Study of turbulent dynamics in a linear magnetized plasma

河内, 裕一

Study of turbulent dynamics in a linear magnetized plasma

Yuichi Kawachi

Contents

Chapter 1

Introduction

1.1 Sustainable development goals and nuclear fusion power

In recent years, while the population is growing and technological innovation is advancing around the world, there is a need to realize a sustainable society. Sustainable Development Goals (SDGs), which consist of 17 goals for sustainable society, were unanimously adopted at the 2015 United Nations Conference. As stated in SDG 7 of Affordable and clean energy and SDG 13 of Climate Action, there is a need for clean and affordable energy that has less impact on the environment. Moreover, the Paris Agreement of 2015, adopted by 196 countries as a measure to combat global warming, promotes efforts to keep the global temperature rise well below 2 degrees Celsius compared to pre-industrial levels. Thermal power generation using fossil fuels, which has been the main method of power generation so far, can provide a stable supply of energy, but there are problems such as economic disparity due to the uneven distribution of fuels and fuel depletion, and one of the biggest problems is that it emits a lot of CO_2. Thus, realization of a decarbonized, clean, and affordable energy source to replace thermal power generation is strongly desirable.

Various technologies are being used to solve energy problems toward

the sustainable and decarbonized society. For example, there are clean energy sources such as solar power and wind power. These are called renewable energy sources, and they are attracting attention as inexpensive energy sources that do not emit CO_2 and can be generated anywhere on the planet. On the other hand, there are still many problems to be solved, such as high power generation costs, low power generation per area, and unstable power generation that is greatly affected by the climate.

Nuclear power is also being used as a decarbonized energy source. Nuclear power generation uses the nuclear "fission" of atoms. In addition to not emitting CO_2, it has the advantages of stable energy supply, high power generation per area, low power generation cost, and high power generation per fuel (one gram of fuel can produce the energy equivalent to 1.8 tons of oil). However, nuclear power generation generates long-lived high-level radioactive materials, and their disposal has become a problem. There are also concerns about environmental risks due to leakage of radioactive materials. Furthermore, because of the possibility of large-scale accidents such as runaway fission reactions, as exemplified by the Chernobyl nuclear power plant accident in 1986 and the Fukushima Daiichi nuclear power plant accident following the Great East Japan Earthquake in 2011, various measures to prevent these large-scale accidents are essential.

Thus, there is a need for a clean and stable energy source with no carbon emissions to replace renewable energy and nuclear power. One of the solutions to this problem is nuclear "fusion" power generation. In nuclear fusion power generation, the energy generated when atomic nuclei collide with each other and nuclear "fusion" occurs is used to generate electricity. In the sun, an enormous amount of energy is constantly generated by nuclear fusion, and this energy illuminates and warms the earth. The advan-

tages of nuclear fusion power generation are that it does not emit CO_2, the fuel is inexhaustible and ubiquitous (deuterium and lithium in the ocean), the energy per fuel is high (one gram of fuel can produce the energy equivalent to 8 tons of oil!). In addition, the fusion reaction does not runaway in principle, which is a problem in nuclear power generation using nuclear fission. Thus, fusion power generation is a clean and affordable power generation that has the potential to solve the energy problem.

However, there are still many challenges to fusion power generation, and it has not yet been realized. The challenges of fusion power generation include engineering and scientific challenges. The engineering issues include the development of materials that can withstand the radiation and heat loads from plasma, the improvement of the performance of superconducting coils and plasma heating devices, and the establishment of the fuel recycling system. These issues are related to the realization of nuclear fusion and its economic efficiency. On the other hand, the scientific challenges are to elucidate the wide variety of physical phenomena observed in fusion devices. In fusion devices, sudden plasma disruptions and anomalous transport phenomena that cannot be explained by collisional transport have been observed. It is believed that understanding and controlling these physical phenomena will lead to the improvement of fusion power generation performance.

1.2 Magnetic confinement of plasma

In order for nuclear fusion to occur, atomic nuclei must collide with each other at a very high speed. As the an atom is accelerated, the electrons are stripped from the atom and separated into ion and electrons. In order for ions to collide many times, they must be accelerated fast enough to over-

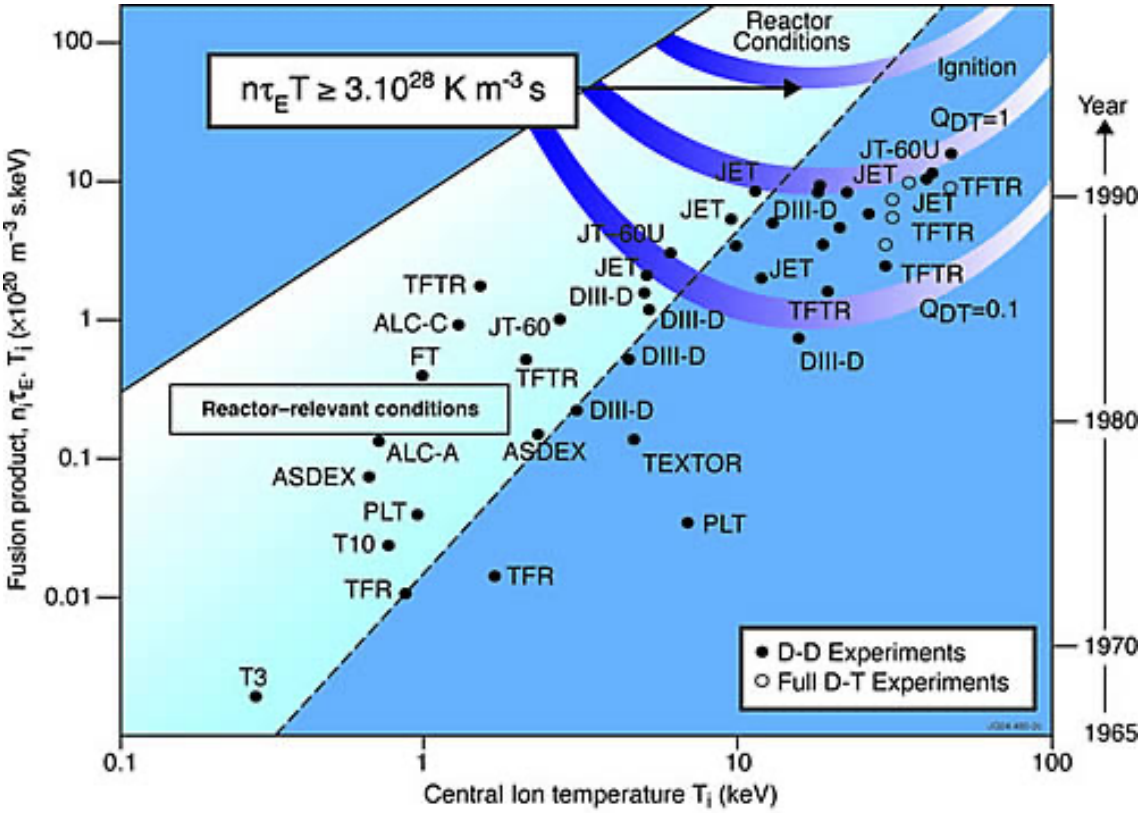

Figure 1.1: Triple products reached by various devices [2].

come the Coulomb force acting on them, and the target ions must be kept dense so that the ions can easily collide. In addition, it is important to keep the fusion reaction going for a long time. Therefore, instead of colliding a small number of ions in an accelerator, it is necessary to maintain a state called plasma, where a large number of ions and electrons coexist and are electrically neutral from a macroscopic point of view. In other words, the plasma must be kept hot (100 million Celsius degrees), dense (10^{20}m^{-3}), and for a long time (1 second). The product of these three factors, temperature, density, and time, is called the triple product. The triple products of various fusion devices are shown in Figure 1.1. When the triple product is greater than 10^{21}(keVm^{-3}s), nuclear fusion occurs continuously, and this condition is called the Lawson criterion [1].

In the sun, the fusion reaction is maintained by “confining“‘ the plasma with its own enormous gravity. For nuclear fusion to occur on Earth, it is necessary to “confine“‘ the plasma by means other than gravity. Magnetic field confinement and inertial confinement methods have been mainly studied as plasma confinement methods, and it has been found through more than 70 years of research that the magnetic field confinement method in particular has high performance.

Charged particles in magnetic fields rotate around the magnetic field lines due to the Lorentz force, and their motion in the direction perpendicular to the magnetic field is restricted. This is called gyro motion or cyclotron motion, which confines the plasma perpendicular to the magnetic field. To prevent the diffusion of charged particles in the direction parallel to the magnetic field, the magnetic field is designed in a donut-shape. Furthermore, in a donut-shaped magnetic field, there is a magnetic field gradient that causes ions and electrons to move in opposite directions, resulting in charge separation. The ExB flow due to the electric caused by charge separation and magnetic fields causes the plasma to move outward, so it cannot be confined. Therefore, by twisting the magnetic field, the charge separation is suppressed and the confinement is improved. There are two methods of twisting the magnetic field lines: the tokamak method, which twists the magnetic field by toroidal plasma current, and the stellarator or heliotron method, which twists the magnetic field by external coil.

Until the 1950s, just after the end of World War II, research on magnetic confinement fusion was carried out in secret by each country. Then, in 1968, it was announced that 1 keV plasma of T-3 tokamak had been achieved in the Russian tokamak T-3 [3], and in 1969, a British research team measured 1 keV plasma by Thomson scattering [4], and since then, researches of

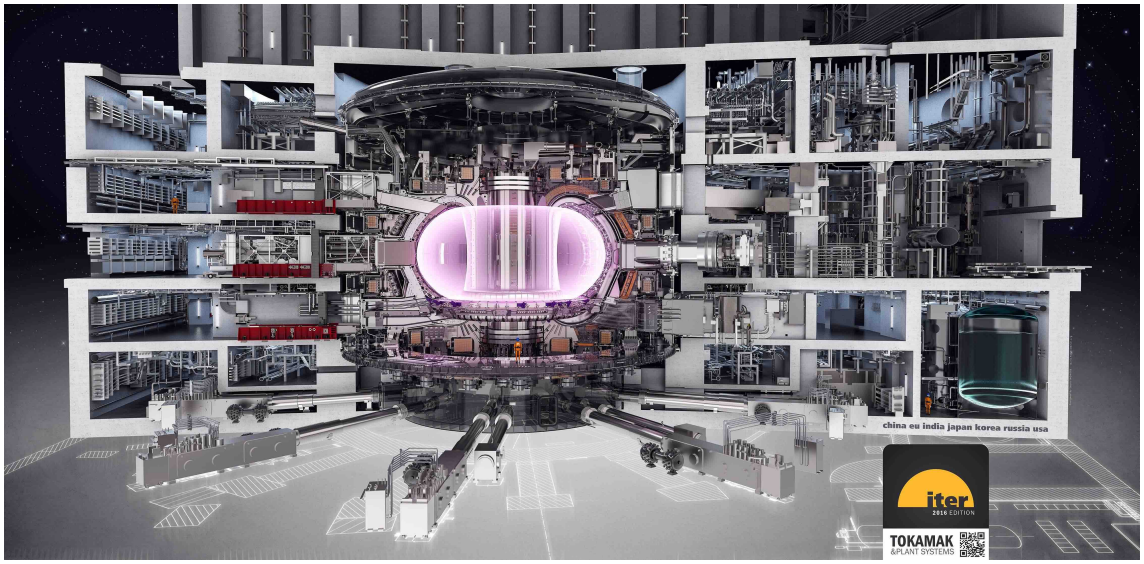

Figure 1.2: Schematic of ITER [11].

tokamak and other confinement method have been conducted with international cooperation and competition. At one time, it was thought that fusion power generation would not be realized in the tokamak system because the plasma would not be heated due to anomalous transport caused by turbulence, no matter how much power was input [5]. However, many studies on turbulence and radial electric field shear structure formation, including the discovery of an high confinement operation mode (H-mode) that reduces anomalous transport due to turbulence [6–8], and the improvement of simulation technology have progressed [9]. Currently, the tokamak devices are expected to be the closest to the realization of nuclear fusion. ITER (International Thermonuclear Experimental Reactor) is a large tokamak device, as shown in Figure 1.2, which is being constructed through international cooperation. ITER is designed to achieve a ratio of heating power to fusion output power close to 10 [10]. Once the ITER fusion power is demonstrated, each country will start to build its own industrial fusion reactor (DEMO reactor).

1.3 Complex phenomena of the plasma turbulence

As mentioned in the previous subsection, the basic physical processes of plasma turbulence need to be clarified to control the plasma turbulence and realize the fusion reactors. In magnetic confinement plasmas, the plasma core is heated by external heating, but at the plasma boundary, the temperature of the vacuum vessel is about room temperature, which essentially creates a density and temperature gradient. The free energy due to these gradients causes many vortices and waves to be linearly excited. (e.g., drift waves are excited by density gradients [12].) The fluctuations drive the transport to relax the gradient of the background, which is the source of the free energy. This fluctuation-driven transport is thought to be the cause of anomalous transport, which is 10 to 100 times larger than the collisional diffusion observed in fusion devices.

The excited fluctuations cascade their energy into smaller scale structures through nonlinear three wave coupling and forms turbulent states. Furthermore, quasi-two-dimensional turbulence, such as magnetized plasma turbulence, inversely cascades the energy of the fluctuations to larger structures [13]. In addition to the nonlinear coupling, there are various other nonlinear processes in magnetized plasmas, such as wave-particle interaction. Through linear growth, dissipation to the plasma structure, and nonlinear processes, the turbulent dynamics of the plasma is determined [12].

Momentum transport driven by turbulent fluctuations is believed to drive meso-scale structures such as zonal flows and streamers, which are also related to the inverse cascade due to nonlinear coupling [8,14]. The zonal flow is a flow with a structure whose wavenumber in the azimuthal direction is $k_\theta \sim 0$ and whose wavenumber in the radial direction is $k_r \neq 0$. The zonal

flow decorrelates and suppresses the turbulence, thereby suppressing the turbulent transport and contributing to the improvement of the plasma confinement [7,15,16]. On the other hand, the streamer have a finite wavenumber in the azimuthal direction ($k_\theta \neq 0$) and a zero wavenumber in the radial direction ($k_r \sim 0$), which connects the core and the edge of the plasma, causes ballistic and non-local transport, and significantly degrades the confinement performance [17–21].

1.4 Problems of plasma diagnostics and of conventional analytical method, for plasma turbulence study

Since the frequency of plasma turbulence ranges from a few kHz to a few hundred kHz and the spatial scale is of the order of ~ 1 cm, it is necessary to measure the plasma with high temporal ($\sim$MHz) and spatial ($\sim$mm) resolutions for experimental studies of plasma turbulence. Various kinds of diagnostics have been developed for turbulence observation. In tokamak plasmas, for example, density fluctuations measured by reflectometer [22], and density and potential fluctuations measured by heavy ion beam probe (HIBP) have been used to study plasma turbulence [23], and many results have been obtained, such as the discovery of turbulence suppression in H-mode and the identification of zonal flows [7, 24]. For the study of plasma turbulence in a low-temperature basic plasma, electrostatic probe measurements are available, in which electrodes are inserted directly into the plasma. Due to the high temporal and spatial resolutions and high signal-to-noise ratio, of the electrostatic probe, many results on fundamental processes of plasma turbulence have been reported, such as studies on nonlinear processes of drift waves [25, 26], formation of streamer structures [19–21], and

interaction between drift waves and zonal flows [27, 28].

While many results have been achieved by the plasma turbulence measurement technique, there are still many problems in plasma turbulence measurement. One example is the measurement of temperature fluctuations caused by plasma turbulence. Thomson scattering and electron cyclotron emission measurement have been used to measure electron temperature in torus plasmas [4, 29]. Thomson scattering has poor temporal resolution ($\sim$Hz), so electron temperature fluctuation measurement is not possible. Although electron cyclotron emission measurements have sufficient time resolution, they cannot measure turbulence because the noise is so large that the turbulent oscillation signal is buried in the thermal noise. For the electron temperature measurement in basic plasma devices, the electrostatic probe has been mainly used [30], and its time resolution depends on sweep frequency of the voltage. If the sweep frequency is high, the stray capacitance distorts the probe current-voltage characteristics, so the sweep frequency is limited to about 1 kHz [31]. That's why, the time resolution is not enough for turbulence measurement. The ion temperature fluctuation measurement is still difficult for the same reason as the electron temperature measurement [32].

Another example of tasks for plasma turbulence measurement is the direct measurement of the transport driven by plasma turbulence. In general, it is difficult to evaluate turbulence-driven transport directly in fusion devices, and the turbulent transport has been estimated by particle and energy balance equations and plasma profile measurements [33, 34] and by order evaluations such as Bohm diffusion and gyro-Bohm diffusion [33, 35, 36]. In order to directly observe fluctuation-driven particle transport or heat transport, it is necessary to measure velocity and density or temperature

fluctuations at the same time and position. In the case of magnetized plasmas, most of the velocity fluctuations are caused by electric field fluctuations, so that velocity fluctuations are often estimated by measuring potential fluctuations. Fluctuation-driven particle transport has been observed by simultaneous measurement of density and potential fluctuations using electrostatic probes in the laboratory plasma and HIBP measurements in the torus plasma [21, 37–40]. However, electrostatic probe measurements has some problems such as the inability to use electrodes at high temperatures and the need to be careful in interpreting the measurement results because electron temperature fluctuations can affect the results. The problem with HIBP measurement is that the scale of the measurement device is large and the port is limited, and there are conditions where measurement cannot be performed depending on the magnetic field shape and temperature. It is even more difficult to evaluate fluctuation-driven heat transport because it is difficult to measure temperature fluctuations in the first place. That's why there are few direct observation of fluctuation-driven heat transport .

In the study of plasma turbulence, in addition to the measurement of turbulence, it is important to understand the characteristics of the turbulence by using data analysis. The Fourier analysis, which is a stationary analysis, has been mainly used to analyze turbulence. However, in general, nonlinearity of plasma turbulence causes non-stationary phenomena, so it is important to understand how the turbulent phenomena changes with time, and non-stationary analysis should be applied. Although wavelet analysis has been developed as an non-stationary analysis [41–43], higher time resolution analysis is required to clarify the details of turbulence dynamics.

The conditional sampling method, which has been used in the analysis of magnetized plasma turbulence and neutral fluid turbulence, is one

of the non-stationary analysis that analyzes the time evolution of pulse-like coherent phenomena [44, 45]. The conditional sampling method can be applied to improve the temporal resolution of plasma measurement and to reconstruct the simultaneous multi-position measurement of different physical quantities. In other words, the conditional sampling method is the non-stationary analysis suitable for turbulent fluctuation analysis and has the potential to solve the problems of time resolution and transport measurement in turbulence study. However, although the conditional sampling method is effective for the analysis of intermittent phenomena such as Blobs and edge localized modes [46–50], it is difficult to apply the conditional sampling method to turbulent fluctuation because the waveform of turbulent fluctuations is generally any waveform rather than pulse-like.

1.5 Purpose of the thesis

The purpose of this thesis is to develop a new method to extend the conditional sampling method to arbitrary waveforms, in order to solve the problems of measurement and data analysis of plasma turbulence. Furthermore, by applying the new method to experimental data obtained from PANTA, this thesis aim to observe turbulent dynamics including electron temperature fluctuations, which are difficult to measure, nonlinear energy dynamics, and the instantaneous frequency fluctuation of turbulent fluctuation, which is an non-stationary picture of turbulence.

This thesis is organized as follows. In Chapter 2 the experimental device, diagnostics and data analysis methods used in this study are introduced. Chapter 3 is devoted to describe the template method developed in this study, the validation results of the template method, and the instantaneous frequency fluctuations obtained by applying the template method.

The results obtained by analyzing the experimental data with the template method, including the spatiotemporal dynamics of the fluctuations and the nonlinear dynamics between different fluctuations, in Chapter 4. This thesis is concluded in Chapter 5.

Chapter 2

Experimental Setup and Analytical method for plasma turbulence

Plasma turbulence has been studied in various experimental devices by using a variety of diagnostics and analytical methods. The experimental devices include torus-type machine and linear machines. Linear devices are more suitable for observing the spatiotemporal dynamics of turbulence because their magnetic field structure is simpler and their low temperature allows the use of probes. In this study, turbulence experiments were performed in a linear magnetized plasma device, PANTA. Main diagnostics tools of PANTA are electrostatic probe arrays. The obtained plasma turbulence data can be subjected to statistical analysis, such as spectral analysis, to capture important features of the plasma turbulence, such as dispersion relation and nonlinear coupling strength. In this chapter, the experimental device, PANTA is introduced in Section 2.1. In Section 2.2, the electrostatic probe arrays and their measurement principles are reviewed . The basic analytical methods used in this study are described in Sections 2.3-2.5.

2.1 PANTA

PANTA (Plasma Assembly for Nonlinear Turbulence Analysis) is a linear device in Kyushu University [38], which is a successor device of LMD-U [19, 51]. Figures 2.1 and 2.2 show a schematic view and a photo of discharge, of PANTA, respectively. Linear magnetized plasma devices such as PANTA have been developed all over the world, and a lot of studies on fundamental plasma processes have been carried out [19, 26–28, 52–55]. The advantages of linear devices are listed below.

- Simple magnetic field structure
- High reproducibility of discharges allows for a large number of statistics
- Good accessibility of plasma diagnostics
- Low temperature allow us to use electrostatic probe with high temporal and spatial resolution
- Easy and flexible experimentation

PANTA and its successor device of LMD-U are designed to observe plasma turbulence in detail, in which has successfully observed basic process of plasma turbulence [28,56], nonlinear interaction [19,27], and turbulent transport [21, 37, 57] etc.

PANTA comprises a vacuum vessel, a magnetic field generating coil, and a plasma source. The vacuum vessel is cylindrical with a length of 4050 mm and a diameter of 450mm, and consists of 16 modular chambers with various shapes that allow for flexible installation of various measurement and plasma control tools, such as electrostatic probes and visible light tomography. Five turbo-molecular pumps are installed at near the end of the

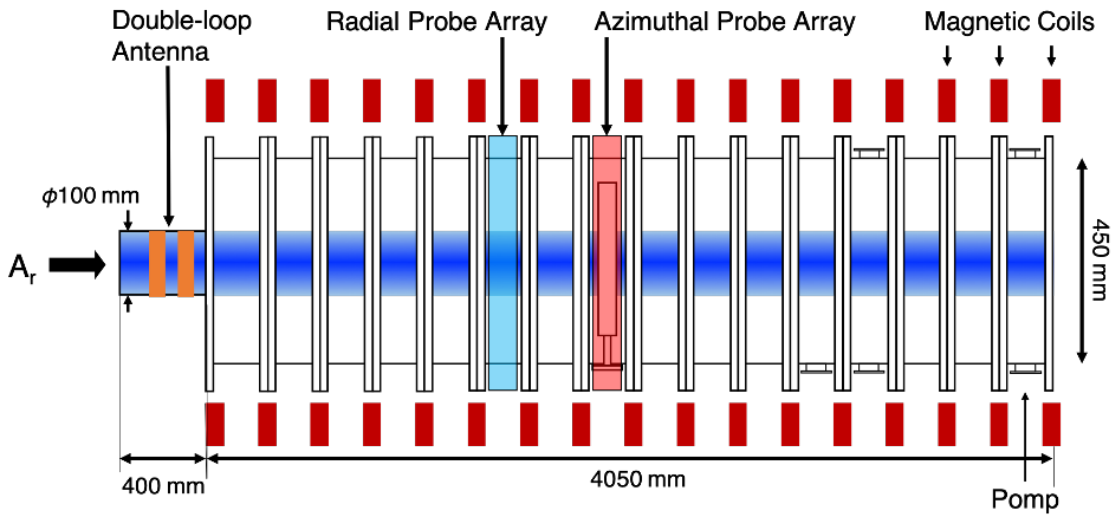

Figure 2.1: Schematic view of a linear magnetized plasma device, PANTA.

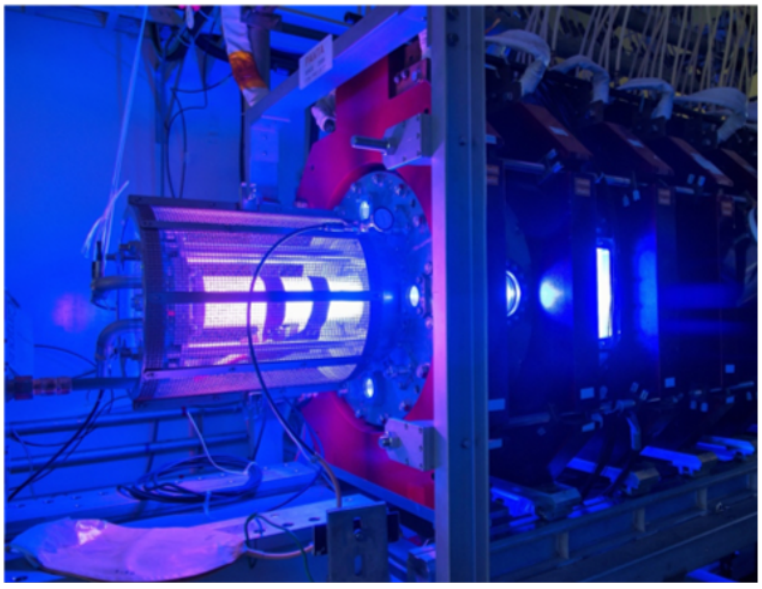

Figure 2.2: A photo of the discharge on PANTA.

vacuum vessel which realize at most the total exhaust velocity of 1400 L/s. The background pressure is achieved to reach 1×10^5 Pa in PANTA.

Homogeneous magnetic field is generated by 17 pairs of Helmholtz coils. The direction of the magnetic field is from the plasma source to the end side. Since the coil current is always flowing in a steady power supply, the experiment is conducted with a steady magnetic field. The experiment is conducted with a steady magnetic field since the coil current is constantly applied to the coils by a constant power supply. The magnetic field is controlled by a control panel that controls the current applying to the coils, and the range of the magnetic field is from 0 T to 0.15 T.

In PANTA, Argon plasma is produced by helicon wave, which is generated by sweeping RF of 7 MHz to a double loop antenna made of copper surrounding a quartz tube with the inner diameter of 100 mm. Helicon waves are right-handed circularly- polarized electromagnetic waves whose frequency is in the range of $\omega_{ci} < \omega < \omega_{ce}$, and they propagate along magnetic fields. Here, ω_{ci} is ion cyclotron angular frequency of (A_r^+), and ω_{ce} is electron cyclotron angular frequency. The RF frequency of 7 MHz is satisfied the frequency criterion, as $\omega_{ci} \approx$ 23-57 kHz and $\omega_{ce} \approx$ 1.7-4.2 GHz for the magnetic field of 0.06-0.15 T. Helicon wave can generate high density plasma up to $\sim 10^{19} m^{-3}$ and form strong density gradient. Although helicon waves have been utilized variety of applications [58–61], the plasma production and heating mechanism has not been understood yet [62–64].

The RF power source is connected to matching circuit box. In the matching circuit box, a pair of variable capacitor is adjusted as the ratio of the incident RF power and reflected power. Typical temporal evolution of incident and reflected power is shown in Figure 2.3. The ratio of reflected/incident power is less than 10 % between 0.24 s and 0.54 s, when the discharge is

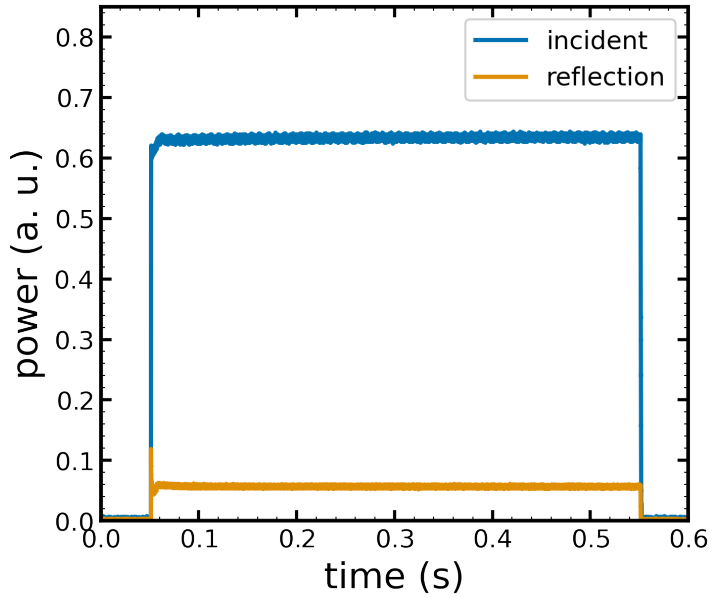

Figure 2.3: Temporal evolution of RF incident and reflected power

quasi-stable.

Argon neutral gas pressure is controlled by the mass flow controller at the plasma source. To keep steady the neutral gas pressure, baffle plates are installed at 375 mm from the source and end of the vessel. Neutral gas pressure is measured by ionization gauge.

2.1.1 Experimental condition

PANTA has three plasma control knobs: neutral gas pressure(P_{n}), magnetic field (B), and RF input power (P_{in}). The control parameter are summarized in the table 2.1. A neutral gas pressure is controlled in the range 0.45$\sim$5 mTorr by mass flow controller to mainly change electron density and ionization degree. Magnetic field is controlled by coil current in the range of 0$\sim$0.15 T, and may relate to fluctuation scale and radial transport due to ion Larmor radius $r_{\mathrm{L}} = \omega_{\mathrm{ci}}/C_{\mathrm{s}} = eB/m_{\mathrm{i}}/C_{\mathrm{s}}$. The RF input power can

Table 2.1: Control parameters of PANTA

parameters	range
Neutral gas pressure	0.45∼5 mTorr
Magnetic field	0∼0.15 T
RF input power	2.4∼6 kW

Table 2.2: Typical plasma parameters of PANTA

parameters	range
electron density	$10^{18} \sim 10^{19}$ m^{-3}
electron temperature	1∼5 eV
ion temperature	0.1∼0.3 eV

be controlled up to 6 kW, but more than 2.4 kW of RF power is required for stable and effective plasma production. Corresponding plasma parameters, electron density, electron/ion temperature are controlled as summarized in table 2.2.

Recently, a new turbulent state was observed in the condition ($P_{\rm n}, B, P_{\rm in}$) = (3 mTorr, 0.13 T, 6 kW). A typical plasma profile of the condition measured by electrostatic probe, are shown in Figures 2.4 (a)-(d). Strong density gradient is formed around r = 30-60 mm. While the density gradient-scale-length becomes minimum at r = 40 mm, the ratio of the gradient-scale-lengths of density and temperature is about 0.5. In this case, drift wave is unstable, but the electron temperature gradient mode is stable. Electron diamagnetic velocity is evaluated as about $V_* = \left(\frac{dn_e}{dr}\right) T_{\rm e}/eB = 700$ m/s. Profiles of floating potential and plasma potential are shown in Figures 2.4 (c) and (d). plasma potential is estimated from electron temperature and floating potential from the relationship that can be expressed in Equation (2.11) (see section 2.2). The profile of the plasma potential is flat in the inner region of the plasma (r $\leq$ 40 mm) and has gradient in the outer region (r $>$ 40 mm) within the error. It is noted that because the plasma potential is evaluated by using the model and thus accuracy depends on the model. In addition,

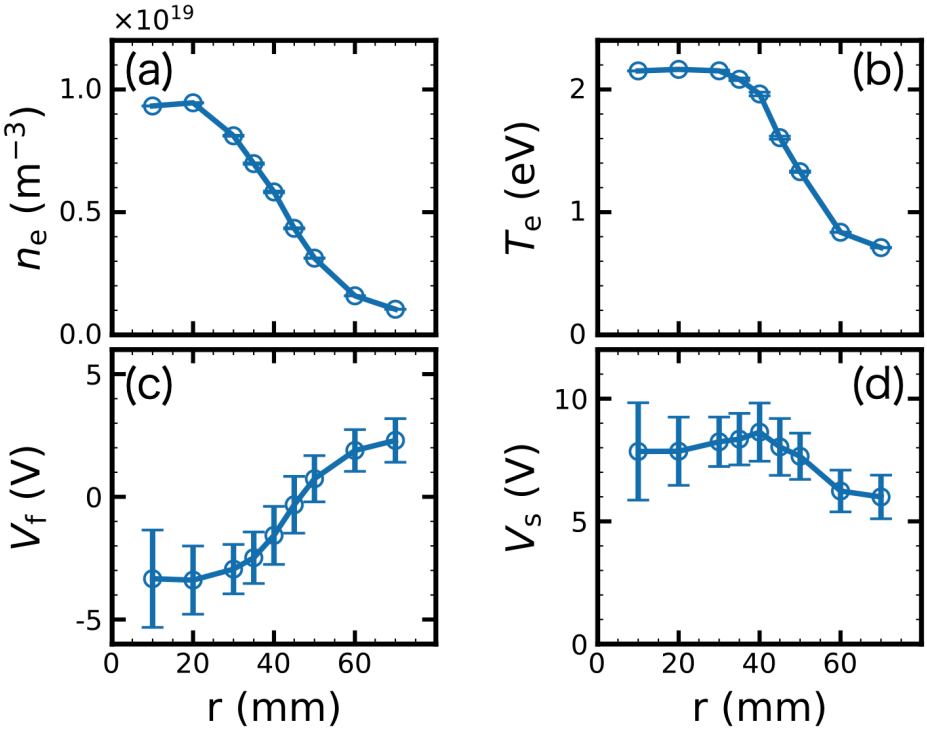

Figure 2.4: Radial profiles of (a) electron density, (b)electron temperature, (c) floating potential, (d) plasma potential observed in the condition $(P_{\mathrm{n}}, B, P_{\mathrm{in}})$ = (3 mTorr, 0.13 T, 6 kW).

the evaluation of the radial electric field has a very large error due to the large error derived from the floating potential error. The LIF measurement supports weak existence of E_r in the inner region [65,66], so that $E \times B$ flow is smaller than diamagnetic drift velocity around r = 40 mm, but measurement accuracy is poor in the outer region. Precise potential or flow measurement is an issue left to be addressed in the future.

Figures 2.5 (a) and (b) show typical two-dimensional spectrum evaluated by 64ch probe and Fourier analysis (see sections 2.2 and 2.3). Coexisting two different rotating modes are observed in normalized density and potential. A $m = 1$ mode has frequency of about 1.6 kHz and a $m = 4$ mode has frequency of about 9.4 kHz. The phase velocities of the $m = 1$ mode and

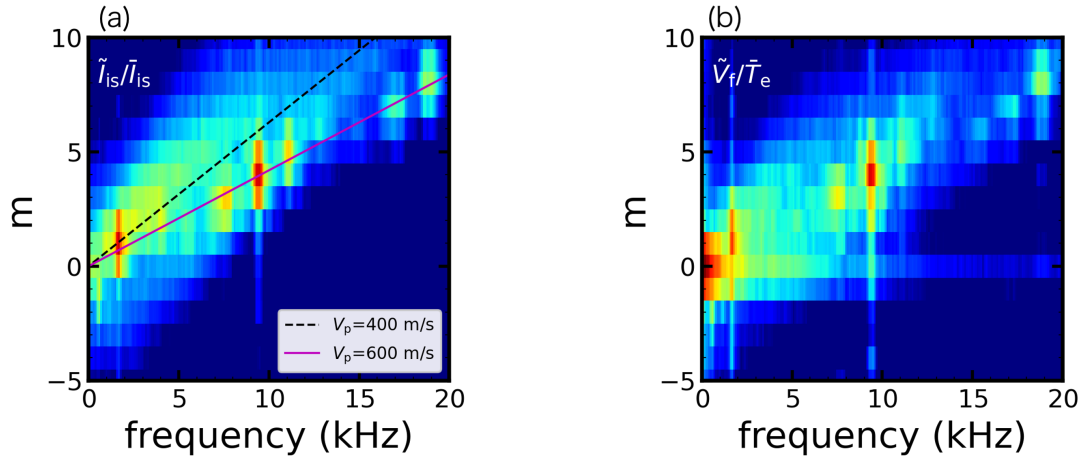

Figure 2.5: Two-dimensional spectrum of normalized amplitude of (a) ion saturation current and (b) floating potential.

the $m = 4$ mode are 400 m/s and 600 m/s, respectively. Higher harmonics of them ($m = 2$ and $m = 8$) and side band between the $m = 1$ and $m = 4$ modes ($m = 3$ and $m = 5$) are also observed. The $m = 0$ fluctuation is also observed in only floating potential fluctuation and its frequency is about 300 Hz.

2.2 Electrostatic probe

A variety of diagnostic methods have been developed to obtain information on plasma. Plasma measurements are mainly classified into non-contact measurements and contact measurements. The former including spectroscopic measurements such as Thomson scattering, has the advantage of being able to evaluate physical quantities without disturbance, but has a low signal-to-noise ratio. An example of the latter is the electrostatic probe method (often so-called Langmuir probe), which can measure physical quantities with a high signal-to-noise ratio and high spatial resolution with a relatively simple structure, although it causes disturbances to the plasma and its electrode is melted at high temperatures, making the measurement diffi-

cult. In linear basic plasmas such as PANTA, electrostatic probes can be used for low-temperature plasmas, and electrostatic probes are desirable for turbulent fluctuation measurements that require high signal-to-noise ratio. In this study, electron density (n_e), electron temperature (T_e) and plasma potential (V_s) was measured by the electrostatic probe in PANTA. In the following section, the principle of the electrostatic probe method, its applications, and the specific instruments utilized in PANTA, are explained.

2.2.1 Principles of Electrostatic probe

Electrostatic probe was proposed by Mott-Smith and Langmuir to measure electron temperature, electron density and plasma potential [30]. In the electrostatic probe measurement, electrodes with an applied voltage is inserted into the plasma, and the physical quantity of the plasma is estimated based on the current flowing to the electrodes during the insertion. High-melting-point materials such as tungsten and molybdenum are used for the electrodes because of the large amount of electrons and ions flowing into them. The electrostatic probe measurement is a fundamental measurement that has been widely used in plasma applications, basic experiments, and even edge measurements of fusion plasmas. The basic principles of the electrostatic probe is described bellow.

Single probe method is most basic and simple electrostatic probe measurement [30, 67, 68]. A typical circuit of a simplified electrostatic probe is shown in Figure 2.6. A probe voltage (V_p) is applied to the probe tip against the vacuum vessel, which is often used as a ground, and probe current I_p flowing in from the plasma is measured by the shunt resistor. Local measurement is realized by protecting the area outside the measurement area with an insulator such as alumina tube.

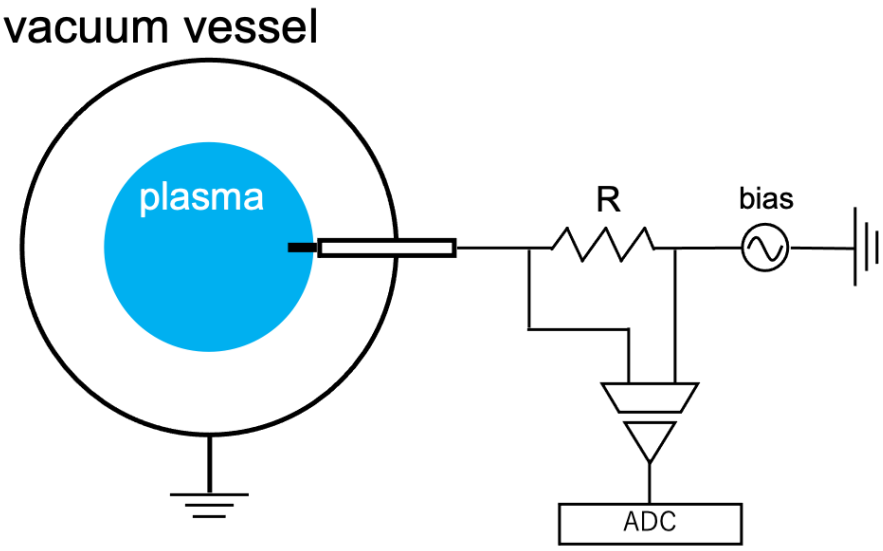

Figure 2.6: Simplified single probe circuit. In PANTA, the bias voltage is often swept in a 100 Hz triangular wave. With a sufficiently steady negative bias, it can be used for ion saturation current measurement.

The theory of electrostatic probes assumes that the velocity distribution of electrons and ions follows a Maxwell distribution, written as

$$f_j(x,v) = n_j(x)\left(\frac{1}{\sqrt{\pi}v_{\mathrm{th},j}^2}\right)^3 \exp\left(-\left(\frac{v_j}{v_{\mathrm{th},j}}\right)^2\right), (j = \mathrm{i}, \mathrm{e}, \tag{2.1}$$

where n_j is density, $v_{\mathrm{th},j}$ is thermal speed, and j indicates particle species (i for ion and e for electron). When the plasma potential and the bias probe voltage are the same, both ions and electrons flow into the electrode, and the current flows according to the thermal velocity of the Maxwell distribution ($v_{\mathrm{th},j} = \sqrt{\frac{8T_j}{\pi m_j}}$) is written as

$$I_{\mathrm{p}} = I_{\mathrm{e}} + I_{\mathrm{i}} \tag{2.2}$$

$$I_j = \frac{1}{4}Aq_j n_j v_{\mathrm{th},j}, \tag{2.3}$$

where A is surface area of the electrodes, q_j is charge of specie j. Since the electron mass is much smaller than ions, that is, thermal velocity of electron is much larger than that of ions, the probe current is dominated by the

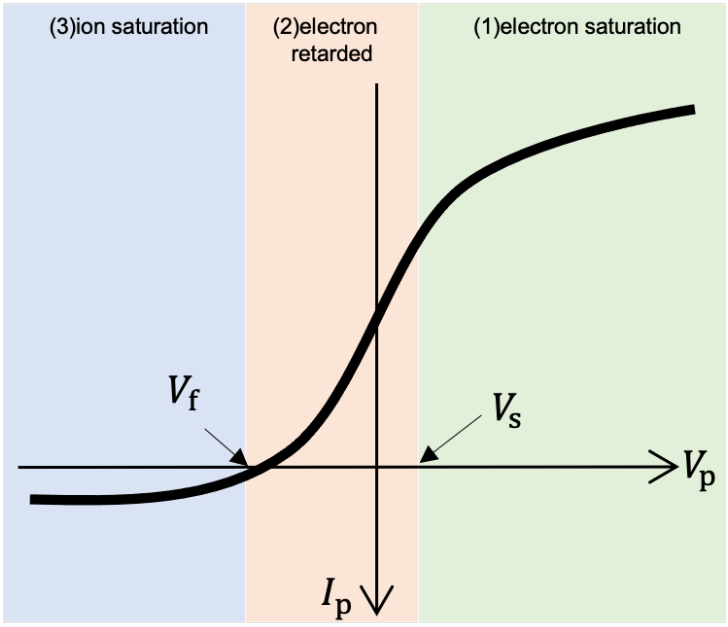

Figure 2.7: Typical I_p-V_p characteristics of the electrostatic probe.

electron current. When the bias voltage is different from the plasma potential, there is a difference in the number of particles flowing in, and this forms a sheath structure around the electrode. Therefore, the flowing in current depends on whether the bias voltage is high or low relative to the plasma potential at the location where the electrode is inserted. A typical current-voltage characteristic curve of a single-probe is shown in Figure 2.7. Usually, the current-voltage (I_p-V_p) characteristics is measured by sweeping probe voltage. The I_p-V_p characteristic is divided into three regions depending on the applied probe voltage at the measurement position: (1) electron saturation region, (2) electron retarded region, and (3) ion saturated region.

(1) Electron saturation region

When a probe voltage larger than the plasma potential is applied to the electrode (i.e. $V_s < V_p$), ions are stripped from the electrode because an

outward electric field is created against the electrode. Therefore, only electrons flow into the electrode, and thus more electrons gather around the electrode and saturate it, forming an electron sheath. In this case, the probe current becomes the electron current only, and is so-called electron saturation current(I_{es}), written as

$$I_{\mathrm{p}} \approx I_{\mathrm{e}} \equiv I_{\mathrm{es}}. \tag{2.4}$$

(2) Electron retarded region

When the probe voltage is less than the plasma potential, the electric field accelerates the ions while decelerating the electrons. In this case, the ion current decreases as the probe voltage increases, but the electron current is still greater than the ion current. Since the electron velocity distribution is assumed to follow the Maxwell distribution, the electron current can be written as

$$I_{\mathrm{e}} = I_{\mathrm{e0}} \exp\left(-e\frac{V_{\mathrm{p}} - V_{\mathrm{s}}}{T_{\mathrm{e}}}\right). \tag{2.5}$$

Ion current, however, is not so simple. Since there are more ions than electrons around the electrode, an ion sheath is formed. In the ion sheath, the ion velocity is accelerated to the ion sound velocity C_{s} by Bohm's sheath condition [69]. Therefore, the ion current can be written as

$$I_{\mathrm{i}} = I_{\mathrm{i0}} + Aq_{\mathrm{i}}n_{\mathrm{i}}v_{\mathrm{th,i}}. \tag{2.6}$$

For basic plasma devices, ion temperature is too small and is negligible. Thus, the ion current is dominated by current due to accelerated to ion sound speed $C_{\mathrm{s}} = \sqrt{T_{\mathrm{i}} - T_{\mathrm{e}})/m_{\mathrm{i}}}$. Consequently, probe current is written as,

$$I_{\mathrm{p}} = I_{\mathrm{i}} + I_{\mathrm{p}} = Aq_{\mathrm{i}}n_{\mathrm{i}}C_{\mathrm{s}} - I_{\mathrm{e0}} \exp\left(-e\frac{V_{\mathrm{p}} - V_{\mathrm{s}}}{T_{\mathrm{e}}}\right) \tag{2.7}$$

When the probe voltage is close to the plasma potential, the ion current can still be neglected because the electron current is much larger than the ion

current. As the probe voltage is lowered, the ion and electron currents are balanced, and the probe current becomes zero at a certain voltage. The probe voltage at this point is called the floating potential, and the voltage area between the floating potential and the plasma potential is so-called the electron retarding region. As shown in Eq. (2.7), the electron temperature is obtained by exponential regression on the I-V characteristic of the electron retarding region.

(3) Ion saturation region

When the probe voltage is sufficiently smaller than the floating potential, electrons cannot reach the electrode and only ions flow into the electrode. At this time, the ion sheath is formed around the electrode, and the probe current can be written as

$$I_{\mathrm{p}} = A q_{\mathrm{i}} n_{\mathrm{e}} C_{\mathrm{s}} \exp\left(-\frac{1}{2}\right) \equiv I_{\mathrm{is}}, \tag{2.8}$$

This probe current is called the ion saturation current (I_{is}), and if the electron temperature is known, the electron density can be estimated from the ion saturation current.

2.2.2 Applications of Electrostatic probe

In addition to the single probe method, there are various applications of electrostatic probes such as the double probe method [70], triple probe method [71], and emissive probe [72]. In this subsection, applications of electrostatic probes utilized in this study is described.

Ion saturation current measurement

In single probe method, probe bias voltage is swept with frequency of a few Hz or a few kHz [31]. Since the time resolution is determined by the

sweep frequency, the single probe method cannot measure phenomena of several kHz to several hundred kHz, such as turbulent fluctuations. Ion saturation current measurement allow us to measure density fluctuation with high time resolution.

When a voltage sufficiently lower than the floating potential is steadily applied as the probe voltage, only the ion saturation current always flows into the probe. The ion saturation current measurement is possible with sufficient time resolution ($\sim$MHz) for turbulent fluctuation measurement. Since the ion saturation current is a function of electron density and electron temperature and ion temperature, the electron density fluctuation can be evaluated as

$$\begin{aligned} n_{\mathrm{e}}(t) &= \frac{1}{Aq_{\mathrm{i}}Cs} I_{\mathrm{is}}(t) \exp\left(-\frac{1}{2}\right) \\ &= \frac{1}{Aq_{\mathrm{i}}} \sqrt{\frac{m_{\mathrm{i}}}{T_{\mathrm{i}} + T_{\mathrm{e}}}} I_{\mathrm{is}}(t) \exp\left(-\frac{1}{2}\right) \end{aligned} \tag{2.9}$$

In basic plasma, ion temperature is much smaller than electron temperature and ion temperature can be negligible. Furthermore, if electron temperature fluctuation is negligible, the electron density fluctuation is proportional to ion saturation current fluctuation written as

$$\tilde{n}_{\mathrm{e}}(t) = \frac{1}{Aq_{\mathrm{i}}} \sqrt{\frac{m_{\mathrm{i}}}{\bar{T}_{\mathrm{e}}}} \exp\left(-\frac{1}{2}\right) \tilde{I}_{\mathrm{is}}(t) \propto \tilde{I}_{\mathrm{is}}(t), \tag{2.10}$$

where $\bar{A}$ and $\tilde{A}$ denote long time average and fluctuation component of A, respectively. The effect of the electron temperature fluctuation measurement on the ion saturation current is described in Section 4.1.1.

Floating potential measurement

The floating potential is described as the voltage at which the electron and ion currents are balanced. This means that if no current flows through the

swept electrode, the electrode will be charged to the floating potential. If the electrode is measured with a high impedance, no current flows through the electrode and the floating potential can be measured. A simple circuit for measuring floating potential is shown in the figure 2.8. Substituting $I_{\mathrm{p}} = 0$ to Eq.(2.7), floating potential can be obtained as

$$V_{\mathrm{f}}(t) = V_{\mathrm{s}}(t) + \alpha \frac{T_{\mathrm{e}}(t)}{e}, \tag{2.11}$$

where

$$\alpha = \ln\left(\exp\left(-\frac{1}{2}\right)\sqrt{2\pi\frac{m_{\mathrm{e}}}{m_{\mathrm{i}}}}.\right) \tag{2.12}$$

For argon plasma, the α is about -5.2. If the electron temperature fluctuation is negligible, the relation between floating potential and plasma potential is evaluated as

$$\tilde{V}_{\mathrm{s}} \approx \tilde{V}_{\mathrm{f}}. \tag{2.13}$$

It should be noted that the effect of electron temperature fluctuation on the floating potential measurement is larger than that on the ion saturation current, since it takes effect at about five times the amplitude of electron temperature fluctuation. The result that the effect of electron temperature fluctuations is not negligible in practice is shown in Section 4.1.1.

Double probe method

The single probe method cannot be used for RF discharges in a vacuum vessel made of insulators such as glass, because there is no electrode to serve as a voltage reference. Also, if the voltage is increased to collect more electron current, the disturbance to the plasma becomes significantly larger. Thus, if the single probe cannot be used, the double probe method can be substituted.

Simple circuit of double probe is shown in Figure 2.9. Two electrodes are inserted into the plasma and a voltage is swept between the two electrodes.

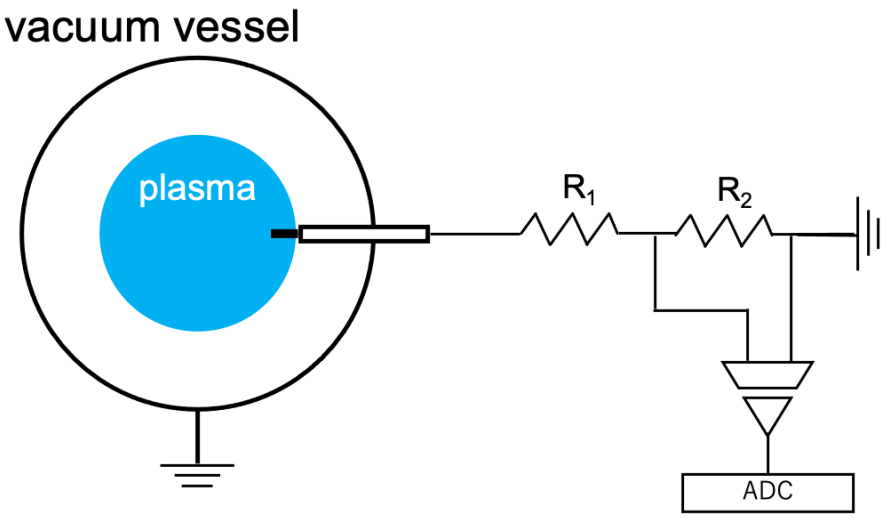

Figure 2.8: Simplified circuit of floating potential measurement. To prevent the current from flowing from the plasma into the probe, the resistance value of resistor R_1 is designed to be much larger than that of R_2, and the typical respective resistance values in PANTA are $R_1 = 1\mathrm{M}\Omega$ and $R_2 = 50\mathrm{k}\Omega$.

The double probe circuit is floated from the plasma. The probe current of the electrodes #1 and #2 are written as

$$I_j = -I_{\mathrm{is},j} + \frac{1}{4} q_{\mathrm{i}} A_1 n_e v_{\mathrm{th,e}} \exp\left(-e\frac{V_{\mathrm{s}} - V_j}{T_{\mathrm{e}}}\right), \quad j = 1, 2. \tag{2.14}$$

Using $I_1 = I_2 = 0$, $V_p = V_1 - V_2$ for I_1, $V_p = V_2 - V_1$ for I_2, and $I_1 = -I_2 = I_{\mathrm{p}}$,

$$I_{\mathrm{p}} = \frac{A_1 I_{\mathrm{is},2} \exp\left(eV_{\mathrm{p}}/T_{\mathrm{e}}\right) - A_2 I_{\mathrm{is},1}}{A_1 \exp\left(eV_{\mathrm{p}}/T_{\mathrm{e}}\right) + A_2}. \tag{2.15}$$

Typical I_{p}-V_{p} characteristics of the double probe is shown in Figure 2.10. When the two electrodes are symmetric and same surface area ($I_{\mathrm{is},1} = I_{\mathrm{is},2} = I_{\mathrm{is}}, A_1 = A_2$), double probe characteristics are finally written as

$$I_{\mathrm{p}} = I_{\mathrm{is}} \tanh\left(\frac{eV_{\mathrm{p}}}{2T_{\mathrm{e}}}\right). \tag{2.16}$$

The ion saturation current and electron temperature are obtained by nonlinear fitting $I_{\mathrm{p}} - V_{\mathrm{p}}$ curve to the Eq. (2.16).

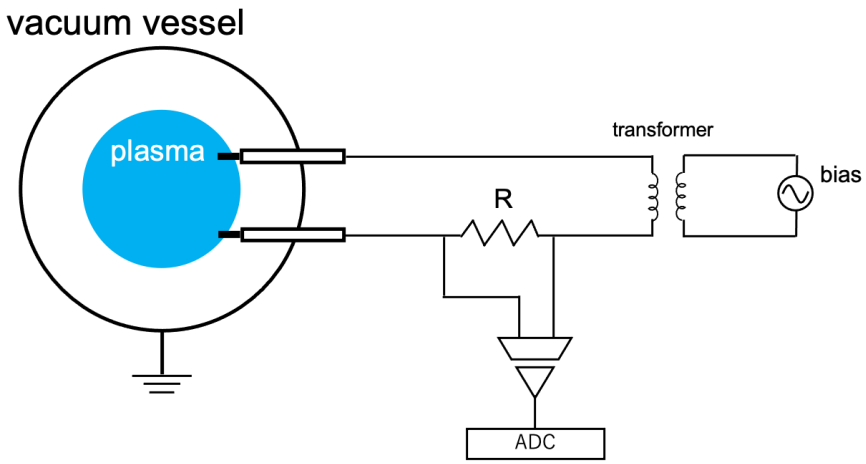

Figure 2.9: Simplified circuit of double probe measurement. The transformer keeps the probe circuit floating away from the plasma. The shunt resistance of $R = 51.5\Omega$ is used for measure the plasma current in PANTA.

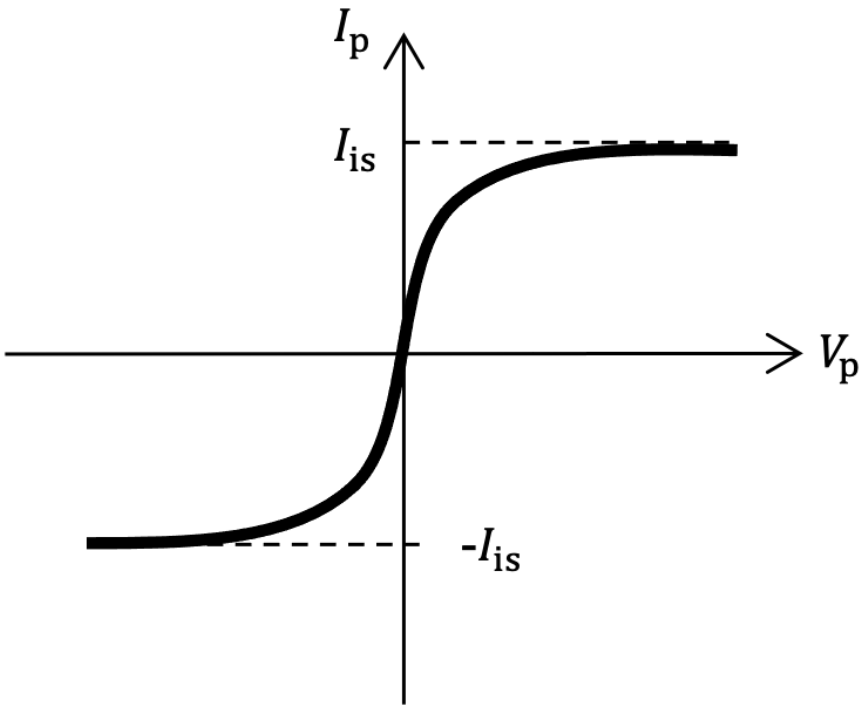

Figure 2.10: Typical I_p-V_p characteristics of the double probe.

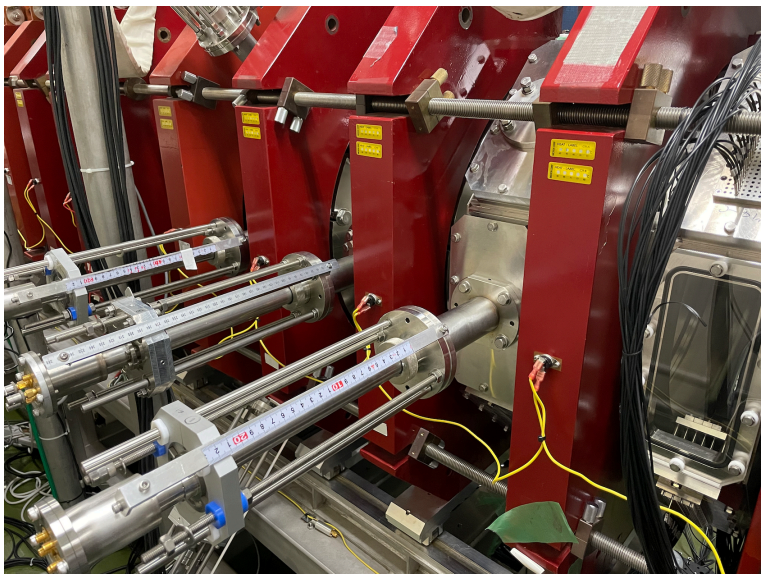

Figure 2.11: Picture of radial movable probe arrays inserted into vacuum vessel of PANTA.

2.2.3 Probe arrays in PANTA

Radial movable probe

In PANTA, there are many probe ports and many radial drive probes can be inserted. The appearance of a radially movable probe is shown in Fig.2.11. The radial movable probes are mainly used to measure the plasma profiles and the radial structure of fluctuations. Various types of probe tips can be attached to the radial movable probe and some examples of probe tips are shown in Figure 2.12. By changing the probe tips at the tip, various applications such as Reynolds stress measurement and axial velocity field measurement have been achieved [56, 57]. In this study, 4-tips probe and 3-tips probe were used for double-probe measurements, ion saturation current measurement and floating potential measurement.

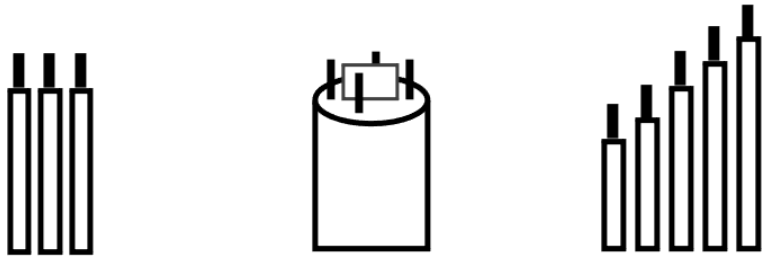

Figure 2.12: Schematics of various tip shapes that can be attached to the radial movable probe.

64ch probe array

In order to measure azimuthal structure of fluctuation, azimuthal probe arrays have been developed in KIWI [73], VINETA [74], TJ-K [75], and PANTA [76]. Photos of an azimuthal probe array in PANTA, so-called 64ch probe array are shown in Figures 2.13 (a) and (b). Each probe tip is made of tungsten and surrounded by an almina tube. The probe tips have diameter of 0.8 mm and length of 3 mm. All probe tips aligned at radius of 40 mm. The 64ch probe array is installed at a distance of 1875mm from the plasma source. Usually, fluctuation of ion saturation current and floating potential are measured by the probe tips at each azimuthal position alternately. The details of the features and alignment of 64ch probe array is referred in Ref. [76]. The 64ch probe allow us to measure the azimuthal and temporal evolution of turbulent fluctuation as shown in Figure 2.14.

2.3 Fourier analysis

Plasma turbulence is complex and non-deterministic phenomena rather than random phenomena. Spectral analysis are well-known tools for characterizing the stochastic process such as the plasma turbulence. The idea of the spectral analysis is decomposed the experimental data as the superposition

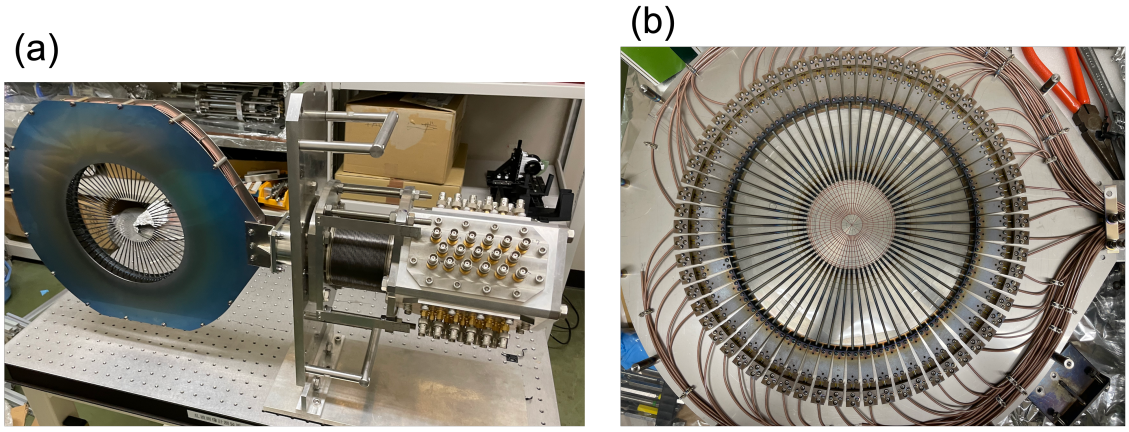

Figure 2.13: Photos of 64ch probe array.

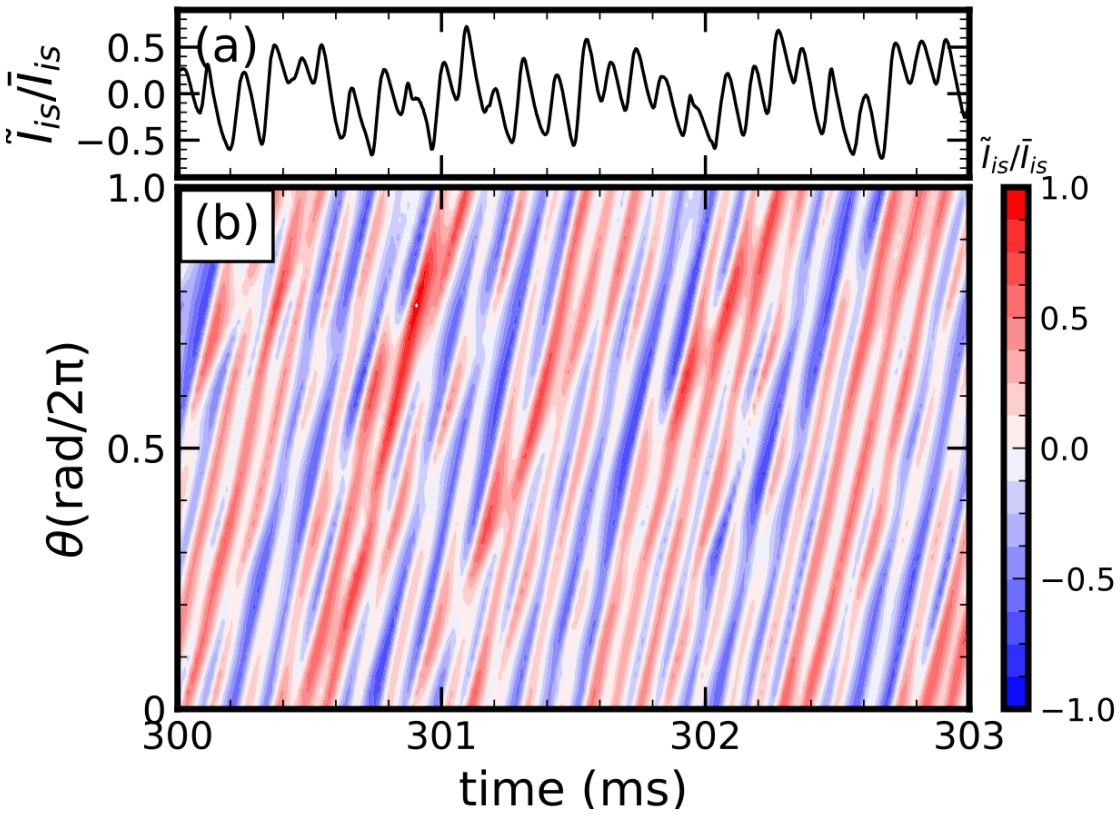

Figure 2.14: (a) Typical temporal evolution and (b) azimuthal-temporal evolution, of ion saturation current measured by 64ch probe.

of sinusoidal wave with each frequency (and wave number). Conventional spectral analysis such as Fourier analysis described next section is ideally assumed that observed data is stationary. In general, Fourier analysis still can provide us deep insights for experimental data even though plasma turbulence is non-stationary phenomena. In this section, the series of conventional Fourier analysis is described.

2.3.1 Fourier transform

Fourier transform is conventional spectral analysis for stationary data. Fourier transform $X(f)$ of the one-dimensional time series data $x(t)$, is defined as

$$X(f) = \int_{-\infty}^{\infty} x(t) e^{-2\pi i f t} dt \tag{2.17}$$

and inverse Fourier transform is defined as,

$$x(t) = \int_{-\infty}^{\infty} X(f) e^{2\pi i f t} df. \tag{2.18}$$

Here f is frequency, t is time, and i is imaginary unit. In practical, experimental data is discrete and finite length N (i.e. $x(t) = x(nt_0), n = (0, 1, 2, \cdots N-1)$), where t_0 is interval time for sampling data. The discrete Fourier transform and inverse Fourier transform is represented as,

$$X(pf_0) = \frac{1}{N} \sum_{n=0}^{N-1} x(nt_0) e^{\frac{-2\pi i p n}{N}} \tag{2.19}$$

and

$$x(nt_0) = \sum_{p=0}^{N-1} X(pf_0) e^{\frac{-2\pi i p n}{N}}, \tag{2.20}$$

where the f_0 is interval of frequency of discrete frequency series and l is $l = (0, 1, 2, \cdots, N-1)$. t_0 is sampling time and p is $p = (0, 1, 2, \cdots, N-1)$

Concerning the aliasing of the higher frequency component, the discrete Fourier transform only allow us to evaluate the Fourier component with

frequency of $f \leq 1/2t_0$, which is so called sampling theorem. For instance, when the time interval of data sampling is $t_0 = 1\mu$s, maximum frequency which can be evaluate the Fourier component is 500 kHz. Frequency resolution of the discrete Fourier transform is determined by time window written as $f_0 = 1/t_0 N$ (e.g. $f_0 =$ 1 kHz for $t_0 = 1\mu$s and data points $N = 1000$).

Fourier transform can be extended in two or three-dimensional data. Two dimensional Fourier transform is defined as

$$X(pf_0, qk_0) = \frac{1}{NM} \sum_{n=0}^{N-1} \sum_{m=0}^{M-1} x(nt_0, m_0) e^{-2\pi i \left(\frac{pn}{N} + \frac{qm}{M}\right)} f_0. \tag{2.21}$$

Here $x(nt_0, mx_0)$ is two dimensional data, M is data length in space points, k_0 is interval of wavenumber of wavenumber resolution of discrete Fourier transform, and q is $q = (0, 1, 2, \cdots, M-1)$. For instance, the two-dimensional Fourier transform can be applied to the two-dimensional data with time and space series obtained from the 64ch probe array. In this case, the two-dimensional Fourier transform allows us to evaluate the Fourier component with frequency and azimuthal wave number space as shown in Figure 2.5. For convenience, azimuthal mode number m is calculated from the azimuthal wave number k_θ as $m = k_\theta / 2\pi r$. The two-dimensional Fourier transform allow us to evaluate the propagation direction of fluctuation. Propagation direction is essential for identifying instability of the fluctuation.

2.3.2 Auto power spectrum

In order to evaluate the fluctuation energy density from the experimental data, the auto power spectrum density can be used. The auto power spectrum density $P(f)$ in range of $[-T/2, T/2]$ is defined as,

$$P(f) = \lim_{T \to \infty} \frac{1}{T} \langle X^*(f) X(f) \rangle \tag{2.22}$$

where angler bracket $\langle\cdot\rangle$ denotes ensemble average. Auto power spectrum density means fluctuation power of the frequency from f to $f + f_0$. Usually, the auto power spectral density is estimated by dividing the experiment data into overlapping segments, computing Fourier transform for each segment, and averaging the Fourier component. This calculation method is called the Welch's method [77]. Various other methods for estimating the power spectrum have been proposed [78,79]. In this study, the Welch's method was used for power spectrum estimation of uniformly spaced time series data, such as electrostatic probe data.

2.3.3 Lomb-Scargle method

Estimating the power spectrum of non-uniformly sampled data is not possible with the analysis described in the previous section. In such cases, the Lomb-Scargle method, an analysis based on the least-squares method, can be used instead [80–83]. This method has been developed mainly for the analysis of satellite data in the field of astronomy, and is equivalent to least-squares fitting to

$$x = a\cos(2\pi t) + b\sin(2\pi t). \tag{2.23}$$

The generalized form of the Lomb-Scargle periodogram is proposed by Scargle [81], and written as

$$\begin{aligned} P(f) = &\frac{1}{2}\left(\sum_{n=0}^{N-1} x(t_0)\sin(2\pi f(t_n - \tau_{LS}))\right)^2 / \sin^2(2\pi f(t_n - \tau_{LS})) \\ &+ \frac{1}{2}\left(\sum_{n=0}^{N-1} x(t_0)\cos(2\pi f(t_n - \tau_{LS}))\right)^2 / \cos^2(2\pi f(t_n - \tau_{LS})) \end{aligned} \tag{2.24}$$

, where t_n data of time obtained at unequal intervals. τ_{LS} is a time lag to ensure time-shift invariance of un-uniformly sampled time and is specified

for each f determined for each f, written as

$$\tau_{\mathrm{LS}} = \frac{1}{4\pi f}\arctan\left(\frac{\sum_{n=0}^{N-1}\cos(-2\pi f(t_n))}{\sum_{n=0}^{N-1}\cos(2\pi f(t_n))}\right). \tag{2.25}$$

The Lomb-Scargle method was utilized for power spectrum estimation of instantaneous frequency evaluated by the Template method which is described in Sec. 3.

2.3.4 Window function

When ensembles are obtained by dividing the experimental data for spectral estimation, as in the Welch's method, the data segments are generally discontinuous at the beginning and end. Since the Fourier transform assumes continuity, this discontinuity will affect the estimation of the spectrum. Therefore, it is common to estimate the spectrum after applying a weight function, called a window function, to the experimental data to make it continuous at the beginning and end of the segment, so that the beginning and end of the data are continuous, as shown Figure 2.15. Various window function have been proposed [84, 85]. Boxcar window (i.e. without window), Han window, flat-top window, and Blackman window are plotted in Figure 2.16 (a) as examples. Figure 2.16 (b) shows the result of estimating the spectrum of the test data by applying each window function. It can be seen that there is a wide range in the spectrum when the window function is not applied while the other window function suppress the width of spectrum. The shape of the spectrum differs depending on the window function, and it is important to choose the proper window function.

2.3.5 Cross power spectrum

The phase relation between the two signals can be evaluated by the cross-power spectrum. The cross-power spectrum $C_{xy}(f)$ of two signals $x(t)$ and

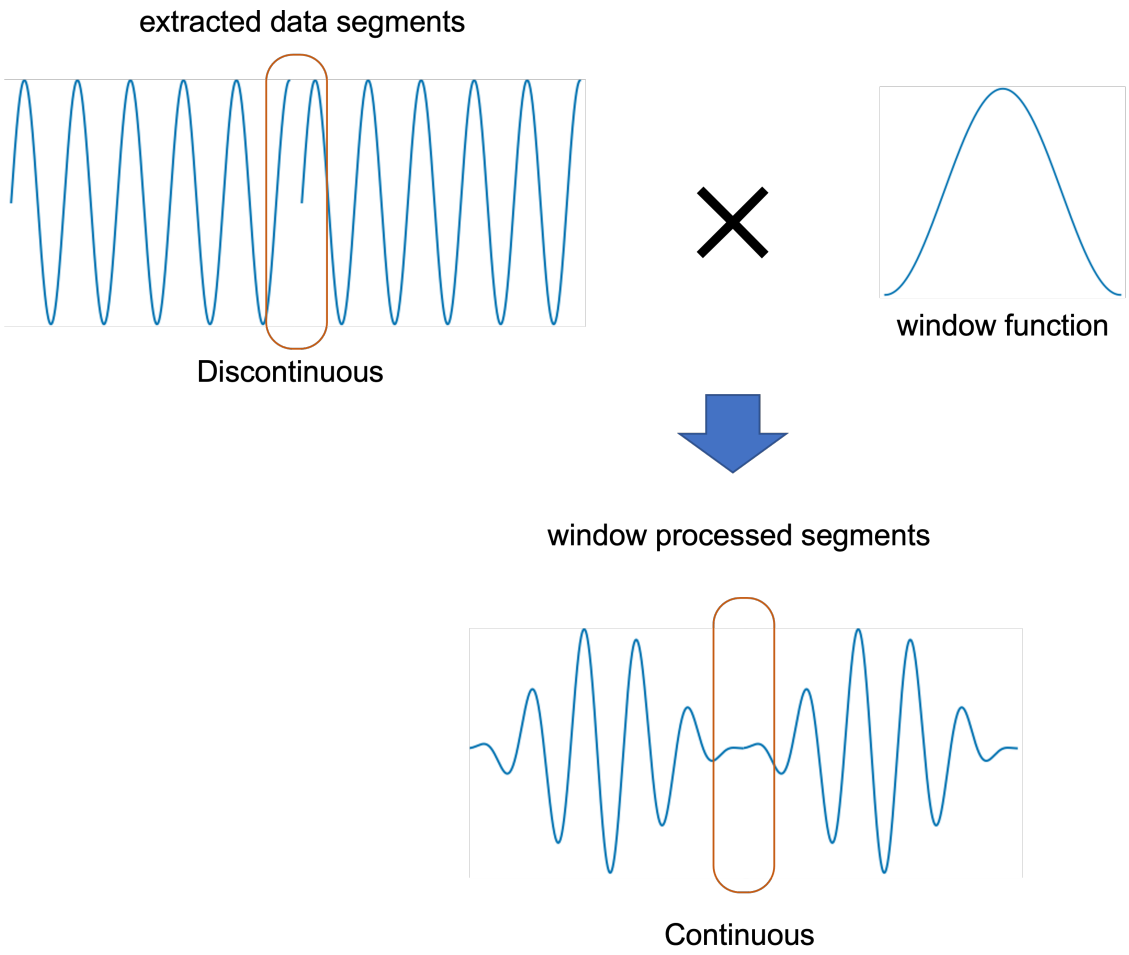

Figure 2.15: Schematics of window function processing.

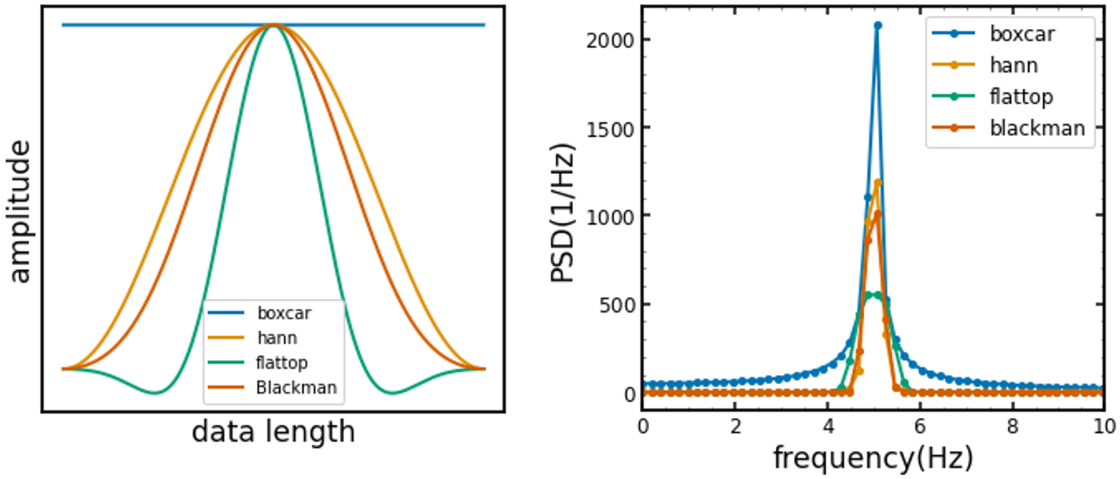

Figure 2.16: (a) Various window functions. It is noted that computing by multiplying by the Boxcar window function is equivalent to computing without the window function. (b) Estimated power spectrum density with each window function.

$y(t)$ is defined as,

$$C_{xy}(f) = \lim_{T\to\infty} \frac{1}{T} \langle X^*(f)Y(f)\rangle \tag{2.26}$$

where, $Y(f)$ is Fourier component of $y(t)$. If $X(f) = Y(f)$, the cross power spectrum is the same as the auto power spectrum. The argument of the cross power spectrum means the average phase difference between the two signals $x(t)$ and $y(t)$, also known as the cross phase. The cross phase $\theta(f)$ is defined as

$$\theta(f) = \arctan\left(\frac{\mathfrak{Im}(C_{xy}(f))}{\mathfrak{Re}(C_{xy}(f))}\right), \tag{2.27}$$

where $\mathfrak{Im}$ and $\mathfrak{Re}$ denotes imaginary part and real part of complex value, respectively. Cross phase analysis has been utilized to evaluate the wavenumber of fluctuations from two signals. Two-dimensional Fourier transform with multi-channel measurement such as 64-channel probe can determine the wavenumber with higher accuracy, but the advantage of cross-phase analysis is that it can evaluate the wavenumber from fewer data. Coherence is defined as the cross-power spectrum normalized by the auto-power

spectrum of the two signals, and can be written as

$$\text{coh}^2_{xy}(f) = \frac{|C_{xy}(f))|^2}{P_y(f)P_x(f))}, \tag{2.28}$$

Correlation strength between Fourier components $X(f)$ and $Y(f)$ can be evaluated from the squared coherence. The squared coherence can be used as indicator of degree of conservation of the cross phase.

2.3.6 Bispectrum

Whereas the cross spectrum is the correlation of two signals, the correlation of three signals can be defined and is called the bispectrum. The bispectrum $B(f_1, f_2)$ can be written as follows,

$$B(f_1, f_2) = \langle X(f_1)Y(f_2)Z^*(f_3)\rangle \tag{2.29}$$

where $X(f)$, $Y(f)$, and $Z(f)$ are Fourier components of time series $x(t)$, $y(t)$ and $z(t)$, respectively. The three Fourier components satisfy the frequency matching condition of $f_3 = f_1 + f_2$. When the Fourier components are obtained from the same time series (i.e. $Y(f) = Z(f) = X(f)$), it is called the auto bispectrum, and when they are not, it is called the cross bispectrum. As in the case of the cross spectrum, the argument of the bispectrum represents the phase difference of the three Fourier components, called the biphase θ_{xyz}, and can be written as

$$\theta_{xyz}(f_1, f_2) = \arctan\left(\frac{\mathfrak{Im}(B(f_1, f_2))}{\mathfrak{Re}B((f_1, f_2))}\right) \tag{2.30}$$

The bispectrum normalized by the power spectrum density represents the strength of the correlation between the three Fourier components, called as bicoherence, and can be written as

$$b^2(f_1, f_2) = \frac{|B(f_1, f_2)|^2}{\langle|X(f_1)Y(f_2)|^2\rangle \langle|Z^*(f_3)|^2\rangle}. \tag{2.31}$$

The auto bicoherence analysis is one of the most important tools in order to quantify the strength of nonlinear coupling [27, 54, 86], and is extended for two dimensional data [19]. Cross-bicoherence has been proposed for application to the explanation of nonlinear phenomena, such as excitation of zonal flows [87], spatial transport of fluctuation intensity related to turbulent spreading or trapping [88].

2.4 Numerical filter

Numerical filter can be utilized to extract specific frequency range from experimental data. Finite impulse response (FIR) filter is one of the numerical filter with window function. The FIR filter can be conducted through the convolution of a time series $x(t)$ with window function $h(j)$ as

$$x'(t) = \sum_{j=-m}^{m} h(j)x(t - jt_0) \tag{2.32}$$

$x'(t)$ is the filtered signal, t_0 is a sampling time, and order of the filter is $k = 2m + 1$. For simplicity, when a sinusoidal wave $x(t) = exp(2\pi ift)$ is input to the system, the filtered signal is obtained as

$$x'(t) = \exp(-2\pi ift) \sum_{j=-m}^{m} h(j) \exp(-j2\pi ift) \quad = H(f) \exp(-2\pi ift), \tag{2.33}$$

where $H(f) = \sum_{j=-m}^{m} h(j) \exp(-j2\pi ift)$ is a transfer function for the FIR filter, which is identical to the Fourier transform of the window function $h(j)$. The numerical filter are characterized by the cut off frequency band (high-pass, low-pass, band-pass, and band-rejected), the ability to cut off the out-band frequency component, the phase delay. Since the performance depends on the window function used, it is important to choose the appropriate window function.

2.5 Hilbert transform

The time series signal obtained in the experiment is a real signal, and the transformation that shifts the phase of each frequency component of the real signal by $\pi/2$ is called the Hilbert transform. The Hilbert transform is defined as

$$\hat{x}(t) = \mathcal{H}(x(t)) = \frac{1}{\pi}\int_{\infty}^{\infty}\frac{x(\tau)}{t-\tau}d\tau. \tag{2.34}$$

A complex signal with the signal obtained by the Hilbert transform in the imaginary part and the original signal in the real part is called an analytical signal and written as

$$x'(t) = x(t) + i\hat{x}(t) \tag{2.35}$$

Since the analytical signal is a complex signal, the instantaneous phase $\theta_{inst}(t)$, which is the phase from time to time, can be evaluated as

$$\theta_{inst}(t) = \arctan\left(\frac{\hat{x}(t)}{x(t)}\right). \tag{2.36}$$

The instantaneous frequency is obtained from the time derivative of the instantaneous phase, written as

$$f_{inst}(t) = \frac{1}{2\pi}\frac{d}{dt}\theta(t) \tag{2.37}$$

Some extended method for instantaneous frequency analysis using Hilbert transform has been proposed [89]. However, if multiple frequency components exist or if there is noise in the experimental data, the evaluation of instantaneous phase is noisy, and its time derivative, instantaneous frequency, has larger error, so care must be taken in its actual use.

The instantaneous amplitude $A_{inst}(t)$ can also be evaluated using the analytic signal, and is written as

$$A_{inst}(t) = \sqrt{x^2(t) + \hat{x}^2(t)} \tag{2.38}$$

The evaluation of the instantaneous amplitude by the Hilbert transform is used in envelope analysis to extract the modulation component of the fluctuation amplitude.

Chapter 3

Development of the template method for turbulent fluctuation

Study on turbulent dynamics is essential for understanding anomalous transport and improving plasma confinement, as mentioned in the Chapter 1. Although variety of analytical methods have been developed for revealing complex turbulent phenomena, the details of basic processes of plasma turbulence is still difficult to understand and has not yet been elucidated. In this chapter, at first, the conventional analytical methods are briefly reviewed and the problem of them are pointed out. Then, a new analytical method developed in this study, is introduced in Section 3.2. The advantage and validation of the new method are shown in Sections 3.3 and 3.4, respectively.

3.1 Limitation of the conventional Fourier analysis and conditional sampling

Many analytical methods for plasma turbulence have been developed and used in the past. One of the most basic and important method is Fourier analysis. As described in Section 2.3, the Fourier analysis is a method of decomposing data into a frequency (and/or wave number) spectrum, assuming that the observed data is a superposition of stationary periodic phenom-

ena. Since plasma turbulence is a kind of oscillatory phenomenon, many valuable information can be obtained by the Fourier analysis. Indeed, the Fourier analysis has allowed us to identify the dispersion relation of turbulent fluctuations using cross spectrum and power spectrum [27, 90, 91], and to identify nonlinear coupling strength using bicoherence [15,20,25,88]. However, in general, actual plasma turbulence is constantly being emerged and disappeared and the period of plasma turbulence can changed in time. Therefore, Fourier analysis assuming a steady-state signal is insufficient for analyzing turbulent flows, and unsteady analysis is required. Although wavelet analysis and Wigner distribution function are proposed as a non-stationary turbulence analysis [41–43, 92, 93], the former still has a problem that the uncertainty principle limits the time resolution and the frequency resolution, and the latter has a problem that a fake peak appears when multiple frequency components exist.

Another analytical method for non-stationary or quasi-periodic signals is conditional sampling technique [44, 45]. The conditional sampling was developed in the field of general fluid turbulence with the aim of extracting coherent structures in complex turbulent flows. In the study of plasma turbulence, it has been widely applied to intermittent phenomena such as blobs and edge localized mode [46–50]. Data processing of conditional sampling is as bellow. The timing when the coherent phenomena happen in time series $x(t)$ are detected in some way, then the ensembles of the temporal evolution of the detected phenomena are sampled. The valuable information, including the averaging time evolution, the emergence timings, and the spatial pattern of different physical quantity at the same time and position, can be evaluated from the conditional sampled data. However, since the results of conditional sampling will change depending on the method

used to detect the coherent phenomenon, a method to correctly detect the phenomenon is desirable.

Several methods to detect the coherent phenomena has been proposed and compared [45, 94–96]. The basic idea of the conventional method for detecting coherent phenomena is to set a threshold value for the time series $x(t)$ and detect the timing when the threshold value is exceeded as the time when the coherent phenomenon appears. This kind of method is so-called the threshold method. An example of the application of the threshold method is shown in Figure 3.1. In the threshold method, the threshold value is artificially determined, for example, several times the standard deviation of $x(t)$, so it is important to note that the results may vary depending on how the threshold value is determined. Another problem with the threshold method is that it is difficult to detect a specific waveform. In other words, the threshold method is good at detecting spike-like waveforms with large amplitude while it is not good at detecting sinusoidal wave-like waveforms. Thus, an alternative detection method to the threshold method is necessary to apply conditional sampling to quasi-periodic but not bursty phenomena such as nonlinear waves.

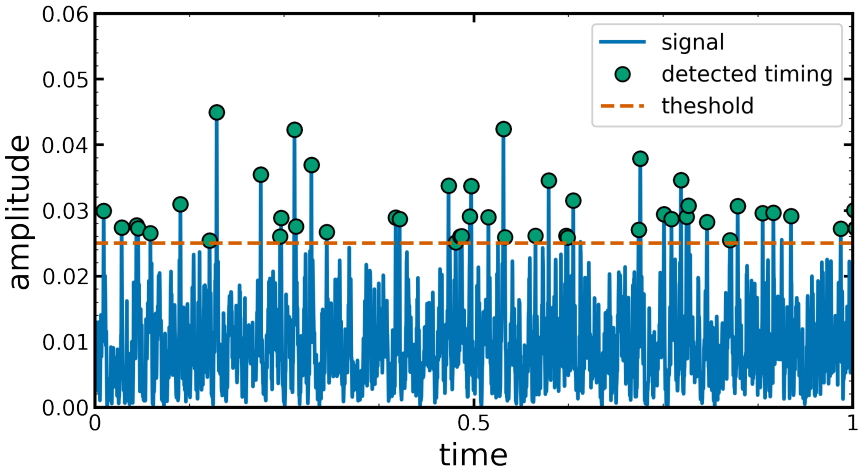

Figure 3.1: An example of the threshold method. Here, A blue line is time series data and the green dots shows detected timings by the threshold method. The threshold value is set to 0.025 as shown by the orange dashed line.

3.2 Template method as an extension to allow conditional sampling to be applied to arbitrary waveform

Template method is one of the methods that can solve the problem of the threshold method. The template method was proposed for Cine-MRI analysis based on electrocardiogram in the medical field [97, 98]. In the template method, cross-correlation function between original signal and the template waveform is calculated, then the peaks of the cross-correlation function is detected as the emergence timings of the template waveform. The cross-correlation function $C(t)$ between an original signal $F(t)$ and an template waveform $f(\tau)$ with a period of T ($0 \leq \tau \leq T$) is defined as

$$C(t) = \frac{1}{\sigma_F(t)\sigma_f} \int_{-T/2}^{T/2} \left(F(t'-t) - \bar{F}(t)\right) \cdot \left(f(t') - \bar{f}\right) dt'. \tag{3.1}$$

Here, $\sigma_F(t)$ and σ_f are standard deviations of $F(t-\tau)$ and $f(\tau)$ over the fundamental period T, respectively. $\bar{F}(t-\tau)$ and $\bar{f}$ are averaged values of them.

The cross-correlation function is normalized and has a value from 0 to 1. Since the cross-correlation function is an indicator of the similarity of two signals, the closer the value of the correlation function is to 1, the more similar the two signals are. That is, when the cross-correlation function peaks at a certain time t_j, it can be detected as the emergence time of the template waveform because the original signal and the template waveform match well at that time.

While there is a typical template waveform in Electrocardiogram analysis, template waveforms are generally unknown in turbulent fluctuation, hence additional analysis is required. The workflow of the template method in turbulent fluctuation is shown in Figure 3.2. First, a initial template to apply the template method for turbulent fluctuation is necessary. For example, the initial template can be determined by $f_0(\tau) = \frac{1}{N}\sum_{i=0}^{N} F(\tau + iT)$. Next, the cross-correlation function between the original signal and the initial template f_0 is calculated, and sub-signals for each time T for original signal based on peaks of the cross-correlation function are extracted and averaged them. The new template waveform $f_1(\tau)$ is obtained in the first cycle of the calculation. Then, using the $f_1(\tau)$, the same calculation does and, the new template waveform $f_2(\tau)$ is obtained in the second cycle of the calculation. Finally, the template is converged, iterating calculation cycles described above.

An example of the actual application of the template method to PANTA experimental data is shown in Figure 3.3. Ion saturation current is used as a original signal and cosine wave with frequency of coherent fluctuation is used as a initial template waveform for simplicity since the observed fluctuation has sinusoidal-like waveform. The template waveforms obtained during the iterative process of the template method is shown in Fig. 3.3 (c). In

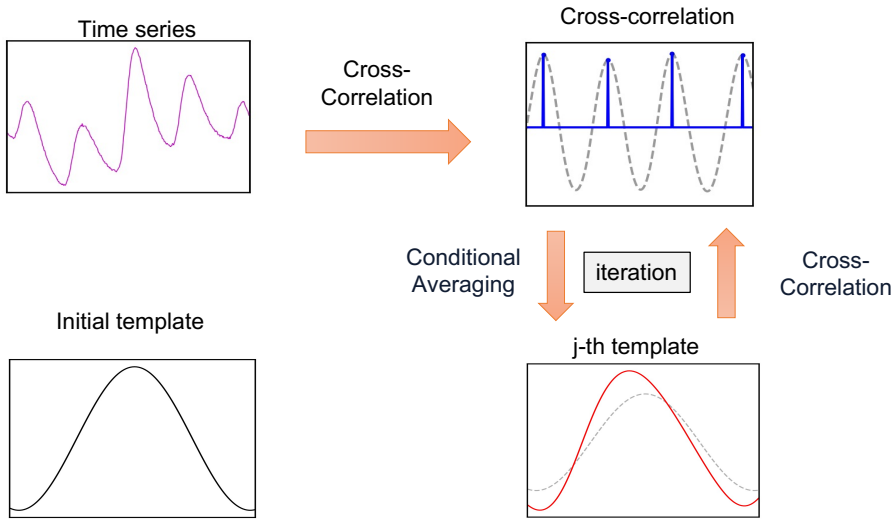

Figure 3.2: Schematic diagram of the template method workflow. The template waveform is determined through the j-th iteration.

this case, the template waveforms converged immediately and the iteration is terminated after the third time, but more iterations are required in some cases [99, 100]. The obtained template waveform is distorted compared to pure sinusoidal wave, that is, the nonlinear waveform due to higher harmonics can be obtained by the template method. Cross-correlation function between the original signal and the converged 3-rd template is shown in Fig. 3.3 (b). Indeed, at the timings of the cross-correlation function peaked, it can be seen the converged waveform appear in the original signal.

3.3 Advantages of the template method

The advantages of the template method are that it can not only detect arbitrary waveforms such as nonlinear waves [99–101], but also evaluate the instantaneous frequency of the waveform. The detection and evaluation of the nonlinear wave with higher harmonics is described before section. In this section, as the other advantage of the template method, the instanta-

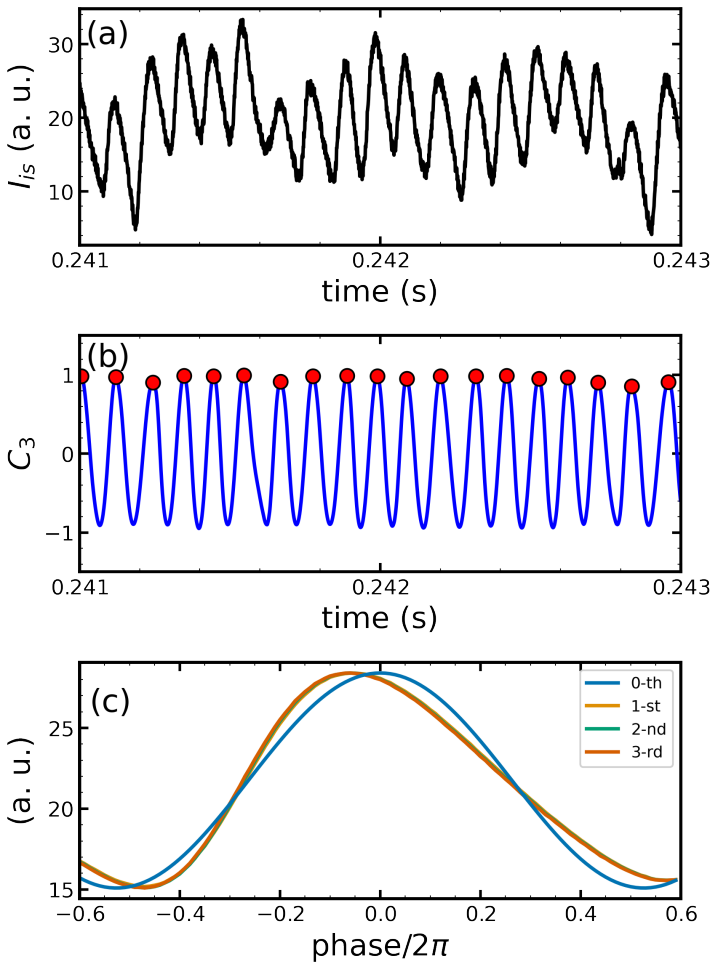

Figure 3.3: (a) time series of ion saturation current fluctuation. (b) Cross-correlation function between the ion saturation current and the 3-rd template waveform. (c) j-th template waveform obtained during the iteration process. In this case, cosine wave is chosen as the initial (0-th) template.

neous frequency analysis using the template method is presented.

The two-dimensional power spectrum of density fluctuation observed in PANTA has a width in the frequency direction, as shown in Figure 2.5. The full width at half maximum of the (m, f) = (4, 9.4 kHz) is about 500Hz. The frequency width could be caused by variation in time of the instantaneous frequency of the turbulent fluctuation. In order to check whether the instantaneous frequency is changed in time, the template method is applied. Then, the time evolution of instantaneous frequency is evaluated from the waiting times of the emergence timing t_j of the template waveform, as illustrated in Figure 3.4. Here, t_j is the j-th detected timing and instantaneous frequency is defined as $1/(t_j - t_{j-1}) = 1/T_j$. The results of the instantaneous frequency analysis is show in Figure 3.5 (a)-(c). It is found that the instantaneous frequency fluctuate in time and seems to gradually increase the averaged instantaneous frequency. The increase in the mean value is at 500 Hz which is coincided with the frequency width of the power spectrum. The changes of the instantaneous frequency can be caused by changes of the pressure, Doppler shift due to flow, noise and so on. The increase in the average instantaneous frequency may be caused by the background pressure change because the time scale of the changes is much slow.

In order to investigate the statistical features of the time evolution of the instantaneous frequency fluctuation,the probability density function of the instantaneous frequency and the power spectrum density were evaluated. The histogram of the instantaneous frequency is shown in 3.6 (a). The mean value of the instantaneous frequency is 9.5 kHz and the standard deviation is about 1.0 kHz. The standard deviation is larger than the frequency width of the power spectrum density. The skewness and kurtosis as defined by Fisher statistics are 0.29 and -0.32, respectively, and it is found to deviate

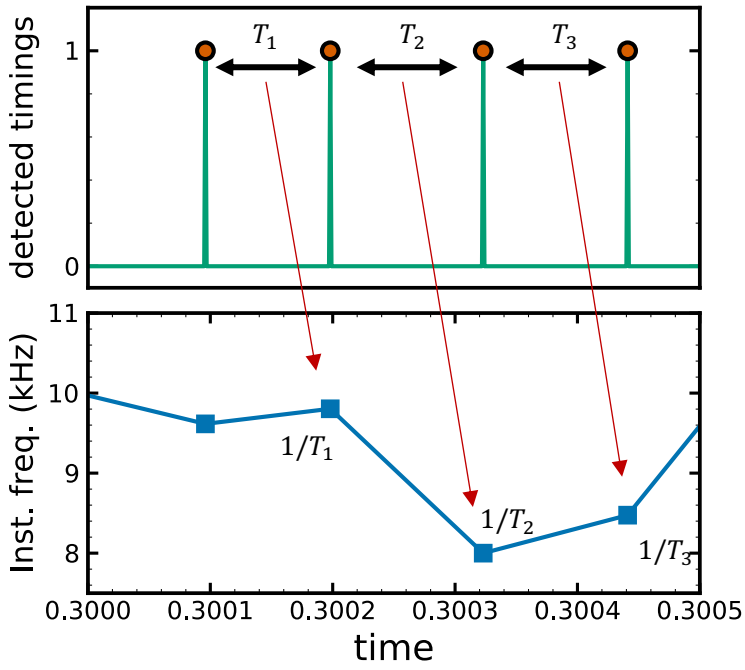

Figure 3.4: Schematic diagram of the instantaneous frequency evaluation using the detected timings of the fluctuation.

from the Gaussian distribution. These results suggests that there is variation other than the increase in the mean value or Gaussian noise.

As can be seen from Figure 3.5 (c), the time variation of the instantaneous frequency also appears to be periodic. Since the time evolution of the instantaneous frequency is unequally spaced in time, the power spectrum of the instantaneous frequency is evaluated by the Lomb-Scargle method as show in Figure 3.6 (b). This analysis shows that there is a peak in the spectrum at 1.7 kHz, indicating that the instantaneous frequency fluctuates at a specific frequency of 1.7 kHz. The frequency of 1.7 kHz is consistent with the frequency of the fluctuation with $m = 1$ that coexists with the (m, f) = (4, 9.4 kHz) fluctuation, suggesting that the instantaneous frequency of the (m, f) = (4, 9.4 kHz) is fluctuating due to the interaction with the (m, f) = (1, 1.7 kHz) fluctuation. Instantaneous frequency fluctuations and their statistical properties were revealed for the first time by instantaneous fre-

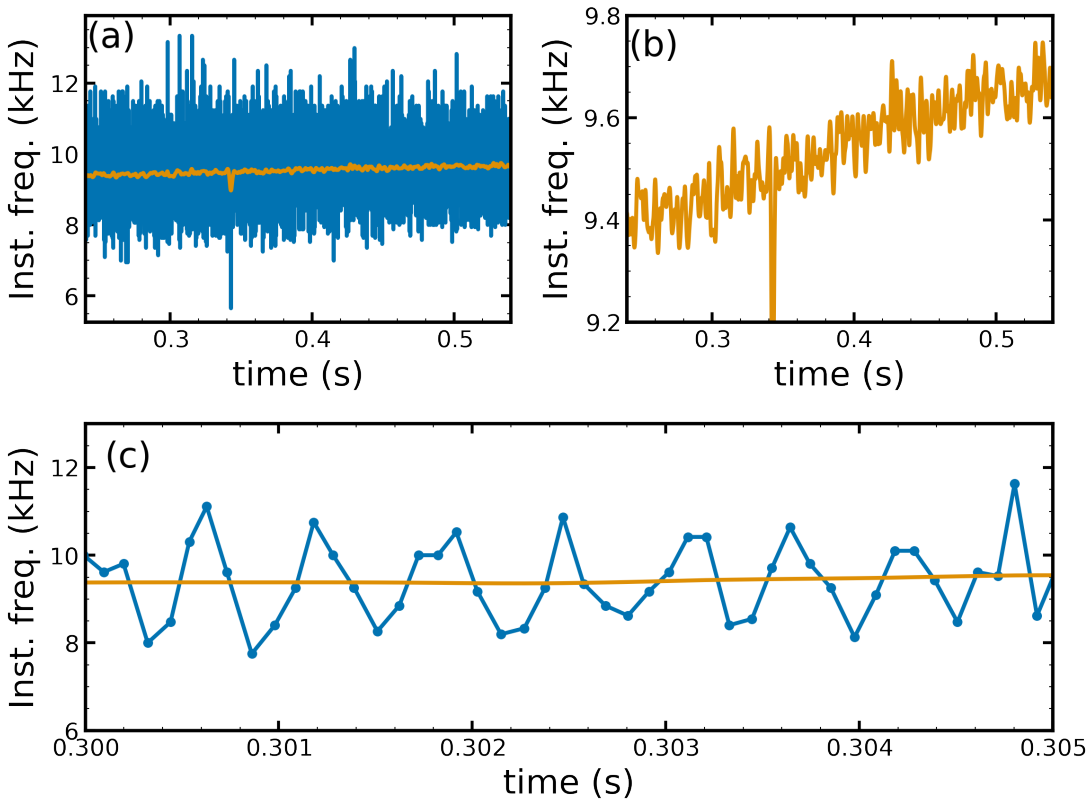

Figure 3.5: (a) Time evolution of the instantaneous frequency. Blue line means variation of the instantaneous frequency, and the orange line means the low-pass-filtered variation. (b) Plot with the low-pass-filtered variation extracted. (c) Enlarged view of (a)

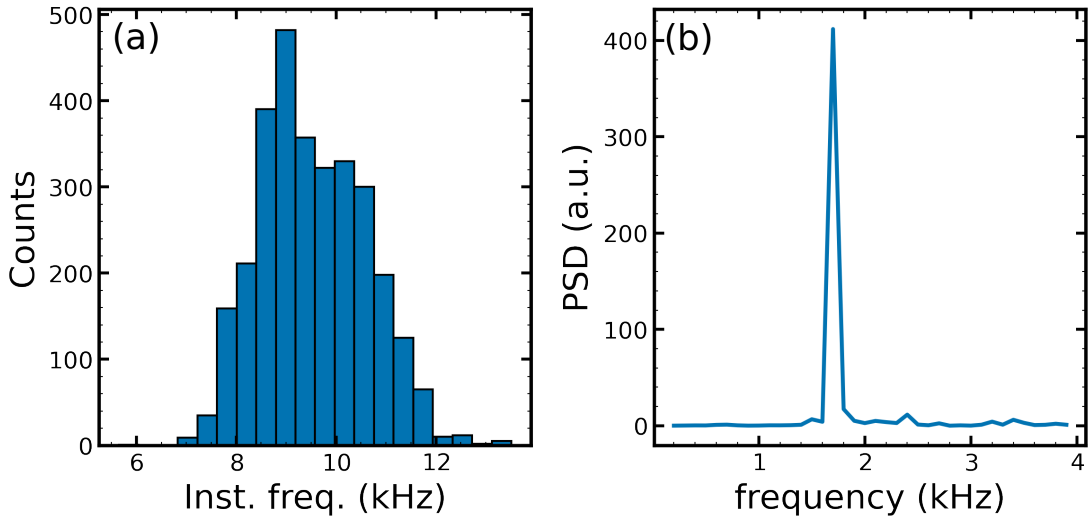

Figure 3.6: (a) Histogram and (b) power spectrum density, of instantaneous frequency obtained from the template method.

quency analysis with high time resolution using the template method. The observed results cannot be revealed by conventional Fourier analysis or non-stationary wavelet analysis, which are limited by the uncertainty principle. Hence, the template method is very effective for non-stationary fluctuation analysis.

3.4 validation of the template method

This section presents the validation study of the template method comparing to the conventional methods. In the subsection 3.4.1, detection precision of the template method and the threshold method is compared for the experimental data in which sinusoidal wave is observed. Subsection 3.4.1 shows the comparison study of conditional sampling based on the template method and the Fourier analysis in fluctuation driven transport analysis, in order to validate whether the spatiotemporal structure is correctly extracted.

3.4.1 A comparison between the template method and the conventional threshold method

As mentioned in the previous section, the template method has an advantages that it can applied to arbitrary waveform, compared to the threshold method. Here, a comparison study between the template method and threshold method is presented.

Firstly, the comparison study was performed by using the test signal of $x(t) = \sin(2\pi f_1 t) + \sin(2\pi f_2 t) + \text{noise}$, where $f_1 = 1\,\text{Hz}$, $f_2 = 1\,\text{Hz}$, and the noise expresses the Gaussian noise with a standard deviation of 0.02, as shown in Figure 3.7(a). In the template method, the cosine wave of the 10 Hz was chosen to detec the 10 Hz fluctuation. The detected timings by the template method (orange) and threshold method with two different values of 1 (green) and 0.8 (magenta) are shown in Figure 3.7(b). There is a possibility of count error depending on the noise level and threshold values in the threshold method and another algorithm avoiding count error due to noise (e.g. smoothing) and threshold value are required for the threshold method [45–50]. Indeed, counting errors are occurs in the threshold method as shown in Figure 3.7 of histogram of the instantaneous periods. The ion saturation current observed by PANTA was used for the validation as the previous section. The template method and the threshold method with two threshold values 0.2 and 0.22 are also applied to the ion saturation current as shown in Figure 3.8 (a) and (b). Figure 3.8 (c) of the histogram of the instantaneous period shows the threshold methods often miss the detection as the doubling and tripling of instantaneous periods, while the template method does not miss the counting. Thus, it was validated that the template method has an advantage over the threshold method in that it can be applied to any waveform.

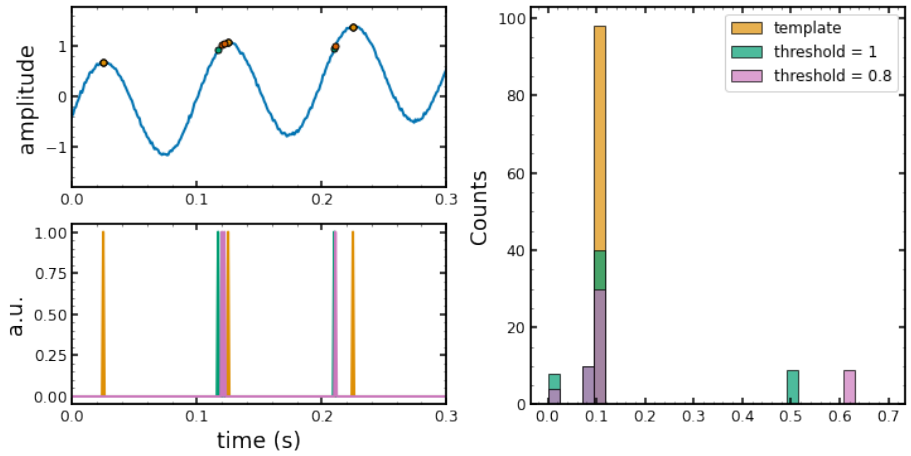

Figure 3.7: (a) Test signal for the comparison study between the template method and the threshold method. (b) Detected time-to-peak indicated by delta functions. (c) Instantaneous periods of the fluctuation pattern with each method. The template method is represented as the color of orange and the threshold method is represented as the color of green for threshold value 1 and the color of magenta for threshold value 0.8.

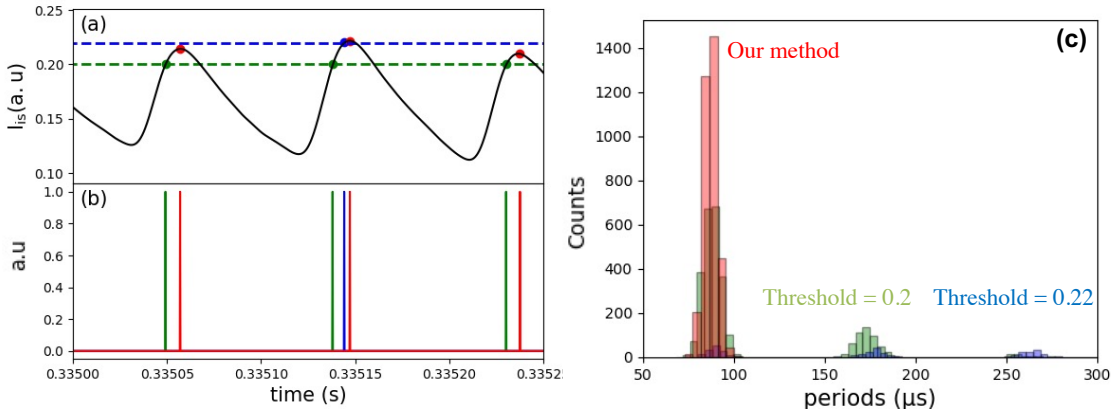

Figure 3.8: (a) Ion saturation current used for the comparison study and (b) detected time-to-peak indicated by delta functions. (c) Instantaneous periods of the fluctuation pattern with each method. The template method is represented as the color of red and the threshold method is represented as the color of green for threshold value 0.2 and the color of blue for threshold value 0.22. The dashed lines in (a) indicates the threshold values for the threshold method.

3.4.2 A comparison between conditional sampling based on the template method and the Fourier analysis, in fluctuation driven transport analysis

The template method was developed to apply the conditional sampling method to arbitrary waveforms. Conditional sampling allow us to evaluate the spatiotemporal evolution of turbulent fluctuation. Moreover, from the evaluated spatiotemporal structure, the fluctuation-driven transport can be estimated.

Net cross-field fluctuation-driven particle flux is written as

$$\overline{\Gamma_r} = \overline{\tilde{n}\tilde{v}_{E\times B}(t)} = -\frac{1}{B}\overline{\tilde{n}\partial_\theta\tilde{\phi}(t)} \tag{3.2}$$

where $\tilde{n}$ and $\tilde{\phi}$ are density and potential fluctuations, respectively. Here, positive flux $\overline{\Gamma_r} > 0$ means out ward flux while negative flux $\overline{\Gamma_r} < 0$ means inward flux. When phases difference between density and potential fluctuations exist, net cross-field particle flux is driven by $E \times B$ flow.

Conventionally, the particle flux is evaluated the phase difference of the density and potential by Fourier analysis. The particle flux in frequency domain is written as,

$$\overline{\Gamma_r} = \frac{2}{B}k_\theta \int_{f+\Delta f/2}^{f+\Delta f/2} \gamma_{\tilde{n},\tilde{\phi}(f')} \left|P_{\tilde{n}}(f')\right|^{1/2} \left|P_{\tilde{\phi}}(f')\right|^{1/2} \sin(\alpha_{\tilde{n},\tilde{\phi}(f)})df', \tag{3.3}$$

where f and Δf are frequency of fluctuation and frequency resolution, respectively. $\gamma_{\tilde{n},\tilde{\phi}}$ and $\alpha_{\tilde{n},\tilde{\phi}}$ are coherence and cross-phase calculated by cross spectrum between density and potential fluctuations. $P_{\tilde{n}}$ and $P_{\tilde{\phi}}$ are power spectrum of density and potential fluctuations, respectively.

In order to validate the transport analysis by conditional sampling, comparison study between conditional sampling and Fourier analysis in fluctuation-driven transport analysis were perform. For the transport analysis using of

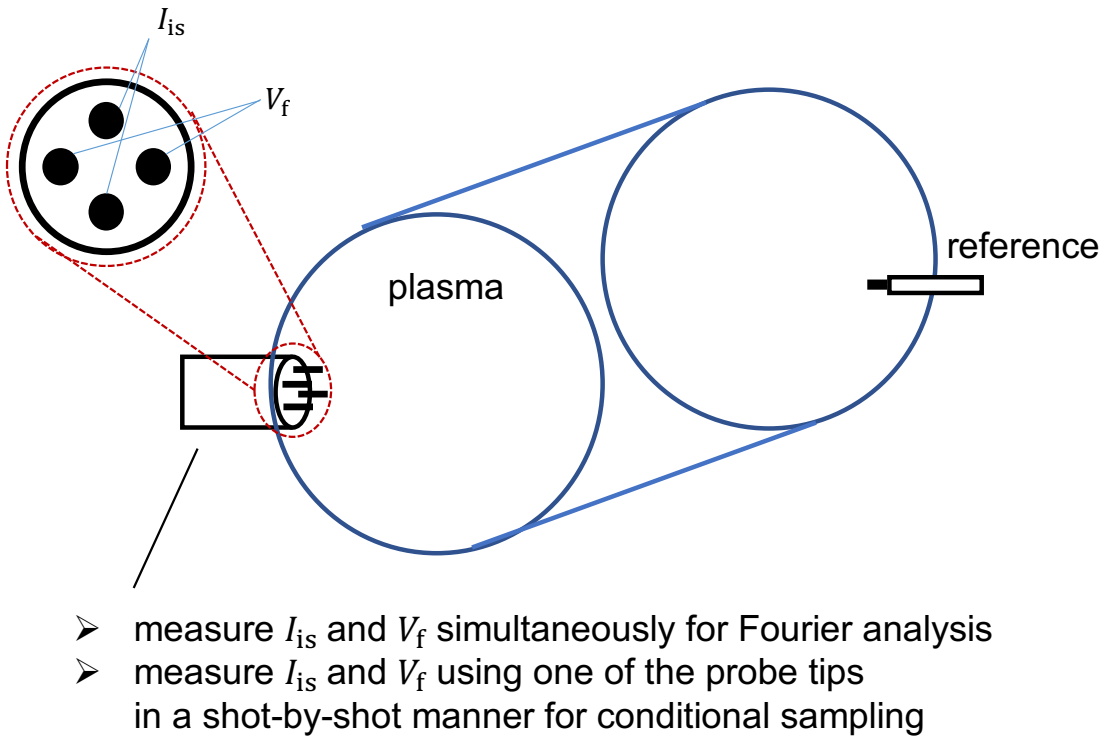

Figure 3.9: Illustration of probe setup for this comparison study.

Fourier analysis, observation of density fluctuation and potential fluctuation at the same time and at the same position is required. Using a probe array with 4 pins, ion saturation currents and floating potential are measured as shown in figure3.9. By averaging the two measured floating potentials and the two measured ion saturation current, the potential fluctuation at the same position as the density fluctuation was obtained, and Fourier analysis are applied to them. Then, the spectrum of the particle flux was obtained.

For the transport analysis based on conditional sampling, ion saturation current and floating potential were measured in a shot-by-shot manner, using one of the four tip probe 3.9. Another ion saturation current was also measured simultaneously by a fixed probe as a reference signal. The template method was applied to the reference signal, then, the spatiotemporal

structure of the density and potential at the same time and same location was evaluated by conditional averaging. Assuming that the fluctuation patterns rotates in the electron diamagnetic direction as rigid-body, the differential operator in the Eq. (3.2) can be replaced $-\partial_\theta$ to ∂_t, and the instantaneous particle flux is written as

$$\Gamma_r(t) = -\frac{1}{B}\left\langle \tilde{n} \right\rangle_{CS} \left\langle \frac{\partial \tilde{\phi}(t)}{\partial t} / \frac{\partial \theta}{\partial t} \right\rangle_{CS} = \frac{k_\theta}{2\pi f B}\left\langle \tilde{n} \right\rangle_{CS} \left\langle \partial_t \tilde{\phi}(t) \right\rangle_{CS}, \tag{3.4}$$

where $<>_{CS}$ denotes conditional sampling. In this way, time evolution of the particle flux can be estimated by using conditional averaging based on the template method. Then, the net particle flux is evaluated from time-average of the instantaneous particle flux.

Figure 3.10 shows the radial profiles of the time-averaged particle fluxes. Both the particle fluxes obtained by Fourier analysis and conditional sampling method are inward, and their absolute values are the largest at r = 2.5 cm. Thus, the Fourier analysis and conditional sampling methods yielded similar results. In detail, the absolute value of the particle flux obtained by the conditional average method is larger than that obtained by the Fourier analysis, which only takes out the fundamental frequency component of the oscillation, and smaller than that obtained by integrating all the frequency components. This indicates that the particle flux obtained by the conditional sampling method contains higher harmonic components and is larger than the result of the fundamental frequency component alone. By using the 4-tip probe, the time evolution of the instantaneous particle flux can be directly measured. The conditional averaged instantaneous particle flux is also evaluated as shown in Fig. 3.10. The evaluated particle flux is almost same profile compared to the particle flux evaluated from the conditionally averaged density and potential. These results validate that the transport evaluation method using the template method is almost consistent with the

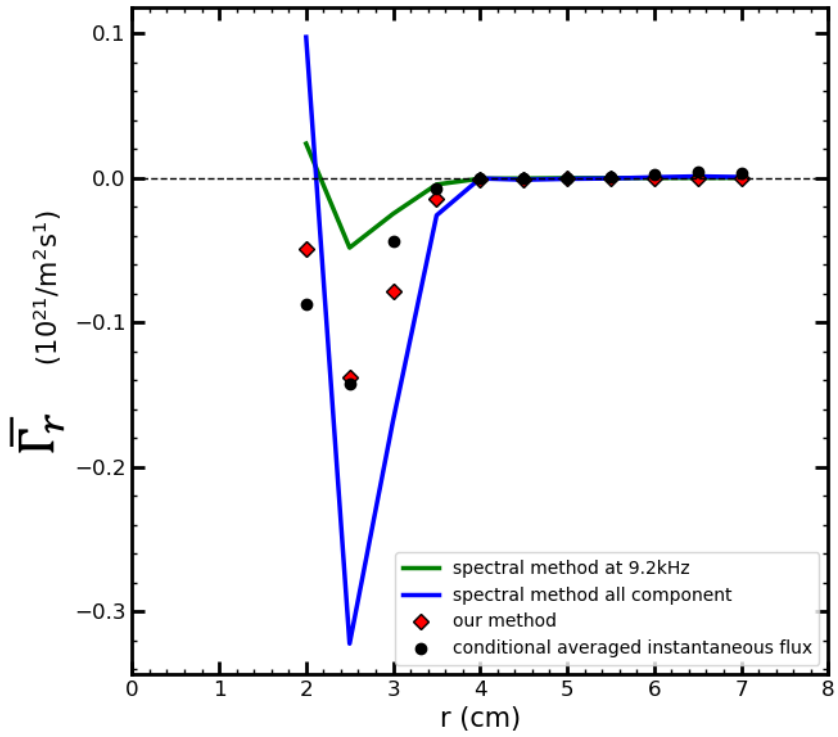

Figure 3.10: (a) A comparison of radial profiles of averaged particle flux. Green line and blue line indicate particle flux estimated by spectral analysis. Green line consists of only the fundamental frequency component of the coherent mode. Blue line consists of all frequency components. Black dots are conditional averaged instantaneous flux and red diamonds indicate particle flux estimated by the conditional averaged density and potential. Conditional averaging based method include the fundamental frequency components and its synchronizing components (e.g. higher harmonics).

conventional method. It is also shown that the conditional sampling has an advantage in that the degree of freedom can be reduced for particle flux containing harmonics such as nonlinear waves [28, 102, 103].

Chapter 4

Application of conditional sampling based on the template method to turbulent fluctuation

Chapter 3 describes the development of the template method as an extension of conditional sampling to arbitrary waveforms. The conditional sampling method allows us to analyze the non-stationary signal such as turbulent fluctuation. Indeed, it was found that the instantaneous frequency is fluctuated in time observed in PANTA, that is, the observed fluctuation is quasi-periodic as mentioned in subsection 3.3. In this chapter, the results of applying conditional sampling based on the template method, to the quasi-periodic turbulent fluctuations are presented.

Section 4.1 shows the spatiotemporal dynamics of the density, potential, and electron temperature fluctuations. Although the measurement of electron temperature fluctuations generally has poor time resolution, conditional sampling was used to improve the time resolution of them. Based on the spatiotemporal dynamics of density, potential, and temperature, fluctuation-driven particle and heat transports are evaluated. The instabilities of the fluctuation is discussed based on the characteristics of the obtained spatiotemporal dynamics.

The discovery of nonlinear dynamics between two different types of tur-

bulent fluctuations is presented in Section 4.2. The intermittent competition between the two fluctuations was observed in the instantaneous wavenumber spectrum. The time evolution of nonlinear energy transfer in the intermittent bursts was evaluated by combining the conditional sampling, bicoherence analysis and so on. Furthermore, the intermittent competition was found to synchronize with a low-frequency potential fluctuation. This suggests that the nonlinear dynamics may be resulted by the interaction of the three fluctuations. Possible explanation of mechanism of the nonlinear dynamics is also discussed.

4.1 Identification of spatiotemporal dynamics of fluctuation

Plasma turbulence is linearly excited by gradients in density and temperature, and then saturates through nonlinear processes to create complex structures. The resulting nonlinear waves can evolve in time with non-sinusoidal waveforms [28, 102–104]. In fact, as described in Section 3, the fluctuation observed by PANTA has a nonlinear waveform with higher harmonics. In this case, the spatial structure can also have a distorted structure. Here, the results of the reconstruction of the spatiotemporal dynamics of two kinds of coexisting fluctuations by applying the conditional extraction method, are reported.

4.1.1 Evaluation of electron temperature fluctuation

In low-temperature plasmas, such as in basic plasma devices and scrape-off layers, electrostatic probe can be used for measuring electron temperature. In the single probe and double probe methods, a current-voltage characteristic curve is obtained by biasing swept voltage to the electrodes. By fitting

the exponential function to the current-voltage characteristics, the electron temperature and other parameters can be evaluated, as reviewed in Section 2.2. The time resolution of these measurements is determined by the frequency of the swept voltage. Since the frequency of turbulent fluctuations is several kHz to several hundred kHz, it is desirable to sweep the voltage at ~ 1 MHz. However, when the voltage is applied at a high frequency, the current-voltage characteristics are distorted by the stray capacitance, etc., and this affects the evaluation of the parameters [31].

In order to evaluate the parameters correctly at high sweep frequency, it is necessary to compensate for the distortion of the current-voltage characteristics [105–107]. The triple probe method can measure electron temperature in high temporal resolution, assuming each tip of a triple probe is aligned at the same plasma potential. The assumption makes it difficult to measuring electron temperature fluctuation in small scale basic device. That's why it is still challenging to measure electron temperature fluctuations.

Another idea for electron temperature fluctuation measurement is to use the conditional sampling method to improve the time resolution of double-probe measurements with low time resolution, as described in Chapter 3. But, conditional sampling is applicable for spiky waveform with large amplitude, In this study, the template method is developed to apply conditional sampling to arbitrary waveforms, and it allows us to evaluate electron temperature fluctuations such as nonlinear waves.

A probe setup for evaluating electron temperature fluctuations with double probe is shown in Figure 4.1. The double probe measurement was carried out to measure the electron temperature and electron density. The frequency of the sweep voltage was set to 100 Hz. As a reference signal, ion

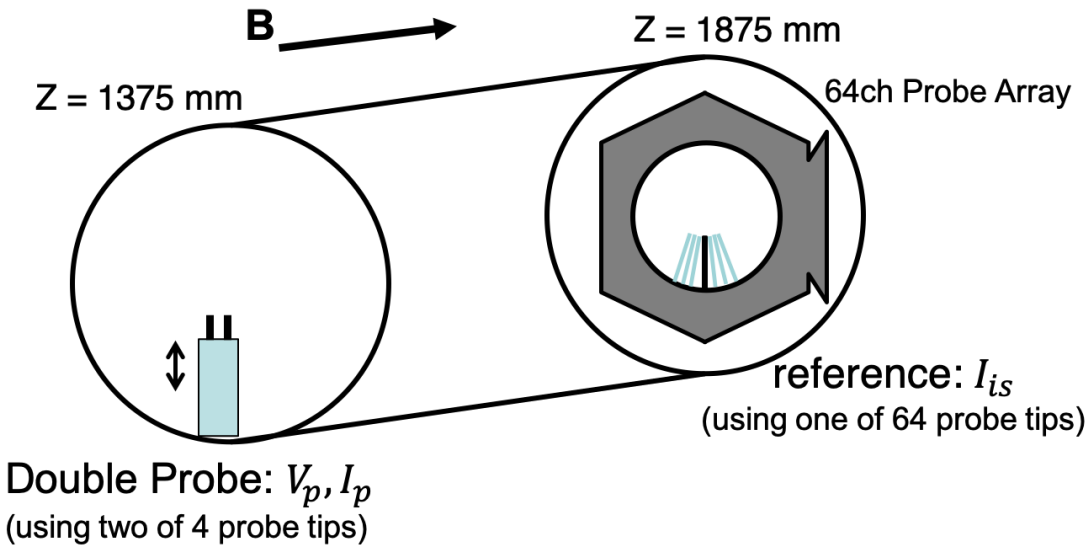

Figure 4.1: Illustration of probe setup for the electron temperature fluctuation measurement.

saturation current was measured by the one of the probe tips of the 64ch probe simultaneously. Then, the template method is applied to the reference signal. Here, the $m = 4$ fluctuation is the target of the analysis (see fig. 2.5). The reference signal and the cross-correlation function obtained from the template method are shown in Figures 4.2 (a) and (b). Figures 4.2 (c) and (d) show the time evolution of double probe current $I_{\rm p}$ and bias voltage $V_{\rm p}$ measured at r = 30 mm. The $I_{\rm p}$ is strongly fluctuated by the turbulent fluctuation. Figure 4.3 shows the $I_{\rm p} - V_{\rm p}$ curve for one voltage sweeping. It can be seen that the observed characteristics has large deviation due to the fluctuation.

Based on the detected timings of the template waveform represented as red dots in Figure 4.2 (b), the probe current and the probe voltage are conditionally sampled at each time delay τ from the detected timings. Figures 4.4 (a)-(f) show the conditionally sampled $I_{\rm p} - V_{\rm p}$ characteristics obtained from data for many voltage sweepings. The $I_{\rm p} - V_{\rm p}$ characteristic for each τ

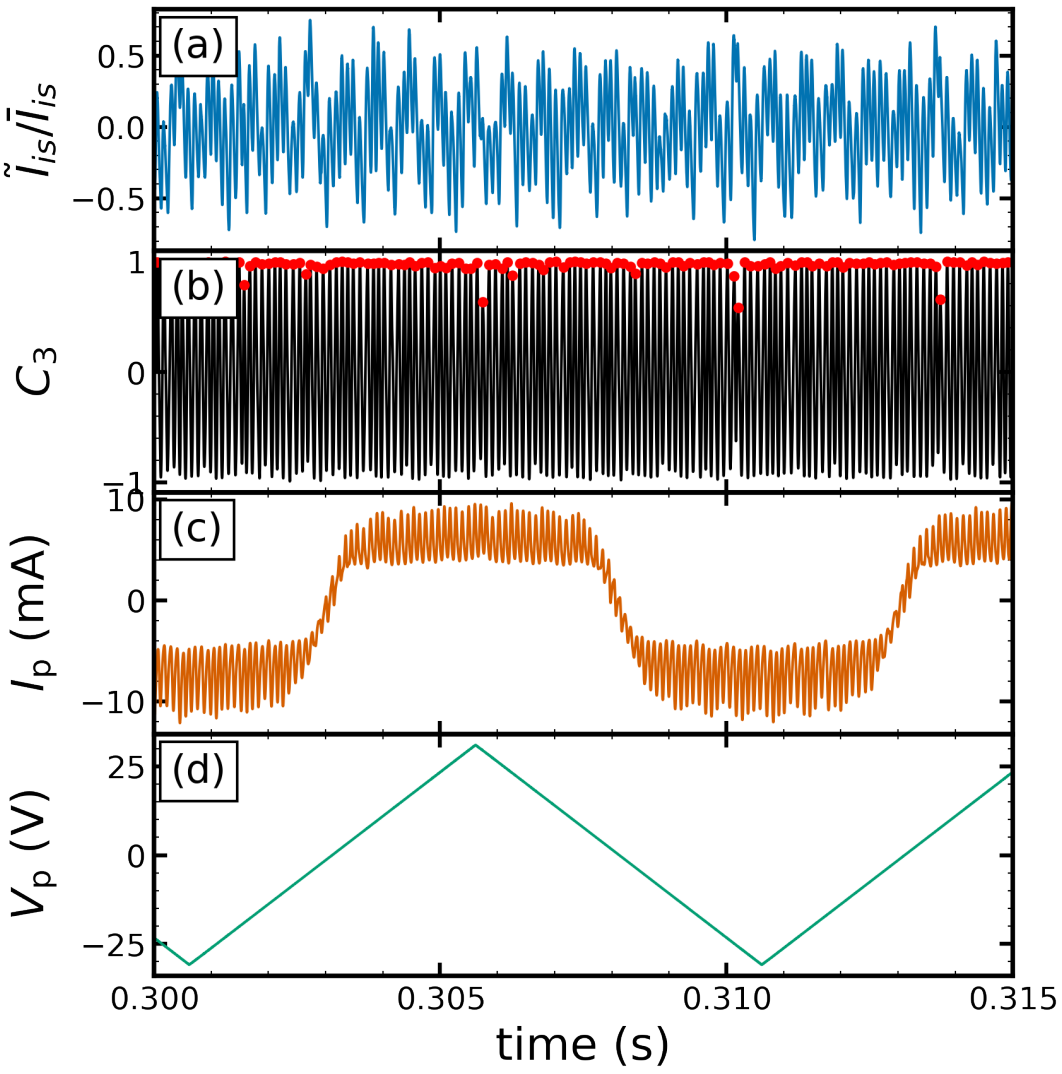

Figure 4.2: Time evolution of (a) normalized ion saturation current used as a reference signal, (b) cross-correlation function, (c) probe current and (d) probe voltage. Red dots in (b) are the peaks of cross-correlation function, which is used as the trigger timings for conditional sampling.

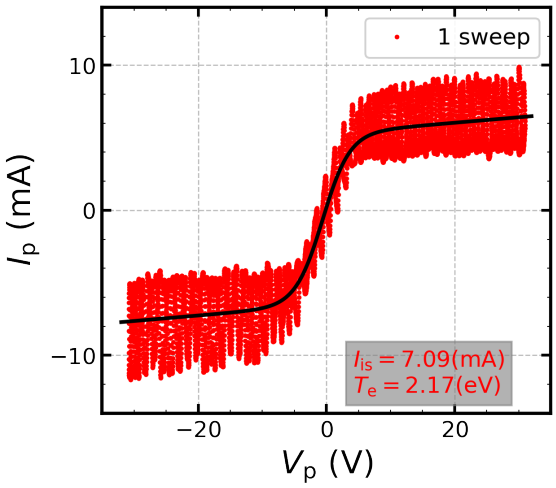

Figure 4.3: $I_p - V_p$characteristic for one sweep obtained by the double probe measurement. Dots are experimental data, and a solid line is a curve obtained by fitting equation (2.16) with nonlinear regression.

has a different shape. The parameters obtained by nonlinear regression to equation (2.16), i.e., ion saturation current and electron temperature, also change with each τ.

Time evolution of electron temperature and ion saturation current were evaluated from the conditionally sampled $I_p - V_p$ characteristics at each τ as shown in Figure 4.5. Electron temperature fluctuation was successfully observed by applying the conditional sampling method. Ion saturation current was also evaluated simultaneously. In order to verify the conditional sampling of double probe, ion saturation current measurement was also performed in the same experimental condition. Then, Conditional averaging was applied to the ion saturation current. A comparison of the normalized waveforms obtained by conditional sampling and averaging is shown in figure 4.6. Since the waveforms obtained by conditional sampling agree with the waveform obtained by conditional averaging in the range of error bars, the conditionally sampled double probe $I_p - V_p$ characteristics is cor-

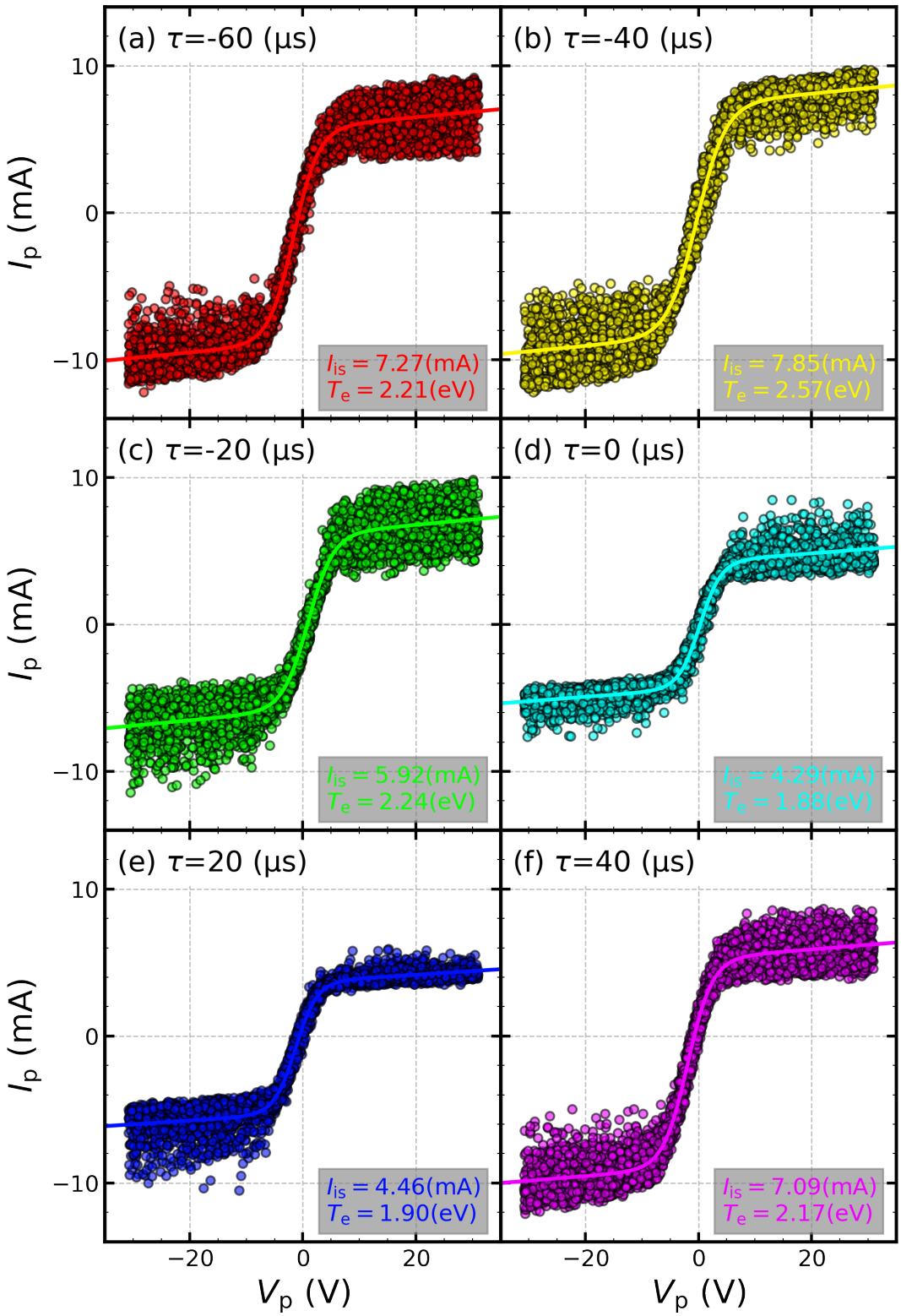

Figure 4.4: Conditionally sampled double probe $I_p - V_p$ characteristics at each time lags τ from the emergence timings. Dots are experimental data, and solid lines are curves obtained by fitting equation (2.16) with nonlinear regression.

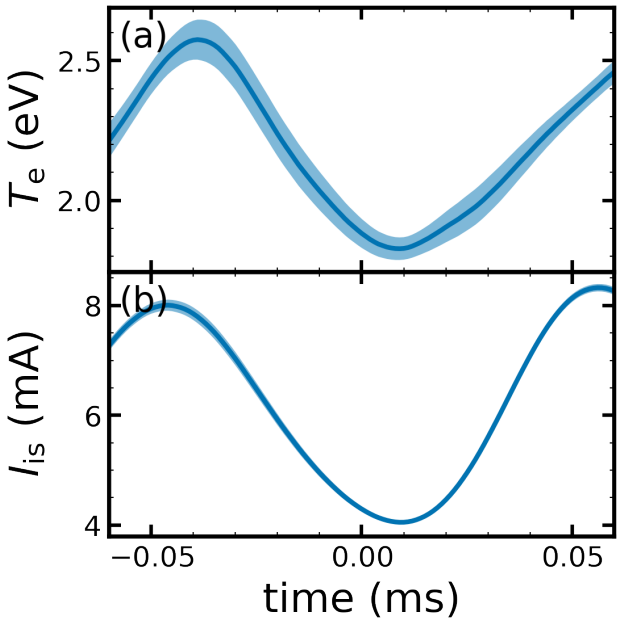

Figure 4.5: Temporal evolution of (a) electron temperature and (b) ion saturation current. Filled region of each figures indicates standard deviation.

rect and the evaluated electron temperature fluctuation should be correctly evaluated.

Figure 4.7 shows power spectrum density of normalized electron temperature fluctuation $\tilde{T}_e/\bar{T}_e$ and normalized density fluctuation $\tilde{n}_e/\bar{n}_e$. Here,$\tilde{n}_e/\bar{n}_e$ was evaluated as $\tilde{n}_e/\bar{n}_e \approx \tilde{I}_{is}/\bar{I}_{is} - \frac{1}{2}\tilde{T}_e/\bar{T}_e$. For comparison, $\tilde{I}_{is}/\bar{I}_{is}$ obtained by one of the 64ch probes as a reference signal is also plotted. The power spectrum density of conditional sampled $\tilde{n}_e/\bar{n}_e$ indicate that only the target mode and its synchronized components are extracted without noise, unlike reference $\tilde{I}_{is}/\bar{I}_{is}$. Both $\tilde{n}_e/\bar{n}_e$ and $\tilde{T}_e/\bar{T}_e$ have higher harmonics of the fundamental mode. That is, the conditional sampling successfully evaluated nonlinear waveform of electron temperature fluctuation. The fundamental mode and the second harmonic of $\tilde{n}_e/\bar{n}_e$ are larger than that of $\tilde{T}_e/\bar{T}_e$ while the third and the subsequent harmonics of $\tilde{n}_e/\bar{n}_e$ are smaller than that of $\tilde{T}_e/\bar{T}_e$. This

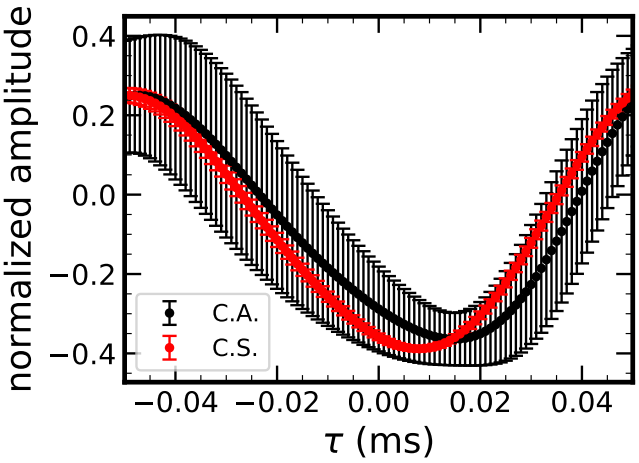

Figure 4.6: Comparison of conditional averaging and conditional sampling. Black dots are evaluated by conditional averaged (C. A.) ion saturation current, and red dots are evaluated by conditional sampled (C. S.) double probe current-voltage characteristics.

can be caused by differences in nonlinear coupling or dissipative processes. The details of the features of the spatiotemporal structure of them are described in the next section.

When the electron temperature fluctuates with a finite amplitude, it can affect the measurement of electron density and spatial potential using the electrostatic probe, as reviewed in Sec. 2.2. In order to verify the effects of the electron temperature fluctuation on density and potential evaluation, floating potential was also measured at the same position as the double probe measurement. Then, using the same reference probe, conditional averaged waveform of the floating potential was obtained. The relationship of Eq. (2.10) between electron density n_{e} and ion saturation current I_{is}, the relationship of Eq. (2.11) between plasma potential V_{s} and floating potentialV_{f} were used for estimating the electron density and plasma potential, respectively.

In order to check the $\tilde{T}_{\mathrm{e}}$ effects on the phase relation, the temporal evolu-

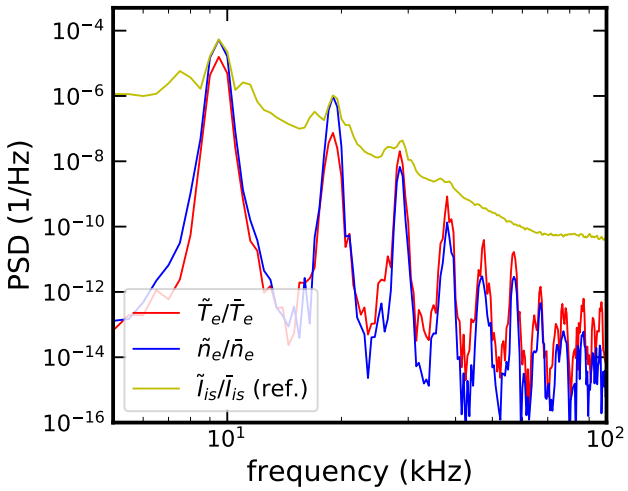

Figure 4.7: Power spectrum density of normalized electron temperature (red line) and density (blue line) obtained by each conditionally sampled waveform. Yellow line is the power spectrum density of ion saturation current used as a reference.

tion of the normalized fluctuations at r = 40 mm are displayed in Figures.4.8 (a) and (b). The normalized density fluctuation $\tilde{n}_\mathrm{e}/\bar{n}_\mathrm{e}$ has the same phase and amplitude as the normalized ion saturation current fluctuation $\tilde{I}_\mathrm{is}/\bar{I}_\mathrm{is}$. Figure 4.8 (c) shows the radial profile of the phase difference $\delta_{I_\mathrm{is},n_\mathrm{e}}$ between the fundamental modes of the $\tilde{n}_\mathrm{e}$ and $\tilde{I}_\mathrm{is}$, which is evaluated by cross-spectrum analysis. The $\delta_{I_\mathrm{is},n_\mathrm{e}}$ is almost 0 at any radial position in the region of $r \geq 20$ mm. Hence, the $\tilde{T}_\mathrm{e}$ effect on $\tilde{n}_\mathrm{e}$ evaluation is negligible, and thus the $\tilde{I}_\mathrm{is}$ can be interpreted as the $\tilde{n}_\mathrm{e}$.

While the $\tilde{T}_\mathrm{e}$ effect on plasma potential ($\tilde{V}_\mathrm{s}$) evaluation is larger than that on $\tilde{n}_\mathrm{e}$ measurement. Concerning the Eq. (2.11), $\tilde{T}_\mathrm{e}$ affects to the $\tilde{V}_\mathrm{s}$ measurement by factor $\alpha \sim 5.2$ for argon plasma. In this case, the amplitude of $\tilde{T}_\mathrm{e}$ is ~ 0.2 eV and the effective voltage $\alpha\tilde{T}_\mathrm{e}/\mathrm{e}$ is ~ 1V. Since the order of magnitude of $\tilde{V}_\mathrm{f}$ is ~ 1V, the $\tilde{T}_\mathrm{e}$ can significantly affect to the V_s evaluation (i.e. $\tilde{V}_\mathrm{f} \neq \tilde{V}_\mathrm{s}$). Indeed, the $\tilde{V}_\mathrm{s}$ is anti-phase with the $\tilde{V}_\mathrm{f}$ as shown in Figs. 4.8 (a)-(b).

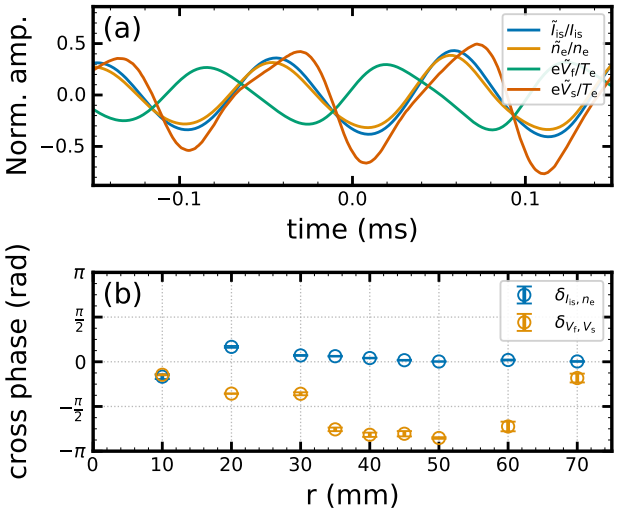

Figure 4.8: Waveforms of the normalized fluctuations of (a) $\tilde{I}_{\mathrm{is}}$, $\tilde{n}_{\mathrm{e}}$, (b) $\tilde{T}_{\mathrm{e}}$, $\tilde{V}_{\mathrm{f}}$, and V_{p} at $r = 40$ mm. (c) Radial profiles of phase differences $\delta_{n_{\mathrm{e}},I_{\mathrm{is}}}$ and $\delta_{V_{\mathrm{p}},V_{\mathrm{f}}}$.

Radial profile of the phase difference $\delta_{V_{\mathrm{f}},V_{\mathrm{s}}}$ between the $\tilde{V}_{\mathrm{s}}$ and $\tilde{V}_{\mathrm{f}}$ are shown in Fig. 4.8 (b). In the region of $r = 30$-60 mm, the large $\delta_{V_{\mathrm{f}},V_{\mathrm{s}}}$ exists with up to $|\pi|$, which may cause that the direction of fluctuation driven flux evaluated by $\tilde{V}_{\mathrm{f}}$ is reversed with respect to one evaluated by $\tilde{V}_{\mathrm{s}}$. Thus, contrary to the $\tilde{n}_{\mathrm{e}}$ measurement, the $\tilde{T}_{\mathrm{e}}$ effect on the $\tilde{V}_{\mathrm{s}}$ measurement is significant.

4.1.2 Conditional averaged spatiotemporal patterns of the fluctuations

Under the experimental condition of this study, two modes rotating with finite azimuthal wavenumber ($m = 1$ and $m = 4$) and a potential fluctuation with azimuthal wavenumber of 0 ($m = 0$) were observed, as shown in Figure 2.5. With a finite azimuthal wavenumber, fluctuation can drive turbulent transport in magnetized plasma. Here, in this subsection, the results of evaluating the spatiotemporal structure of the two rotating fluctuation using conditional sampling.

Double probe measurement and floating potential measurement were

carried out in shot-by-shot manner by using the two tips of probe as shown in Fig. 4.1. Each measurement were alternated for each discharge. Moreover, the measurement position was scanned in the radial direction in shot-by-shot manner. Simultaneously with the double probe measurement or floating potential measurement, ion saturation current was measured by one of the probe tips of the 64ch probe, as a reference for conditional sampling.

The radial-temporal structure of the fluctuation can be reconstructed by conditional sampling the signal obtained from each discharge at each measurement or measurement position obtained for each discharge based on the reference signal. Electron density fluctuations were evaluated from ion saturation current and electron temperature using the Eq. (2.10). Plasma potential fluctuations were evaluated from floating potential and electron temperature using the Eq. (2.11).

Figures 4.9 (a)-(f) show radial-temporal structures of the $m = 4$ mode. Spatiotemporal patterns of density, temperature and potential fluctuations are identified by conditional sampling. It seems that the normalized fluctuation component of all of density, temperature and potential are localized around r = 40 mm, where the density gradient-scale-length is small. The radial profiles of normalized amplitudes are evaluated by root mean square value as shown in Figure 4.10. Indeed, the normalized amplitudes are localized at around r = 40 mm. The amplitude of the density fluctuation is about 30 % and that of potential fluctuation is about 40 %. The amplitude of electron temperature fluctuations is small compared to the amplitude of electron density and potential fluctuations, with a value of 10 %. The shapes of the eigenfunction are similar for all physical quantities. The full width at half maximum is about 16 mm.

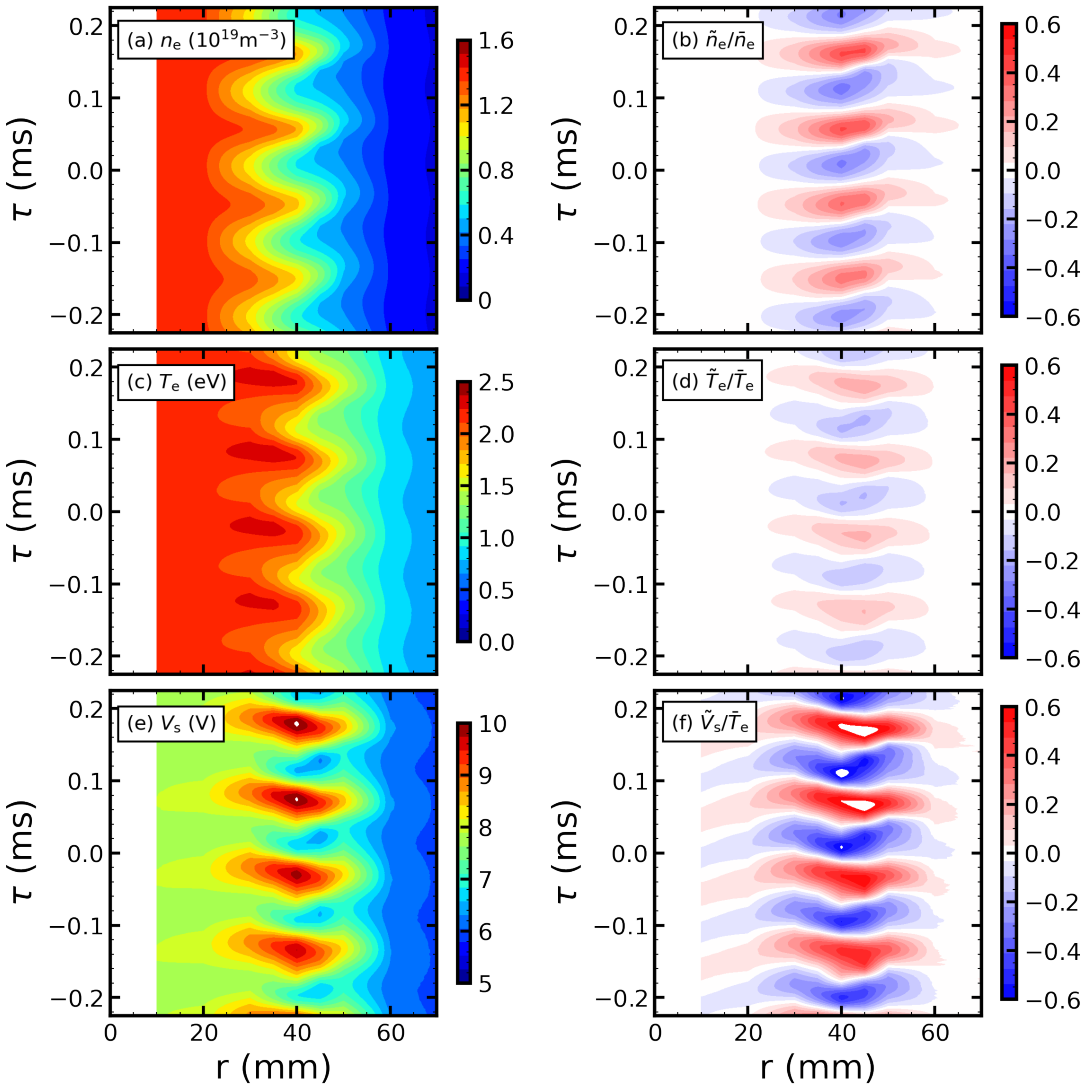

Figure 4.9: Spatiotemporal dynamics of (a) electron density, (c) electron temperature, and (e) plasma potential for the $m = 4$ mode. Those of their normalized fluctuations are shown in (b), (d), and (f).

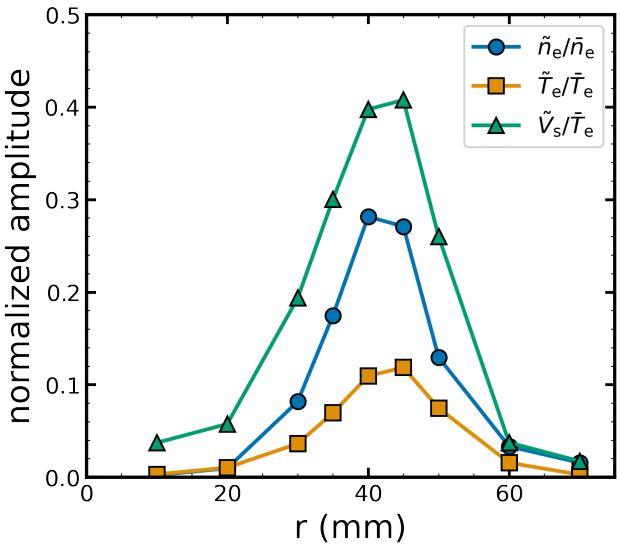

Figure 4.10: Radial profiles of the normalized amplitudes of the $m = 4$ mode.

The radial phase differences are finite, which is suggested that the $m = 4$ mode radially propagates or rotates azimuthally with distorted wavefront. Because the $m = 4$ mode is localized, it is considered that the $m = 4$ mode rotates with distorted wavefront rather than radially propagates. The wavefront distortion in time is different at each radii. It is indicate that the nonlinear coupling with higher harmonics is different at each radii, and may cause the radial wavefront distortion. Indeed, the strength of squared bicoherence of higher harmonics at r = 40 mm is larger than that at r = 30 mm, as shown in Figure 4.11.

Assuming the fluctuations rotate in the electron diamagnetic direction as rigid-body with $m = 4$ structure, the cross-section image can be reconstructed as shown in Figure 4.12. The cross-section images demonstrate that the fluctuation patterns have distorted wavefront in space, that is, twisted. The wavefront distortion is related to nonlinear coupling. They have finite radial wavenumber k_r which are roughly estimated as 20 m^{-1}.

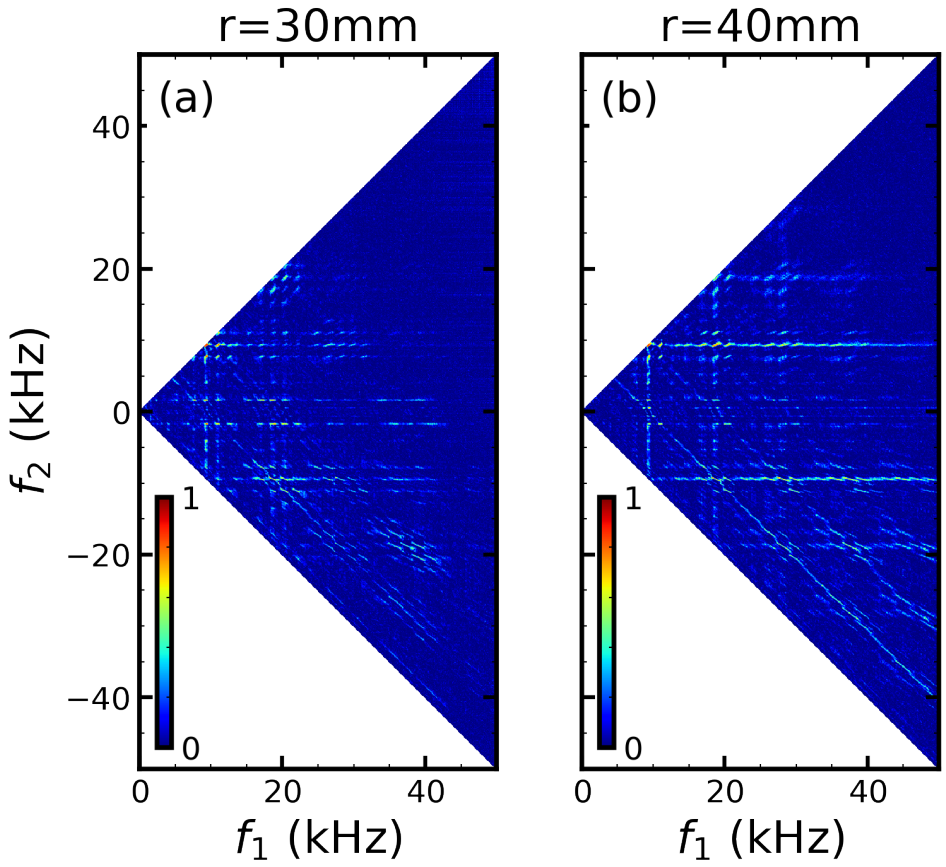

Figure 4.11: Squared bicoherence at (a) r = 30 mm and at (b) r = 40 mm.

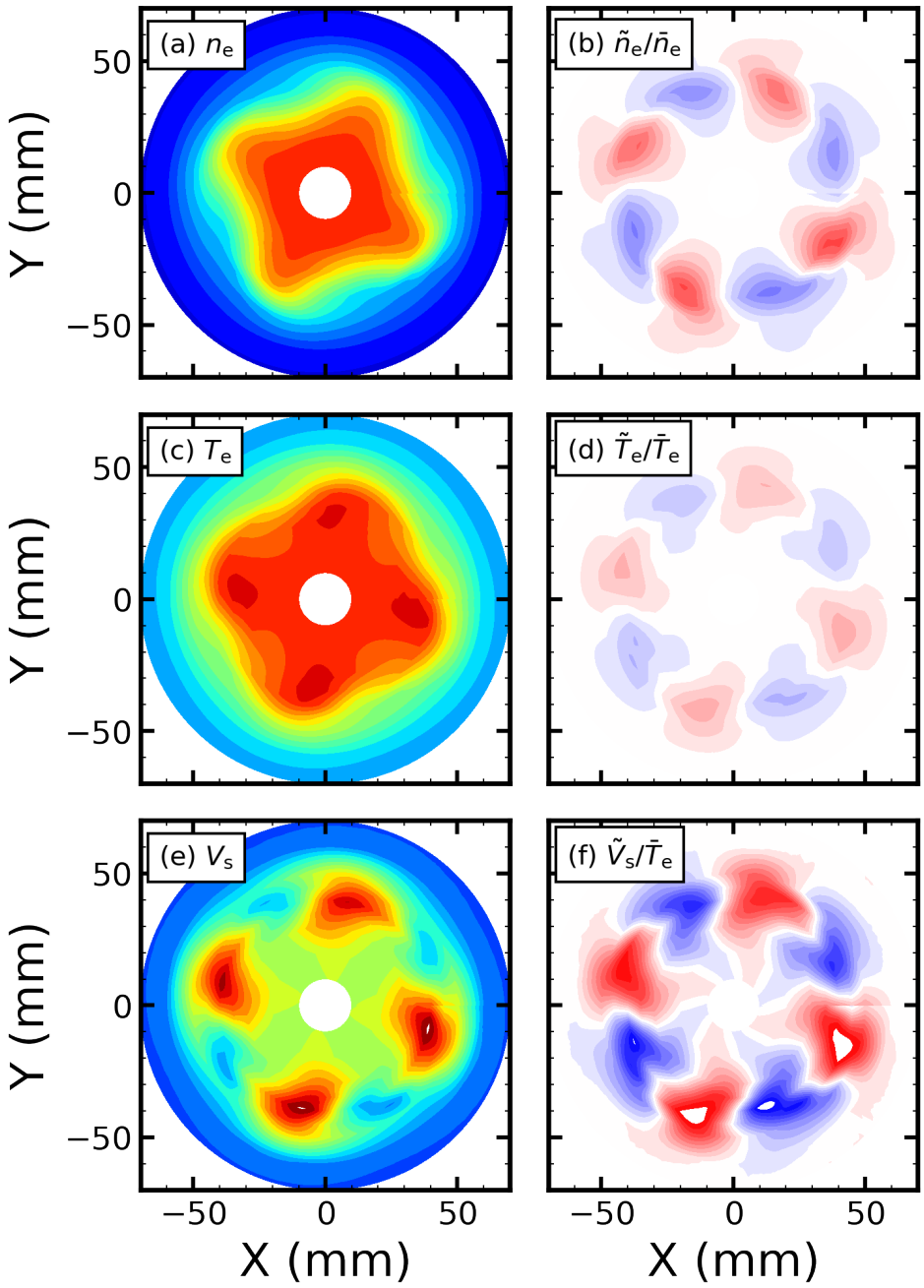

Figure 4.12: Cross-section images of (a) electron density, (c) electron temperature, and (e) plasma potential for the $m = 4$ mode. Those of their normalized fluctuations are shown in (b), (d), and (f).

At r = 40 mm, the phase difference between density and temperature fluctuations (δ_{n_e,T_e}) is - 0.41 rad, and the phase difference between density and potential fluctuations δ_{n_e,V_s} is about - 0.57 rad. The phase differences were evaluated from the conditional sampled spatiotemporal structure. The phase difference can be helpful to information for identifying the instability. In addition, if finite phase differences between density and potential, and between temperature and potential exist, fluctuation can cause particle and heat transport. The results of the fluctuation-driven transport analysis are presented in Sec. 4.1.3.

Conditional sampling was also applied for reconstructing the $m = 1$ mode patterns. Figures 4.13 (a)-(f) show radial-temporal structures of the $m = 1$ mode. Not only the $m = 1$ mode but also the $m = 4$ mode component are extracted. When the $m = 4$ mode is not synchronized with the $m = 1$ mode, the $m = 4$ component should disappear. These results indicate $m = 1$ is nonlinearly coupled with the $m = 4$ mode. Indeed, the bicoherence between the $m = 1$ and $m = 4$ mode is strong as shown in Figure 4.11.

For more clear understanding, low-pass-filtered (< 9 kHz) patterns are shown in Figures 4.14. It can be seen that the spatiotemporal patterns are different for density fluctuation, temperature fluctuation, and potential fluctuation. Assuming the $m = 1$ fluctuations rotate in the electron diamagnetic direction as rigid-body and has $m = 1$ structure. The patterns of density fluctuation is similar to solitary wave pattern observed in LMD-U [28]. Radial wavenumber of density fluctuation are about 30 m^{-1}. Temperature fluctuation and potential fluctuation have more complex patterns than density fluctuation. The radial wave number of temperature and potential is larger than that of the density fluctuation. Since the patterns of the $m = 1$ are different for density, temperature, and potential fluctuation, their phase dif-

ference is finite and different at each radii. These phase differences can cause the fluctuation-driven transport.

The radial profiles of normalized amplitudes for the $m = 1$ mode are evaluated by root mean square value as shown in Figure 4.16. The amplitude of the density is peaked at r = 30 mm and its peak value is about 4 %. Density fluctuation is radially spread, and the full width at half maximum of the density fluctuation is about 30 mm. The amplitude of temperature is peaked at r = 50 mm and its peak value is about 2%. The peaks of the amplitude of potential fluctuation is ambiguous, but the amplitude of the potential fluctuation is 6-8 %. The shapes of eigenfunction are different for density, temperature.

4.1.3 Particle and heat transport driven by the fluctuations

In the previous subsection, it is shown that there are finite phase differences between density fluctuation, temperature fluctuation and potential fluctuation. Finite phase differences cause the turbulent transport as shown in Eq. (3.3). Net fluctuation-driven particle flux is written as Eq. (3.2). In the same way, fluctuation-driven heat flux $\overline{Q_r}$is written as

$$\overline{Q_r} = \overline{nTv_r} = T_0\overline{\Gamma_r} + n_0\overline{\tilde{T}\tilde{v}_r} = \overline{Q_{conv,r}} + \overline{Q_{cond,r}}, \tag{4.1}$$

where T_0 and n_0 are background temperature and density, respectively. $\overline{Q_{conv,r}} = T_0\overline{\Gamma_r}$ represents convective heat flux and $\overline{Q_{cond,r}} = n_0\overline{\tilde{T}\tilde{v}_r}$ represents conductive heat flux.

In transport analysis based on conditional sampling, instantaneous particle and heat transport is evaluated from the time evolution of the fluctuation obtained by conditional sampling. The time average of the instantaneous transports is then evaluated as the net transport as described in

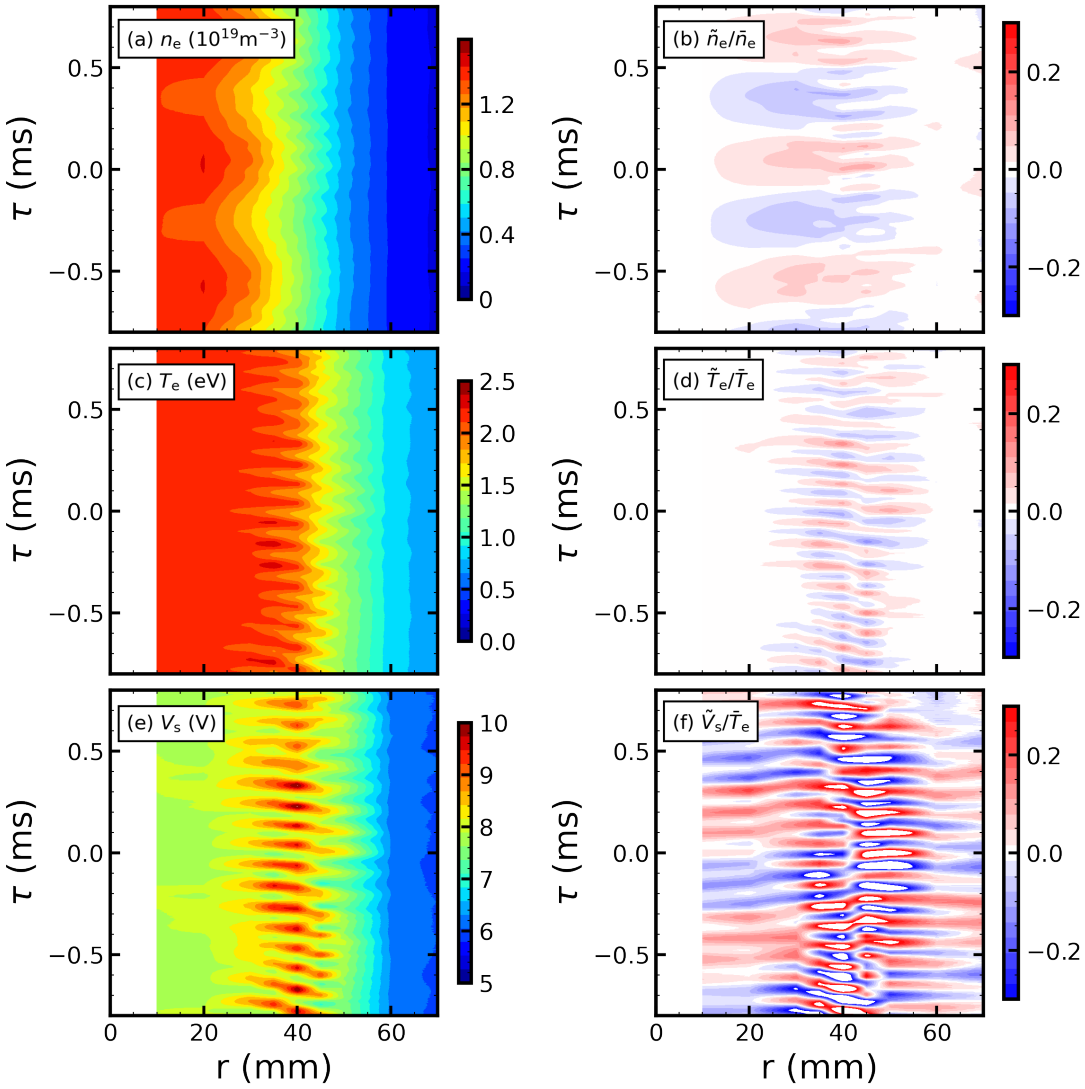

Figure 4.13: Spatiotemporal dynamics of (a) electron density, (c) electron temperature, and (e) plasma potential for the $m = 1$ mode. Those of their normalized fluctuations are shown in (b), (d), and (f). It is visible that higher frequency components are synchronized with $m = 1$ mode

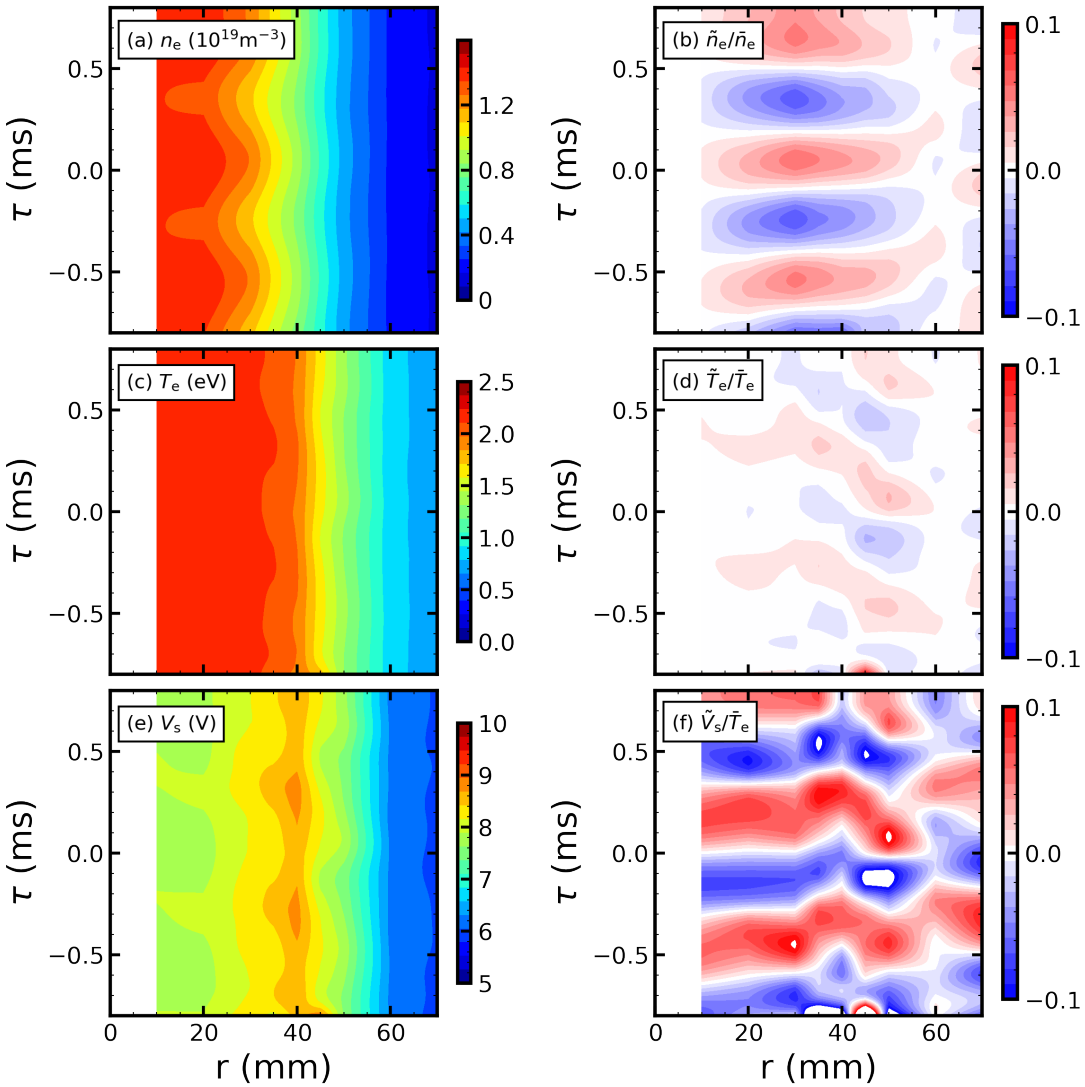

Figure 4.14: Low-pass-filtered spatiotemporal dynamics of (a) electron density, (c) electron temperature, and (e) plasma potential for the $m = 1$ mode. Those of their normalized fluctuations are shown in (b), (d), and (f).

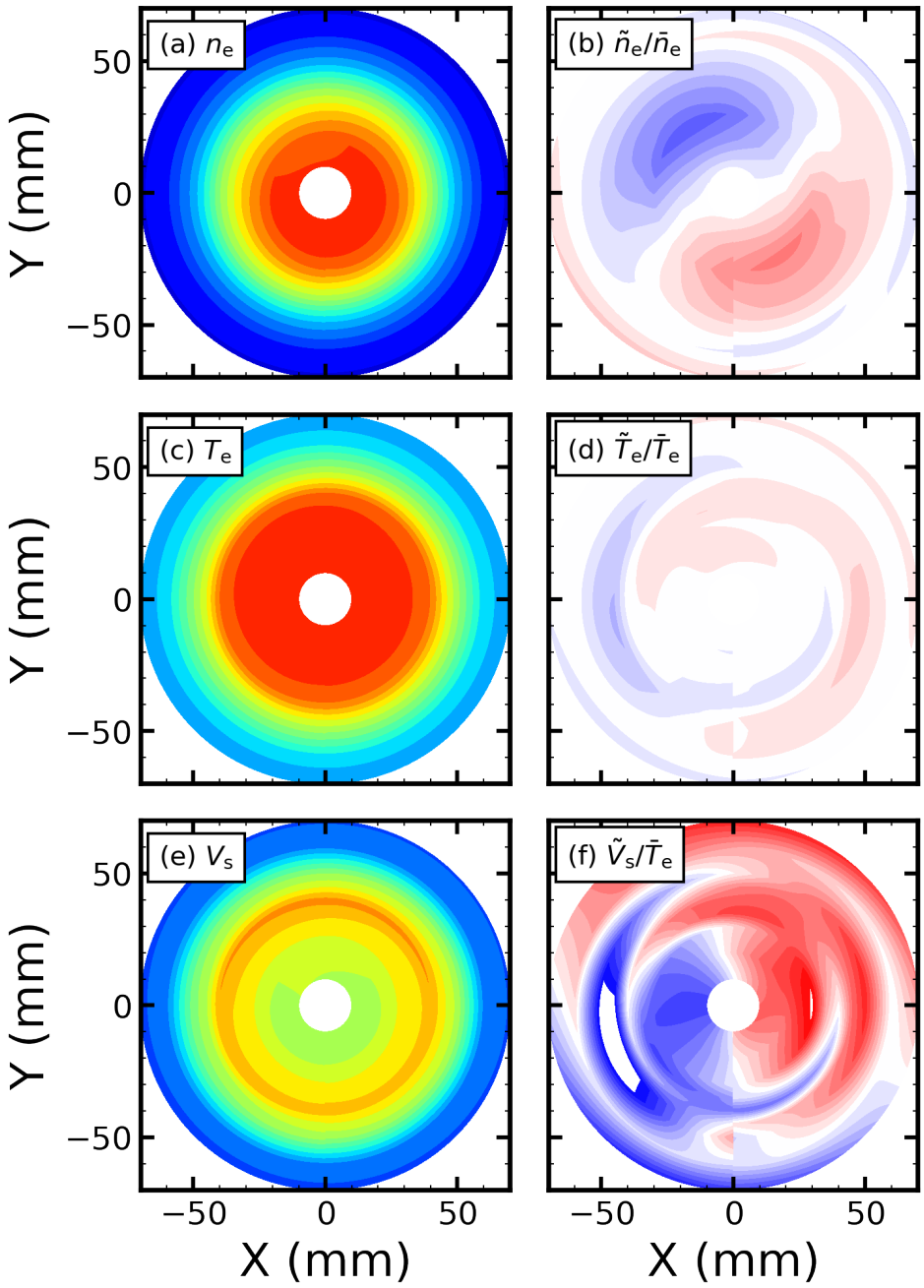

Figure 4.15: Cross-section images of (a) electron density, (c) electron temperature, and (e) plasma potential for the $m = 1$ mode. Those of their normalized fluctuations are shown in (b), (d), and (f).

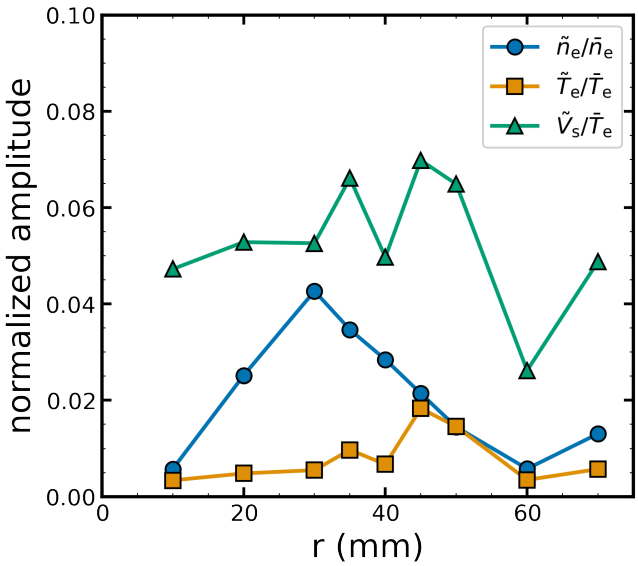

Figure 4.16: Radial profiles of the normalized amplitudes of the $m = 1$ mode.

Sec.3.1.4. The instantaneous particle flux is written in Eq. (3.4) and the instantaneous convective heat flux is evaluated from the instantaneous particle flux. The instantaneous conductive heat flux is written as

$$Q_{cond,r}(t) = -\frac{1}{B} n_0 \left\langle \tilde{T} \right\rangle_{CS} \left\langle \frac{\partial \tilde{\phi}(t)}{\partial t} / \frac{\partial \theta}{\partial t} \right\rangle_{CS} = \frac{k_\theta}{2\pi f B} \left\langle \tilde{T} \right\rangle_{CS} \left\langle \partial_t \tilde{\phi}(t) \right\rangle_{CS}. \quad (4.2)$$

By time-averaging the instantaneous particle/heat flux, the net particle/heat transports are evaluated. Note that the plasma potential was used in the analysis because it was shown that the floating potential is greatly affected by the electron temperature fluctuation.

Figure 4.17 shows profiles of the net fluctuation-driven particle flux. The particle flux driven by the $m = 4$ mode is outward and largest at r = 40 mm. The particle transport driven by the $m = 1$ mode is about 100 times smaller than that of the $m = 4$ mode. The convective and conductive heat flux are shown in figures 4.18 (a) and (b). Each heat transport has a similar shape to the particle flux profile, that is, the $m = 4$ mode drive outward heat flux and peaks around r = 40 mm. The $m = 1$ mode driven heat transport is also 100

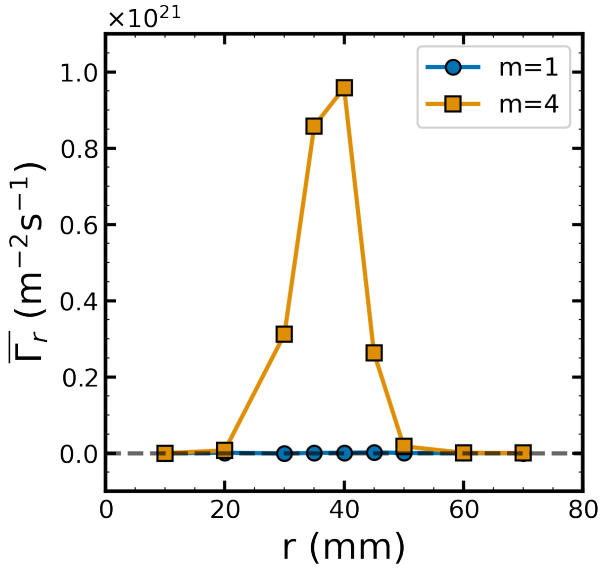

Figure 4.17: Radial profile of net cross-field particle flux obtained by conditional sampling.

times smaller than the $m = 4$ mode driven heat transport. The convective heat transports are 100 times larger than the conductive heat transport.

4.1.4 Origins of the fluctuations

Here, the origins of the $m = 1$ mode and the $m = 4$ mode are discussed based on the obtained spatiotemporal dynamics. The characteristics of the $m = 4$ mode is summarized bellow. The apparent azimuthal speed of the $m = 4$ mode is 600 m/s, which is close to the electron diamagnetic velocity of $\sim$ 750 m/s. The $m = 4$ mode is strongly excited and localized around r = 40 mm where density gradient scale length is shortest. The normalized amplitude of the density fluctuation is the same order of magnitude with that of the potential fluctuation. The ratio of the normalized fluctuation levels is $\frac{\tilde{T}_e}{\bar{T}_e}/\frac{\tilde{n}_e}{\bar{n}_e} \sim 0.3$, which is the same order of magnitude with the theoretically predicted values of $\frac{\tilde{T}_e}{\bar{T}_e}/\frac{\tilde{n}_e}{\bar{n}_e}\frac{\omega_* \eta_e}{k_\parallel^2 \chi_\parallel} \sim 0.3$. The particle and heat transports are outward and localized around r = 40 mm. For more information, axial

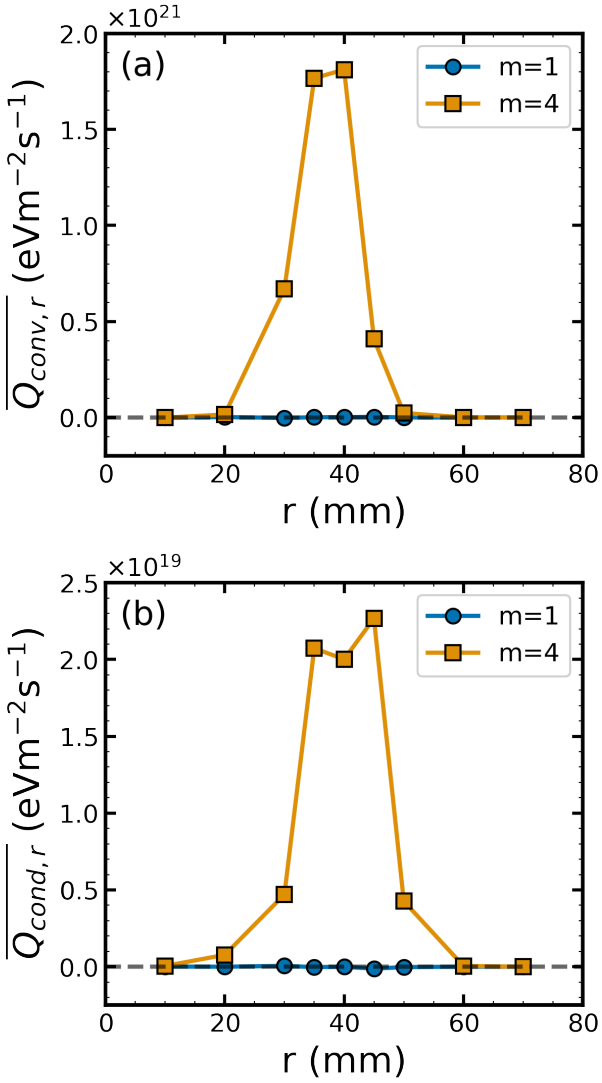

Figure 4.18: Radial profiles of (a) convective component and (b) conductive component, of net cross-field heat flux obtained by conditional sampling.

wavenumber is calculated as shown in Figure 4.19. The axial mode number of the $m = 4$ is finite ($n = k_{\parallel}L \sim$1-2). These results are in good agreement with the characteristics of drift waves, therefore the $m = 4$ mode is considered to be a drift wave.

The characteristics of the $m = 1$ mode are summarized below. The phase velocity is estimated to be 400 m/s. The radial structure of the $m = 1$ mode is broad and peaked at the inner compared with that of the $m = 4$ mode. The fluctuation patterns are different for density, temperature, and potential. The phase differences of them are large. The particle/heat transport is much smaller than the $m = 4$ mode. The axial mode number is $n \sim 0$, which means that the $m = 1$ mode has an axially symmetric structure. Such axially symmetric fluctuations with finite azimuthal wavenumber can be linearly excited by the Kelvin-Helmholtz instability [14,108–110], or nonlinearly excited convection cells [111,112]. To identify specific instability, precise measurements of flow shear or space potential are necessary. Hereafter, based on the above results, the $m = 4$ is referred to as the drift wave (DW), and the $m = 1$ mode is referred to as the axially symmetric (AS) mode.

4.2 Discovery of intermittent nonlinear dynamics

This section presents the experimental discovery of dynamic interaction between the drift wave and the axially symmetric mode. Intermittent competition between them was observed by the instantaneous wavenumber spectrum analysis. The spatiotemporal dynamics of the intermittent competition were evaluated by conditional sampling. Moreover, the nonlinear dynamics during the intermittent competition were also discovered by combining nonlinear energy transfer analysis and conditional sampling. The

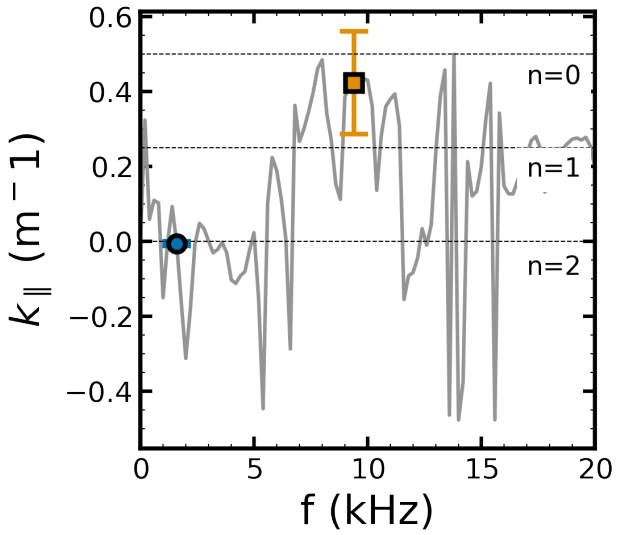

Figure 4.19: Axial wave number (a gray line) evaluated by cross-phase analysis. A orange dot and a green square indicate the $m = 1$ mode of f = 1.6 kHz and the $m = 4$ mode of f = 9.4 kHz, respectively. The error bars are evaluated from the standard deviation of the ensembles.

intermittent competition synchronizes with the $m = 0$ potential fluctuation. Possible explanation of this phenomenon is also discussed.

4.2.1 Intermittent competition of the fluctuations

Since the DW and AS mode have different azimuthal mode number, time evolution of fluctuation power can be trace from instantaneous azimuthal mode power spectrum. Here the Fourier decomposition is applied only in the azimuthal wave number domain and instantaneous time evolution of the wave number spectrum is obtained as shown in Fig. 4.20 (a). The mode power of the DW ($m = 4$) and the AS mode ($m = 1$) are modulated in time. It is obvious that the AS mode quasi-periodically burst. Figure 4.20 (b) displays the time evolution of the mode power of the AS mode and DW. It demonstrates that the AS mode are mutually exclusive with the DW during the intermittent burst (as the power of the AS mode increases, the power of the

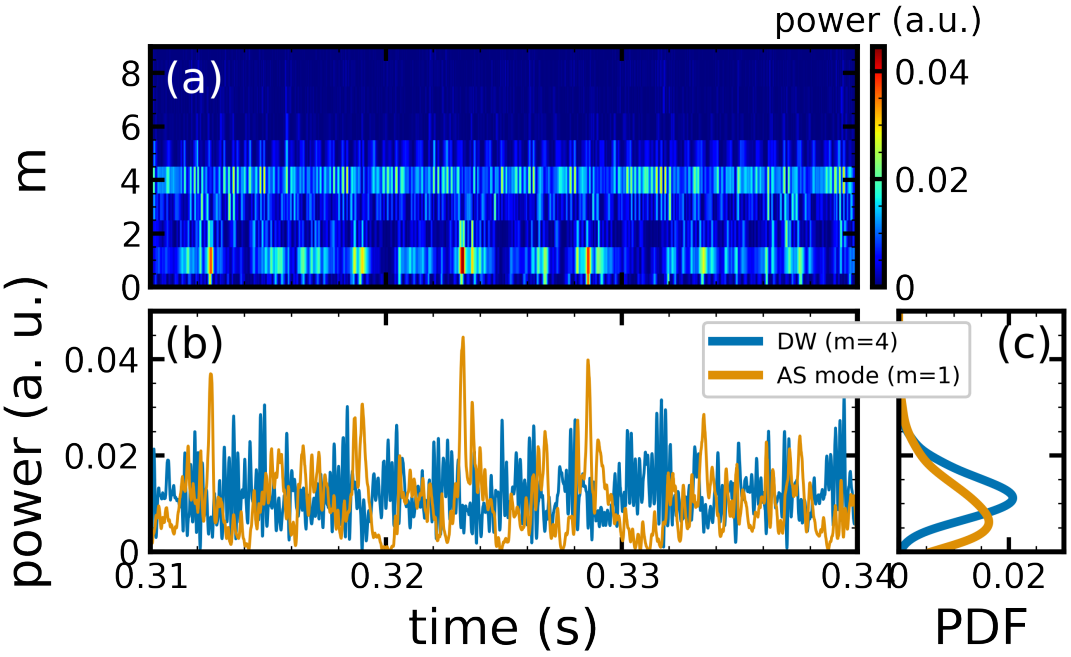

Figure 4.20: (a) Temporal evolution of instantaneous mode power. Instantaneous mode power of the $m = 1$ (the AS mode) and $m = 4$ (the DW) are displayed in (b). (c) Probability density function of the mode's power. Orange and blue lines in (b) and (c) represent the AS mode and the DW, respectively.

DW decreases). The probability density function (PDF) of the AS mode has a positive tail (skewness of 1.26) as shown in Fig. 4.20 (c), that is, the AS mode burst is intermittent.

The modulation spectrum of the instantaneous power spectrum are shown in figure 4.21. The modulation in the AS mode has a frequency of around 300 Hz, which is almost identical to the frequency of the $m = 0$ potential fluctuation while that of the DW has frequencies of about 300 Hz and 1.6 kHz. The 300 Hz component also corresponds to the period of intermittent burst of the AS mode. While the 1.6 kHz component of the modulation spectrum corresponds to the modulation of the DW by the AS mode. The amplitude modulation are also indicated by the bicoherence analysis as shown in fig. 4.22.

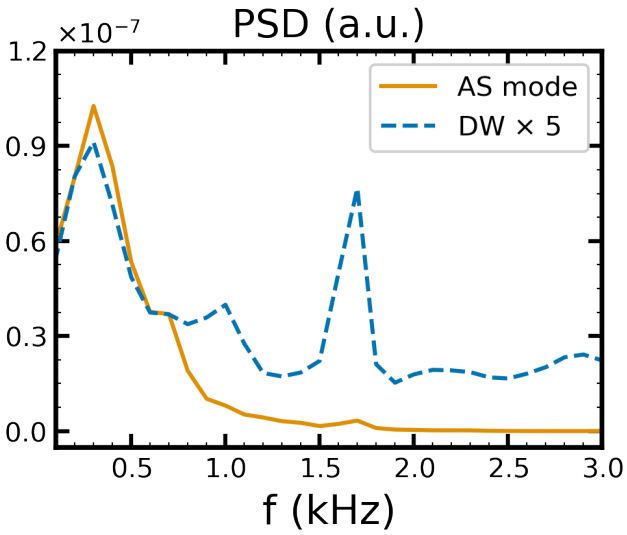

Figure 4.21: Power spectrum density of modulation of the instantaneous mode power. Blue dashed line and orange solid line indicate the drift wave and the AS mode, respectively.

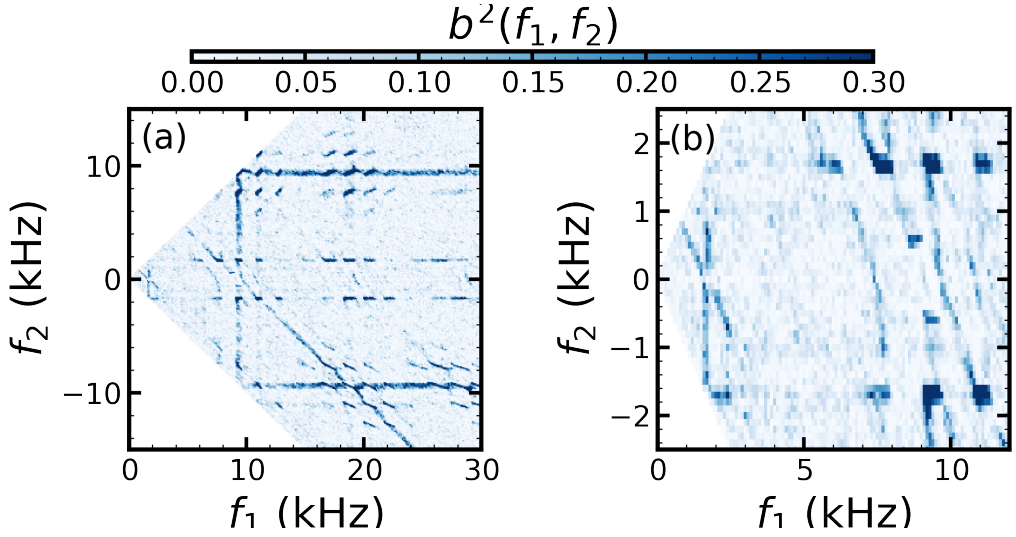

Figure 4.22: (a) Squared bicoherence of the normalized ion saturation current and (b) an enlarged view of the low-frequency region of squared bicoherence.

Focusing on the dynamic interaction during the intermittent burst of the AS mode, since the AS mode and the DW have different frequency, the spatiotemporal behavior during the intermittent burst can be extracted by envelope analysis. After applying band-pass filter to the $\tilde{I}_{\rm is}/\tilde{I}_{\rm is}$ signal obtained by radial movable probe, the envelopes are calculated by the Hilbert transform. Radial movable probe was scanned in a shot-by-shot manner. Applying conditional averaging, spatiotemporal structures of fluctuation component of the envelope ($\tilde{E}$) of the AS mode and the DW are reconstructed and shown in Figures 4.23 (a) and (b). The instantaneous mode power of the AS mode was used as the reference signal for the conditional averaging, and the intermittent burst were detected using the template method. The reference waveform of the instantaneous mode power obtained by conditional averaging is shown in Figure4.24(a). Cross-correlation between the instantaneous mode power and the reference waveform is used for the phase reference of the conditional sampling. We note that low-pass-filter ($f < 1\,$kHz) is applied to the envelope fluctuation obtained by Hilbert transform in order to cut the influence of the carrier wave (1.6 kHz). The envelope of the AS mode increase at r = 20-50 mm while that of the DW decrease at the r = 30-40 mm. The decrease in power of the DW is slightly delayed than the rise in power of the AS mode, and the time lag is $\sim 0.2\,$ms. The power of the AS mode increases at most by a factor of two and then breaks down while that of the DW decreases by about 30 %.

4.2.2 Changes of nonlinear dynamics during the intermittent competition

In order to clarify the nonlinear dynamics in the intermittent burst, conditional sampling and bicoherence analysis are combined. Since the time

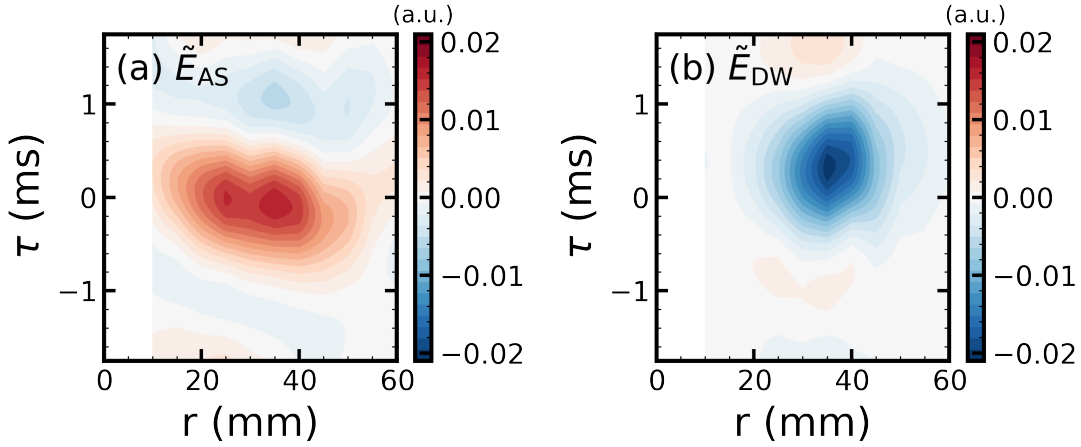

Figure 4.23: (a) Temporal evolution of envelope fluctuations of (a) the AS mode and (b) the DW.

scale of the burst is the same order of the period of the AS mode, wave number bicoherence is more suitable than frequency bicoherence [25]. The summed bicoherence for m is defined as

$$\sum b_m^2 = \frac{1}{s} \sum_{m=m_1+m_2} b^2(m_1, m_2), \tag{4.3}$$

each s is the number of summand for each segment. The summed bicoherence could be an indicator for total contribution to nonlinear coupling. For simplicity, the intermittent burst event is separated into four phases: (i) quasi-stationary phase before the burst; (ii) the $m = 1$ mode power increasing phase; (iii) the power decreasing phase; and (iv) quasi-stationary phase after the burst, as represented in Figure 4.24 (a). Then, the total bicoherence from conditionally sampled instantaneous mode power is estimated for each phase. Figure 4.24 (b) shows wave number total bicoherence at each phase. The nonlinear coupling of the AS mode ($m = 1$) and its second harmonics ($m = 2$) increase at the phases (ii) and (iii). The nonlinear coupling of the DW mode ($m = 4$) slightly increases as well. Moreover, the daughter modes of the AS mode and DW also increase the nonlinear cou-

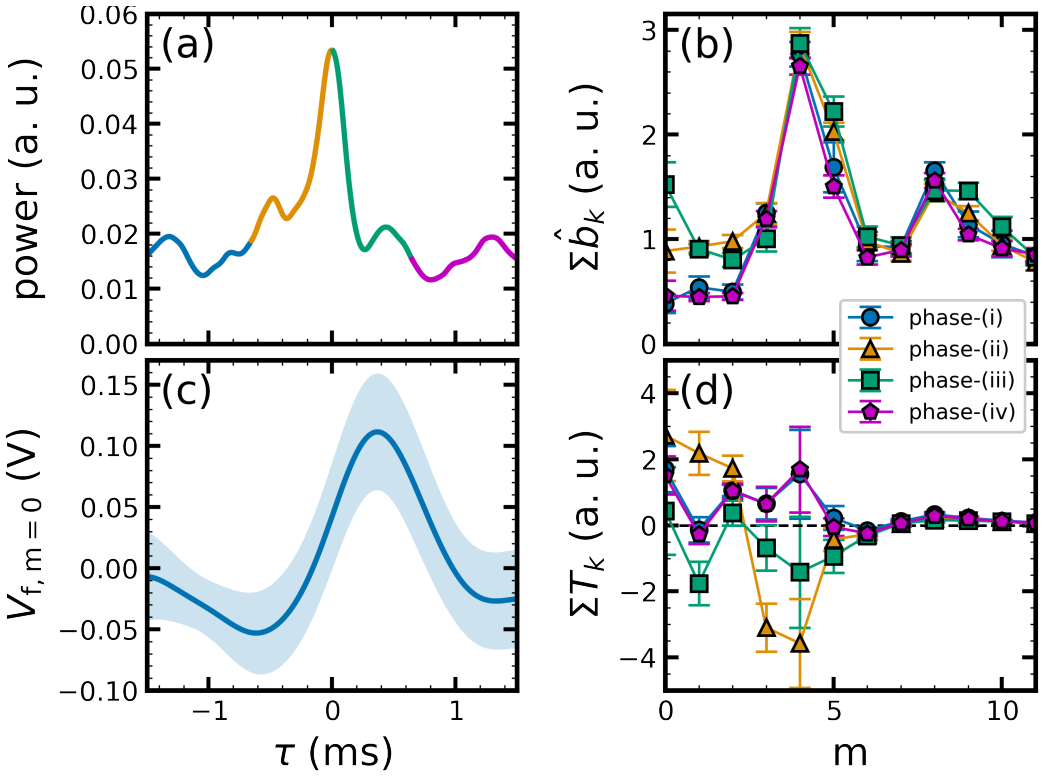

Figure 4.24: (a) Reference waveform of the intermittent burst for conditional sampling, colored for each corresponding phase of the intermittent burst. (c) Time evolution of $m = 0$ component of the conditionally averaged floating potential fluctuation. Filled region of (c) indicates standard deviation. (b) Total bicoherence and (d) energy transfer for each phase which is evaluated from the conditionally sampled instantaneous mode power of $\tilde{I}_{is}/\bar{I}_{is}$.

pling. The $m = 0$ component also increases nonlinear coupling during the burst, and it may be associated with the background change of density or the $m = 0$ potential fluctuation even though the bicoherence is evaluated from the density fluctuation. Figure 4.24 (c) shows the $m = 0$ component of conditionally averaged floating potential fluctuation. It indicates that the $m = 0$ potential fluctuation is synchronizing with the intermittent burst. The amplitude of the $m = 0$ potential is of the same order as observed in LMD-U [27, 28].

Summed bicoherence could give us information for the total strength of

nonlinear coupling, but no information for nonlinear energy transform direction. For further investigation, evaluation of nonlinear energy transfer is necessary. The method of nonlinear energy transfer estimation was developed by Ritz *et al* [86]. Several modified method are also proposed [113,114], and applied to various types of plasma turbulence [115–117]. This method assumes that time evolution of wave number spectrum $X(t,m)$ follows the nonlinear three wave coupling equation written as

$$\frac{\partial}{\partial t}X(t,m) = \Lambda^L_m X(t,m) + \sum_{\substack{m_1 \geq m_2 \\ m=m_1+m_2}} \Lambda^{NL}_{m_1,m_2} X(t,m_1)X(t,m_2), \tag{4.4}$$

where Λ^L_m and $\Lambda^{NL}_{m_1,m_2}$ are the linear and nonlinear coupling coefficients, respectively. Λ^L_m and $\Lambda^{NL}_{m_1,m_2}$ can be estimated from $F(t,m)$ by means of bispectrum analysis [86], or the multiple linear regression [114]. More details of estimation method of the coupling coefficients is reviewed in Appendix.A. In this study, the multiple linear regression was used for estimation of coupling coefficients.

$F(t,m)$ can be evaluated by instantaneous wave number spectrum. By multiplying Eq. (4.4) to $F^*(t,m)$ and taking ensemble average, conservation equation of spectral power $P_m = \langle F(t,m)F^*(t,m)\rangle$ is obtained as

$$\frac{\partial}{\partial t}P_m = \mathfrak{Re}[\Lambda^L_m X(t,m)] + \sum_{\substack{m_1 \geq m_2 \\ m=m_1+m_2}} T_m(m_1,m_2), \tag{4.5}$$

where, $T_m(m_1,m_2)$ is the nonlinear spectral energy transfer function defined as

$$T_m(m_1,m_2) = \mathfrak{Re}[\Lambda^{NL}_{m_1,m_2} \langle X^*_m X_{m_1} X_{m_2}\rangle]. \tag{4.6}$$

Here, the positive values of $T_m(m_1,m_2)$ means the m mode gains energy from the m_1 and m_2 modes, whereas the negative value means losses to the m_1 and m_2 modes. This nonlinear energy transfer analysis is applied to the conditional sampled instantaneous mode power with about 1000 ensembles at

each phase of the intermittent burst as shown in Fig. 4.25(a)-(d). Nonlinear energy transfer are dynamically change during the intermittent competition. Especially, the coupling of $(m_1 = 5, m_2 = -4) \Rightarrow (m_3 = 1)$ and $(m_1 = 5, m_2 = -3) \Rightarrow (m_3 = 2)$ dynamically changed. The $m_3 = 1$ (the AS mode) and $m_3 = 2$ (harmonics of the AS mode) gains energy in the phase (ii). Then, the $m = 1$ mode seems to release energy to $m = 4$ by coupling of $(m_1 = 1, m_2 = 3) \Rightarrow (m_3 = 4)$.

Because plots of energy transfer $T_m(m_1, m_2)$ is not always easy to interpret, for more simple understanding, summed nonlinear energy transfer is calculated as shown in Figure 4.24 (d). The summed nonlinear energy transfer is defined as

$$\sum T_m = \sum_{m=m_1+m_2} T_m(m_1, m_2). \tag{4.7}$$

In the phase (ii), the AS mode gain energy from the other modes, then, the AS mode releases energy in the phase (iii). While the drift wave loses energy during the phases (ii) and (iii) corresponding to the delay of the mode power decrease of the DW. Therefore, the intermittent competition could be related nonlinear energy transfer. It is noted that the $m = 0$ component also gains energy from the other modes which may be related density corrugation due to the intermittent burst or the $m = 0$ potential fluctuation, but further verification is required.

4.2.3 Mechanism of the intermittent competition

The intermittent competition synchronizes with the $m = 0$ low-frequency potential fluctuation. The nonlinear energy transfer dynamically changes during the intermittent competition. The intermittent bursts of nonlinear coupling coefficient of the drift waves were observed in experiment [25].

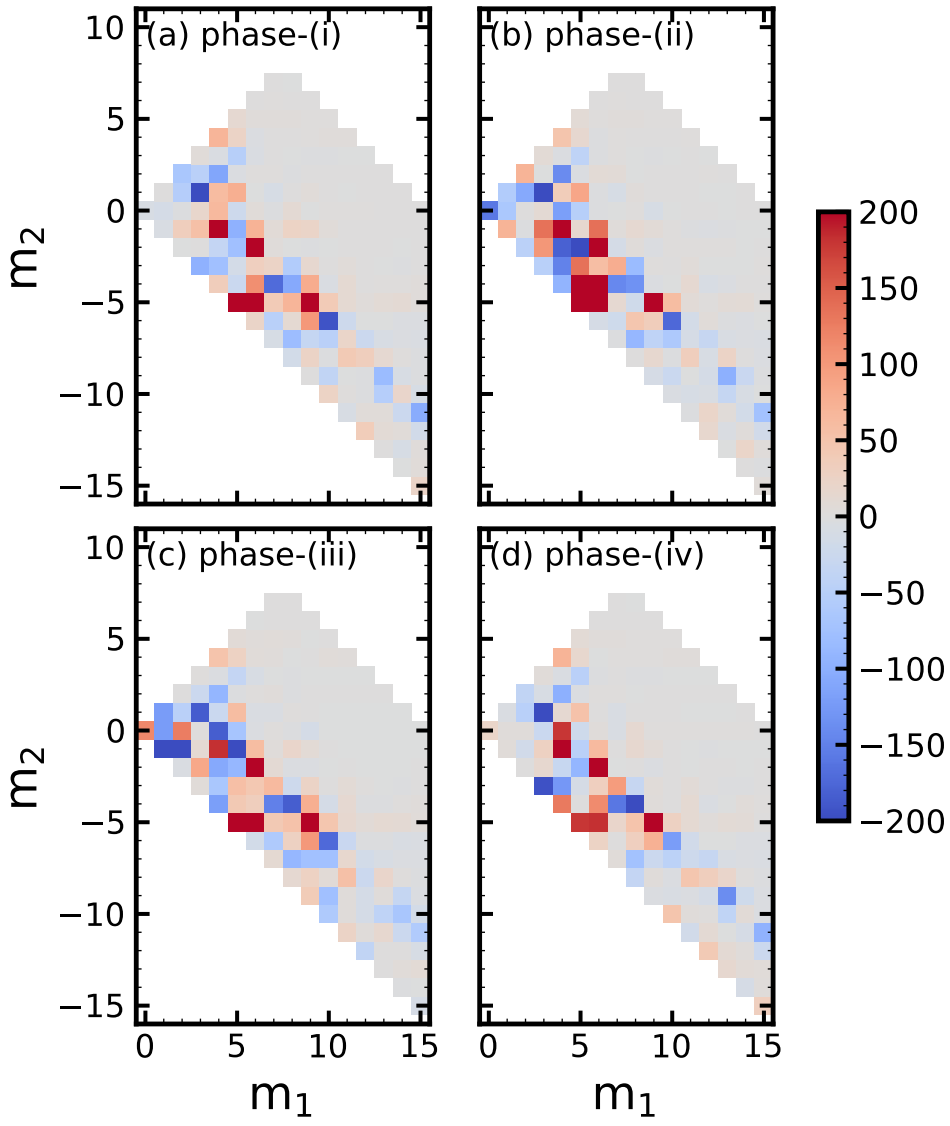

Figure 4.25: Nonlinear energy transfer in the phases (i)-(iv).

Intermittent phenomena associated with Kelvin-Helmholtz type instability were reported in simulation study [118,119]. Dynamic phenomena synchronizing with low-frequency potential fluctuations (zonal flows) are observed in linear plasmas [28, 118, 120], and tokamaks [121].

One of the possible mechanisms of the intermittent competition is discussed below. In this system, the drift waves and the Kelvin-Helmholtz (observed as the AS mode in this study) instability are linearly excited, and zonal flow (the $m = 0$ potential fluctuation) is secondary driven by Reynolds stress due to the drift wave turbulence. Then, the Kelvin-Helmholtz instability is enhanced by zonal flow as tertiary instability. In the enhancement, the Kelvin-Helmholtz instability additionally gains energy from the drift wave turbulence via nonlinear three wave coupling. This kind phenomenon is discussed in theoretical and simulation studies [14, 118]. In order to clarify it, precise flow or radial electric field measurements such as laser induced fluorescence [65] and advanced probe measurements [72, 122] to identify the Kelvin-Helmholtz instability and the zonal flow, are required and left for future work.

Chapter 5

Conclusions

Plasma confinement is determined by anomalous cross-field transport which is driven by turbulence in magnetic fusion plasmas, and thus experimental studies of plasma turbulence are required. Problems to be solved in the measurement of plasma turbulence are the improvement of time resolution and signal-to-noise ratio. In addition, non-stationary analysis of the turbulence is needed. One of the non-stationary analysis that can solve the measurement problem is the conditional sampling method, but this analysis can only be applied to intermittent phenomena. In this thesis, a template method is developed and verified as a new method to solve the problems. The results of this thesis are summarized as follows.

Development of a template method

In order to make the conditional sampling method applicable to arbitrary waveforms, a template method was developed and validated as described in Chapter 3. The template method is an iterative method to detect the appearance time of turbulent fluctuation based on the correlation function between the template waveform and experimental data. The template method can be applied to various turbulence measurements of devices with various shapes, and has the potential to make it possible to observe phenomena that

have been difficult to observe in the past. The specific achievement related to the development of the template method are listed below.

- The template method was compared with the conventional threshold method in detection the turbulent fluctuation. It was found that the template method can detect the emergence period of vibration with higher accuracy than the threshold method. The template method was established as a method that can be applied to arbitrary waveforms with the conditional sampling method.

- The conditional sampling method based the template method was used to evaluate the fluctuation-driven particle transport and compared with the transport evaluation method using Fourier analysis. The particle transport obtained by the template method agreed with that obtained by Fourier analysis. In this validation study, it was shown that the conditional sampling by the template method can correctly analyze the spatiotemporal structure of turbulent fluctuation.

- The time evolution of the instantaneous frequency of the oscillation was observed using the high-precision oscillation appearance time detection by the template method. The observed instantaneous frequency oscillates at 1.7 kHz, which is consistent with the frequency of another oscillation that coexists with the one being analyzed. This is the first experimental observation of the instantaneous frequency of the turbulent fluctuation, which may be related to a new nonlinearity of turbulent oscillation.

Observation of turbulent dynamics by using the template method

Conditional sampling based on the template method were applied to the electrostatic probe measurement and analyze the turbulent dynamics observed in PANTA. Using this analysis, it have been succeeded to improvement of temporal resolution of electron temperature measurement, reconstructed the structure of fluctuations of electron temperature, density, and potential at the same time and position, and found the temporal changes of nonlinear energy transfer between different fluctuations. These observations include phenomena that have been difficult to observe in the past, and will contribute to understanding of the fundamental processes of turbulent fluctuations. The details of the observation results are listed below.

- The conditional sampling method based on the template method was applied to the double probe measurement with low time resolution. As a result, the time resolution of the electron temperature measurement was improved and the electron temperature fluctuation was successfully observed. Moreover, it was found that the electron temperature fluctuation significantly affect the plasma potential measurement.

- Spatiotemporal dynamics of density, temperature and plasma potential fluctuations of the two different modes are reconstructed by using the conditional sampling method. The structures of these fluctuations at the same time and at the same position is successfully identified. These reconstruction allow us to evaluate the particle and heat transport driven by turbulent fluctuations and it is found that the outward particle and convective heat transport.

- Intermittent competition between drift wave and axially symmetric mode was observed by instantaneous wavenumber spectrum analy-

sis. The spatiotemporal dynamics of envelope fluctuations and the dynamic change of nonlinear energy transfer during the intermittent competition are observed. In addition, it was found that the intermittent competition was synchronized with the azimuthally symmetric potential fluctuation. The interaction involving the three types of fluctuations and the dynamics of nonlinear energy transfer, have never been observed experimentally, and are shown for the first time in this study.

The template method developed in this study can be applied not only to diagnostics in basic plasma devices but also to various measurements in fusion devices, which will lead to the observation of new picture of plasma physics. The discovery of the new physical picture of turbulence such as instantaneous frequency modulation and nonlinear energy dynamics, which can be newly observed by this method, will contribute to the clarification of the fundamental process of plasma turbulence.

Acknowledgement

First of all, I would like to express my great appreciation to my supervisor, Professor Shigeru Inagaki, for his continuous supporting. Prof. Inagaki has guide me through various aspects of basic plasma experiment, plasma measurements, suggestions for data analysis methods, and discussions on my study. The results of this research would not have been possible without the guidance and encouragement of him. I will continue to promote my research, keeping his guidance in mind.

I would like to thank Associate Professor Yusuke Kosuge and Assistant Professor Makoto Sasaki, for discussing the experimental study from the theoretical point of view and giving me fruitful comment and many suggestion. I am grateful to Professor Takuma Yamada, Associate Professor Hiroyuki Arakawa, Professor Akihide Fujisawa, Associate Professor Yoshihiko Nagashima, and Assistant Professor Chanho Moon for their useful comments on my research.

Our lab graduates, Assistant Professor Tatsuya Kobayashi and Dr. Fumiyoshi Kin, gave me a lot of support in my research life and always helped me with useful comments in my research. Thank you very much. I'm grateful to my office mates, Mr. Mamoru Matsuo, Mr. Yuya Iwasaki, and Mr. Masaharu Fukuyama. I spent time with them, and we talked about life in the lab and other random things, which always encouraged me.

My parents, Mr. Tsugio and Naomi, supported me in various ways, in-

cluding financially, until I studied in the doctoral course. When I said that I wanted to do research in the doctoral program, they encouraged me without denying it. Thank you very much for everything. Please continue to take care of yourself and stay healthy.

Finally, I would like to thank my wife, Rina. Even though she is busy with her own work, she has given me a great deal of support and encouragement in my daily life. Without her support, I would not have been able to overcome the challenges of my research in the doctoral program.

Appendix A

Estimation of coupling coefficients

Here, the estimation method of the linear/nonlinear coupling coefficients (Λ_m^L and Λ_{m_1,m_2}^{NL}) is reviewed. As mentioned in 4.2.2, the nonlinear energy transfer is estimated on the basis of the three-wave coupling equation (Eq. (4.4)). The mode number spectrum $X(t,m)$ can be written as a complex representation of $X(t,m) = |X(t,m)|e^{i\theta(t,m)}$, where $|X(t,m)|$ and $\theta(t,m)$ represent the instantaneous amplitude and the instantaneous phase, of $X(t,m)$, respectively. Discretizing Eq.(4.4) with spectrum $|X(t,m)|e^{i\theta(t,m)}$ for the time distance δt results in

$$Y_m = \mathcal{L}_m X_m + \sum_{\substack{m_1 \geq m_2 \\ m=m_1+m_2}} \mathcal{N}_m^{m_1,m_2} X_{m_1} X_{m_2} \tag{A.1}$$

where,

$$Y_m = X_m(t+\delta t), \tag{A.2}$$

$$X_m = X_m(t), \tag{A.3}$$

$$\mathcal{L}_m = \Lambda_m^{\mathbf{L}} \delta t + 1 - i[\theta_m(t+\delta t) - \theta_m(t)]e^{ie^{i\delta\theta_m}}, \tag{A.4}$$

$$\mathcal{N}_m^{m_1,m_2} = \Lambda_{m_1,m_2}^{\mathbf{N}} \delta t e^{i\delta\theta_m}, \tag{A.5}$$

$$\delta\theta_m = \theta_m(t+\delta t) - \theta_m(t). \tag{A.6}$$

When the $\mathcal{L}_m$ and $\mathcal{N}_{m_1,m_2}$ are obtained, the coupling coefficients and nonlinear energy transfer function can be evaluated. There are two methods for evaluating the $\mathcal{L}_m$ and $\mathcal{N}_{m_1,m_2}$: the Ritz's method based on Fourier analysis and the Wit's method based on multiple regression technique.

In Ritz's method, assuming the fourth moment of $\left\langle X_{m_1}X_{m_2}X^*_{m_1}X^*_{m_1}\right\rangle$ can be written as $\langle|X_{m_1}X_{m_2}|^2\rangle$ (Millionshchikov hypothesis), the $\mathcal{L}_m$ and $\mathcal{N}_{m_1,m_2}$ are estimated from the moments of $\langle Y_m X^*_m\rangle$ and $\left\langle Y_m X^*_{m_1}X^*_{m_2}\right\rangle$. By multiplying each X^*_m and $X^*_{m_1}X^*_{m_2}$ with Eq.(A.1) and by ensemble averaging over many statistically similar realizations, the moment equations are obtained as

$$\langle Y_m X^*_m\rangle = \mathcal{L}_m \langle X_m X^*_m\rangle + \sum_{\substack{m_1\geq m_2\\ m=m_1+m_2}} \mathcal{N}_m^{m_1,m_2} \langle X_{m_1}X_{m_2}X^*_m\rangle, \tag{A.7}$$

$$\left\langle Y_m X^*_{m'_1}X^*_{m'_2}\right\rangle = \mathcal{L}_m \left\langle X_m X^*_{m'_1}X^*_{m'_2}\right\rangle + \sum_{\substack{m_1\geq m_2\\ m=m_1+m_2}} \mathcal{N}_m^{m_1,m_2} \left\langle X_{m_1}X_{m_2}X^*_{m'_1}X^*_{m'_2}\right\rangle. \tag{A.8}$$

Assuming the terms of $(m'_1 m'_2) \neq (m_1 m_2)$ for the fourth moment of Eq.(A.8) is negligible, the fourth moment is written as

$$\begin{aligned}\sum_{\substack{m_1\geq m_2\\ m=m_1+m_2}} \mathcal{N}_m^{m_1,m_2} \left\langle X_{m_1}X_{m_2}X^*_{m'_1}X^*_{m'_2}\right\rangle &= \mathcal{N}_m^{m_1,m_2} \left\langle X_{m'_1}X_{m'_2}X^*_{m'_1}X^*_{m'_2}\right\rangle \\ &= \mathcal{N}_m^{m_1,m_2} \left\langle |X_{m_1}X_{m_2}|^2\right\rangle \end{aligned} \tag{A.9}$$

Using Eqs. (A.7), (A.8), and (A.9), and eliminating $\mathcal{N}_{m_1,m_2}$, $\mathcal{L}_m$ is obtained as

$$\begin{aligned}
\langle Y_m X_m^* \rangle =& \mathcal{L}_m \langle X_m X_m^* \rangle && \text{(A.10)} \\
&+ \sum_{\substack{m_1 \geq m_2 \\ m=m_1+m_2}} \left(\frac{\langle X_{m_1} X_{m_2} X_m^* \rangle - \mathcal{L}_m \langle X_{m_1} X_{m_2} X_m^* \rangle}{\langle |X_{m_1} X_{m_2}|^2 \rangle} \right) \langle X_{m_1} X_{m_2} X_m^* \rangle && \text{(A.11)} \\
=& \mathcal{L}_m \left(\langle X_m X_m^* \rangle - \sum_{\substack{m_1 \geq m_2 \\ m=m_1+m_2}} \frac{\langle X_{m_1} X_{m_2} X_m^* \rangle}{\langle |X_{m_1} X_{m_2}|^2 \rangle} \right) && \text{(A.12)} \\
&+ \sum_{\substack{m_1 \geq m_2 \\ m=m_1+m_2}} \frac{\langle X_{m_1} X_{m_2} X_m^* \rangle}{\langle |X_{m_1} X_{m_2}|^2 \rangle} && \text{(A.13)} \\
& && \text{(A.14)}
\end{aligned}$$

$$\therefore \mathcal{L}_m = \frac{\langle Y_m X_m^* \rangle - \sum_{\substack{m_1 \geq m_2 \\ m=m_1+m_2}} \frac{\langle X_{m_1} X_{m_2} X_m^* \rangle \langle X_{m_1} X_{m_2} Y_m^* \rangle}{\langle |X_{m_1} X_{m_2}|^2 \rangle}}{\langle X_m X_m^* \rangle - \sum_{\substack{m_1 \geq m_2 \\ m=m_1+m_2}} \frac{|\langle X_{m_1} X_{m_2} X_m^* \rangle|^2}{\langle |X_{m_1} X_{m_2}|^2 \rangle}}. \quad \text{(A.15)}$$

Using $\mathcal{L}_m$, $\mathcal{N}_m^{m_1,m_2}$ is evaluated as,

$$\mathcal{N}_m^{m_1,m_2} = \frac{\langle Y_m X_{m_1}^* X_{m_2}^* \rangle - \mathcal{L}_m \langle X_{m_1} X_{m_2} X_m^* \rangle}{\langle |X_{m_1} X_{m_2}|^2 \rangle}. \quad \text{(A.16)}$$

Here, $\langle X_m X_m^* \rangle$ is calculated auto power spectrum, $\langle Y_m X_m^* \rangle$ is calculated by cross power spectrum, $\langle X_{m_1} X_{m_2} X_m^* \rangle$ is calculated by auto bispectrum, $\langle X_{m_1} X_{m_2} X_m^* \rangle$ is calculated by cross bispectrum, and $\langle X_{m_1} X_{m_2} X_m^* \rangle$ is calculated by second order moment. Namely, in Ritz's method, the linear/nonlinear coupling coefficients are evaluated based on the Fourier spectrum analysis. Further modification of the method was also proposed by Kim et al [113].

In the Wit's method, The following matrix equation are built for each mode number m:

$$\mathsf{Y}_m = \mathsf{X}_m \mathsf{H}_m, \quad \text{(A.17)}$$

where

$$\mathsf{Y}_m = \left[\begin{array}{cccc} Y_m^{(1)} & Y_m^{(2)} & \cdots & Y_m^{(N)} \end{array} \right]^T \tag{A.18}$$

$$\mathsf{H}_m = \left[\begin{array}{cccc} \mathcal{L}_m & \mathcal{N}_m^{0,m} & \mathcal{N}_m^{1,m-1} & \cdots & \mathcal{N}_m^{m_M,m-m_M} \end{array} \right]^T \tag{A.19}$$

$$\mathsf{X}_m = \left[\begin{array}{ccccc} X_m^{(1)} & X_0^{(1)}X_m^{(1)} & X_1^{(1)}X_{m-1}^{(1)} & \cdots & X_{m_M}^{(1)}X_{m-m_M}^{(1)} \\ X_m^{(2)} & X_0^{(2)}X_m^{(2)} & X_1^{(2)}X_{m-1}^{(2)} & \cdots & X_{m_M}^{(2)}X_{m-m_M}^{(2)} \\ \vdots & \vdots & \vdots & \ddots & \vdots \\ X_m^{(N)} & X_0^{(N)}X_m^{(N)} & X_1^{(N)}X_{m-1}^{(N)} & \cdots & X_{m_M}^{(N)}X_{m-m_M}^{(N)} \end{array} \right] \tag{A.20}$$

Here, $X_m^{(n)}$ denotes n-th ensemble of X_m, N is number number of ensembles and m_M is muximum mode. Solving the matrix equation (A.17), the vector H_m, that is the $\mathcal{L}_m$ and $\mathcal{N}_{m_1,m_2}$, is obtained.

Bibliography

[1] J. D. Lawson. SOME CRITERIA FOR A POWER PRODUCING THERMONUCLEAR REACTOR. *Proc. Phys. Soc. (London)*, Vol: B70, January 1957.

[2] https://www.euro-fusion.org.

[3] L.A. Artsimovich, G.A. Brobrovskii, E.P. Gorbunov, D.P. Ivanov, V.D. Kirillov, E.I. Kuznetsov, S.V. Mirnov, M.P Petrov, K.A. Rasumova, V.S Strelkov, and D.A. Shcheglov. Survey on Closed Plasma Systems. *Plasma Physics and Controlled Nuclear Fusion Research, Novosibirsk*, 1(17), 1968.

[4] N. J. Peacock, D. C. Robinson, M. J. Forrest, P. D. Wilcock, and V. V. Sannikov. Measurement of the Electron Temperature by Thomson Scattering in Tokamak T3. *Nature*, 224(5218):488–490, November 1969.

[5] James Glanz. Turbulence May Sink Titanic Reactor. *Science*, 274(5293):1600–1600, December 1996.

[6] F. Wagner. A quarter-century of H-mode studies. *Plasma Physics and Controlled Fusion*, 49(12B):B1–B33, November 2007.

[7] A. Fujisawa, K. Itoh, H. Iguchi, K. Matsuoka, S. Okamura, A. Shimizu, T. Minami, Y. Yoshimura, K. Nagaoka, C. Takahashi, M. Kojima, H. Nakano, S. Ohsima, S. Nishimura, M. Isobe, C. Suzuki, T Akiyama, K. Ida, K. Toi, S.-I. Itoh, and P. H. Diamond. Identification of Zonal Flows in a Toroidal Plasma. *Physical Review Letters*, 93(16):165002, October 2004.

[8] P. H. Diamond, S.-I. Itoh, K. Itoh, and T. S. Hahm. Zonal flows in plasma—a review. *Plasma Physics and Controlled Fusion*, 47(5):R35–R161, April 2005.

[9] M. N. Rosenbluth and F. L. Hinton. Poloidal Flow Driven by Ion-Temperature-Gradient Turbulence in Tokamaks. *Physical Review Letters*, 80(4):724–727, January 1998.

[10] K. Ikeda. Progress in the ITER Physics Basis. *Nuclear Fusion*, 47(6), June 2007.

[11] http://www.iter.org.

[12] W. Horton. Drift waves and transport. *Reviews of Modern Physics*, 71(3):735–778, 1999.

[13] Akira Hasegawa, Carol G. Maclennan, and Yuji Kodama. Nonlinear behavior and turbulence spectra of drift waves and Rossby waves. *The Physics of Fluids*, 22(11):2122–2129, November 1979.

[14] Eun-jin Kim and P. H. Diamond. Dynamics of zonal flow saturation in strong collisionless drift wave turbulence. *Physics of Plasmas*, 9(11):4530–4539, November 2002.

[15] Y. Nagashima, K. Hoshino, A. Ejiri, K. Shinohara, Y. Takase, K. Tsuzuki, K. Uehara, H. Kawashima, H. Ogawa, T. Ido, Y. Kusama, and Y. Miura. Observation of Nonlinear Coupling between Small-Poloidal Wave-Number Potential Fluctuations and Turbulent Potential Fluctuations in Ohmically Heated Plasmas in the JFT-2M Tokamak. *Physical Review Letters*, 95(9):095002, August 2005.

[16] P. Manz, M. Ramisch, and U. Stroth. Physical mechanism behind zonal-flow generation in drift-wave turbulence. *Physical Review Letters*, 103(16):1–4, 2009.

[17] J. F. Drake, P. N. Guzdar, and A. B. Hassam. Streamer Formation in Plasma with a Temperature Gradient. *Physical Review Letters*, 61(19):2205–2208, November 1988.

[18] W. Dorland, F. Jenko, M. Kotschenreuther, and B. N. Rogers. Electron Temperature Gradient Turbulence. *Physical Review Letters*, 85(26):5579–5582, December 2000.

[19] Takuma Yamada, Sanae I. Itoh, Takashi Maruta, Naohiro Kasuya, Yoshihiko Nagashima, Shunjiro Shinohara, Kenichiro Terasaka, Masatoshi Yagi, Shigeru Inagaki, Yoshinobu Kawai, Akihide Fujisawa, and Kimitaka Itoh. Anatomy of plasma turbulence. *Nature Physics*, 4(9):721–725, 2008.

[20] T. Yamada, S.-I. Itoh, S. Inagaki, Y. Nagashima, N. Kasuya, K. Kamataki, H. Arakawa, T. Kobayashi, M. Yagi, A. Fujisawa, and K. Itoh. Observation of Quasi-Two-Dimensional Nonlinear Interactions in a Drift-Wave Streamer. *Physical Review Letters*, 105(22):225002, November 2010.

[21] F. Kin, A. Fujisawa, K. Itoh, Y. Kosuga, M. Sasaki, S. Inagaki, Y. Nagashima, T. Yamada, N. Kasuya, K. Yamasaki, K. Hasamada, B. Y. Zhang, Y. Kawachi, H. Arakawa, T. Kobayashi, and S.-I. Itoh. Observations of radially elongated particle flux induced by streamer in a linear magnetized plasma. *Physics of Plasmas*, 26(4):042306, April 2019.

[22] E. Mazzucato, T. Munsat, H. Park, B. H. Deng, C. W. Domier, N. C. Luhmann, A. J. H. Donné, and M. J. van de Pol. Fluctuation measurements in tokamaks with microwave imaging reflectometry. *Physics of Plasmas*, 9(5):1955–1961, May 2002.

[23] A. V. Melnikov, L. I. Krupnik, L. G. Eliseev, J. M. Barcala, A. Bravo, A. A. Chmyga, G. N. Deshko, M. A. Drabinskij, C. Hidalgo, P. O. Khabanov, S. M. Khrebtov, N. K. Kharchev, A. D. Komarov, A. S. Kozachek, J. Lopez, S. E. Lysenko, G. Martin, A. Molinero, J. L. de Pablos, A. Soleto, M. V. Ufimtsev, V. N. Zenin, A. I. Zhezhera, and and. Heavy ion beam probing—diagnostics to study potential and turbulence in toroidal plasmas. *Nuclear Fusion*, 57(7):072004, March 2017.

[24] L. Schmitz, L. Zeng, T. L. Rhodes, J. C. Hillesheim, E. J. Doyle, R. J. Groebner, W. A. Peebles, K. H. Burrell, and G. Wang. Role of Zonal Flow Predator-Prey Oscillations in Triggering the Transition to H-Mode Confinement. *Physical Review Letters*, 108(15):155002, April 2012.

[25] F. Brochard, T. Windisch, O. Grulke, and T. Klinger. Experimental evidence of mode coupling in drift wave intermittent turbulence using a wave number bicoherence analysis. *Physics of Plasmas*, 13(12):122305, December 2006.

[26] Chanho Moon, Toshiro Kaneko, and Rikizo Hatakeyama. Dynamics of Nonlinear Coupling between Electron-Temperature-Gradient Mode and Drift-Wave Mode in Linear Magnetized Plasmas. *Physical Review Letters*, 111(11):115001, September 2013.

[27] Yoshihiko Nagashima, Sanae I. Itoh, Shunjiro Shinohara, Masayuki Fukao, Akihide Fujisawa, Kenichiro Terasaka, Yoshinobu Kawai, George R. Tynan, Patrick H. Diamond, Masatoshi Yagi, Shigeru Inagaki, Takuma Yamada, and Kimitaka Itoh. Observation of the parametric-modulational instability between the drift-wave fluctuation and azimuthally symmetric sheared radial electric field oscillation in a cylindrical laboratory plasma. *Physics of Plasmas*, 16(2):20706, 2009.

[28] H. Arakawa, S. Inagaki, M. Sasaki, Y. Kosuga, T. Kobayashi, N. Kasuya, Y. Nagashima, T. Yamada, M. Lesur, A. Fujisawa, K. Itoh, and S.-I. Itoh. Eddy, drift wave and zonal flow dynamics in a linear magnetized plasma. *Scientific Reports*, 6(1):33371, September 2016.

[29] A. E. Costley, R. J. Hastie, J. W. M. Paul, and J. Chamberlain. Electron Cyclotron Emission from a Tokamak Plasma: Experiment and Theory. *Physical Review Letters*, 33(13):758–761, September 1974.

[30] H. M. Mott-Smith and Irving Langmuir. The Theory of Collectors in Gaseous Discharges. *Physical Review*, 28(4):727–763, October 1926.

[31] Robert B. Lobbia and Alec D. Gallimore. Temporal limits of a rapidly swept Langmuir probe. *Physics of Plasmas*, 17(7):073502, July 2010.

[32] Shinji Kobayashi, Akira Sakasai, Yoshihiko Koide, Yoshiteru Sakamoto, Yutaka Kamada, Takaki Hatae, Naoyuki Oyama, and Yukitoshi Miura. Development of Fast Charge Exchange Recombination Spectroscopy by Using Interference Filter Method in JT-60U. □□□□□□□□□□□, 79(10):1043–1050, 2003.

[33] Lyman Spitzer. Particle Diffusion across a Magnetic Field. *The Physics of Fluids*, 3(4):659–661, July 1960.

[34] R. J. Hawryluk. AN EMPIRICAL APPROACH TO TOKAMAK TRANSPORT. In B. Coppi, G. G. Leotta, D. Pfirsch, R. Pozzoli, and E. Sindoni, editors, *Physics of Plasmas Close to Thermonuclear Conditions*, pages 19–46. Pergamon, January 1981.

[35] J. B. Taylor and B. McNamara. Plasma Diffusion in Two Dimensions. *The Physics of Fluids*, 14(7):1492–1499, July 1971.

[36] C. C. Petty, T. C. Luce, K. H. Burrell, S. C. Chiu, J. S. deGrassie, C. B. Forest, P. Gohil, C. M. Greenfield, R. J. Groebner, R. W. Harvey, R. I. Pinsker, R. Prater, R. E. Waltz, R. A. James, and D. Wròblewski. Nondimensional transport scaling in DIII-D: Bohm versus gyro-Bohm resolved. *Physics of Plasmas*, 2(6):2342–2348, June 1995.

[37] S. Oldenbürger, S. Inagaki, T. Kobayashi, H. Arakawa, N. Ohyama, K. Kawashima, Y. Tobimatsu, A. Fujisawa, K. Itoh, and S.-I. Itoh. Dynamics of particle flux in a cylindrical magnetized plasma. *Plasma Physics and Controlled Fusion*, 54(5):055002, April 2012.

[38] S. Inagaki, T. Kobayashi, Y. Kosuga, S.-I. Itoh, T. Mitsuzono, Y. Nagashima, H. Arakawa, T. Yamada, Y. Miwa, N. Kasuya, M. Sasaki, M. Lesur, A. Fujisawa, and K. Itoh. A Concept of Cross-Ferroic Plasma Turbulence. *Scientific Reports*, 6(1):22189, February 2016.

[39] A. V. Melnikov, L. G. Eliseev, E. Ascasibar, A. A. Chmyga, C. Hidalgo, T. Ido, R. Jiménez-Gómez, A. D. Komarov, A. S. Kozachek, L. I. Krupnik, S. M. Khrebtov, A. Könies, Yu K. Kuznetsov, A. López-Fraguas, S. E. Lysenko, V. A. Mavrin, K. Nagaoka, J. L. de Pablos, M. A. Pedrosa, S. V. Perfilov, A. I. Smolyakov, D. A. Spong, M. V. Ufimtsev, and S. Yamamoto and. Alfvén eigenmode properties and dynamics in the TJ-II stellarator. *Nuclear Fusion*, 52(12):123004, November 2012.

[40] Leonid G. Eliseev, Alexander V. Melnikov, Sergey E. Lysenko, Philipp O. Khabanov, Vitaly N. Zenin, Mikhail A. Drabinskij, Nikolaj K. Kharchev, Alexander S. Kozachek, Ludmila I. Krupnik, and Hibp

Team. Evaluation of Turbulent Particle Flux by Heavy Ion Beam Probe in the T-10 Tokamak. *Plasma and Fusion Research*, 13:3402106–3402106, 2018.

[41] A. Le, V. Roytershteyn, H. Karimabadi, A. Stanier, L. Chacon, and K. Schneider. Wavelet methods for studying the onset of strong plasma turbulence. *Physics of Plasmas*, 25(12):122310, December 2018.

[42] B. Ph. van Milligen, C. Hidalgo, and E. Sánchez. Nonlinear Phenomena and Intermittency in Plasma Turbulence. *Physical Review Letters*, 74(3):395–398, January 1995.

[43] Tatsuya Kobayashi, Shigeru Inagaki, Hiroyuki Arakawa, Stella Oldenbürger, Makoto Sasaki, Yoshihiko Nagashima, Takuma Yamada, Satoru Sugita, Masatoshi Yagi, Naohiro Kasuya, Akihide Fujisawa, Sanae-I. Itoh, and Kimitaka Itoh. Observation of Nonlinear Coupling between Low Frequency Coherent Modes and Background Turbulence in LMD-U. *Plasma and Fusion Research*, 6:2401082–2401082, 2011.

[44] R Antonia. Conditional Sampling in Turbulence Measurement. *Annual Review of Fluid Mechanics*, 13:131–156, 1981.

[45] Y. M. Yuan and M. R. Mokhtarzadeh-Dehghan. A comparison study of conditional-sampling methods used to detect coherent structures in turbulent boundary layers. *Physics of Fluids*, 6(6):2038–2057, June 1994.

[46] R. A. Moyer, T. E. Evans, T. H. Osborne, P. R. Thomas, M. Becoulet, J. Harris, K.-H. Finken, J. A. Boedo, E. J. Doyle, M. E. Fenstermacher, P. Gohil, R. J. Groebner, M. Groth, G. L. Jackson, R. J. La Haye, C. J. Lasnier, A. W. Leonard, G. R. McKee, H. Reimerdes, T. L. Rhodes, D. L. Rudakov, M. J. Schaffer, P. B. Snyder, M. R. Wade, G. Wang, J. G. Watkins, W. P. West, and L. Zeng. Edge localized mode control with an edge resonant magnetic perturbation. *Physics of Plasmas*, 12(5):056119, May 2005.

[47] I. Furno, B. Labit, M. Podestà, A. Fasoli, S. H. Müller, F. M. Poli, P. Ricci, C. Theiler, S. Brunner, A. Diallo, and J. Graves. Experimental observation of the blob-generation mechanism from interchange waves in a plasma. *Physical Review Letters*, 100(5):55004, 2008.

[48] C. Theiler, A. Diallo, A. Fasoli, I. Furno, B. Labit, M. Podestà, F. M. Poli, and P. Ricci. The role of the density gradient on intermittent cross-field transport events in a simple magnetized toroidal plasma. *Physics of Plasmas*, 15(4):042303, April 2008.

[49] K. E. Thome, M. W. Bongard, J. L. Barr, G. M. Bodner, M. G. Burke, R. J. Fonck, D. M. Kriete, J. M. Perry, and D. J. Schlossberg. High Confinement Mode and Edge Localized Mode Characteristics in a Near-Unity Aspect Ratio Tokamak. *Physical Review Letters*, 116(17):175001, April 2016.

[50] B. Nold, T. T. Ribeiro, M. Ramisch, Z. Huang, H. W. Müller, B. D. Scott, and U. Stroth and. Influence of temperature fluctuations on plasma turbulence investigations with Langmuir probes. *New Journal of Physics*, 14(6):063022, June 2012.

[51] Takuma Yamada, Sanae-I. Itoh, Kenichiro Terasaka, Naohiro Kasuya, Yoshihiko Nagashima, Shunjiro Shinohara, Takashi Maruta, Masatoshi Yagi, Shigeru Inagaki, Yoshinobu Kawai, Akihide Fujisawa, and Kimitaka Itoh. Spatiotemporal Behavior of Drift Waves in LMD-U. *Plasma and Fusion Research*, 3:S1021–S1021, 2008.

[52] W. Horton, Jean C. Perez, Troy Carter, and Roger Bengtson. Vorticity probes and the characterization of vortices in the Kelvin–Helmholtz instability in the large plasma device experiment. *Physics of Plasmas*, 12(2):022303, February 2005.

[53] F. Brochard, E. Gravier, and G. Bonhomme. Transition from flute modes to drift waves in a magnetized plasma column. *Physics of Plasmas*, 12(6):062104, June 2005.

[54] M. J. Burin, G. R. Tynan, G. Y. Antar, N. A. Crocker, and C. Holland. On the transition to drift turbulence in a magnetized plasma column. *Physics of Plasmas*, 12(5):052320, May 2005.

[55] G. R. Tynan, C. Holland, J. H. Yu, A. James, D. Nishijima, M. Shimada, and N. Taheri. Observation of turbulent-driven shear flow in a cylindrical laboratory plasma device. *Plasma Physics and Controlled Fusion*, 48(4):S51–S73, March 2006.

[56] T. Kobayashi, S. Inagaki, Y. Kosuga, M. Sasaki, Y. Nagashima, T. Yamada, H. Arakawa, N. Kasuya, A. Fujisawa, S.-I. Itoh, and K. Itoh. Structure formation in parallel ion flow and density profiles by cross-ferroic turbulent transport in linear magnetized plasma. *Physics of Plasmas*, 23(10):102311, October 2016.

[57] Yoshihiko Nagashima, Shigeru Inagaki, Kunihiro Kamakaki, Hiroyuki Arakawa, Takuma Yamada, Shunjiro Shinohara, Yoshinobu Kawai, Masatoshi Yagi, Akihide Fujisawa, Sanae I. Itoh, Kimitaka Itoh, and Yuichi Takase. Development of radially movable multichannel Reynolds stress probe system for a cylindrical laboratory plasma. *Review of Scientific Instruments*, 82(3), March 2011.

[58] G. R. Tynan, A. D. Bailey, G. A. Campbell, R. Charatan, A. de Chambrier, G. Gibson, D. J. Hemker, K. Jones, A. Kuthi, C. Lee, T. Shoji, and M. Wilcoxson. Characterization of an azimuthally symmetric helicon wave high density plasma source. *Journal of Vacuum Science & Technology A*, 15(6):2885–2892, November 1997.

[59] Franklin Díaz. The Vasimr Rocket. *Scientific American - SCI AMER*, 283:90–97, November 2000.

[60] Kazunori Takahashi and Akira Ando. Laboratory Observation of a Plasma-Flow-State Transition from Diverging to Stretching a Magnetic Nozzle. *Physical Review Letters*, 118(22):225002, June 2017.

[61] Kazunori Takahashi, Yoshinori Takao, and Akira Ando. Thrust imparted by a stepped-diameter magnetic nozzle rf plasma thruster. *Applied Physics Letters*, 113(3):034101, July 2018.

[62] A. W. Trivelpiece and R. W. Gould. Space Charge Waves in Cylindrical Plasma Columns. *Journal of Applied Physics*, 30(11):1784–1793, November 1959.

[63] Konstantin P. Shamrai. Stable modes and abrupt density jumps in a helicon plasma source. *Plasma Sources Science and Technology*, 7(4):499–511, November 1998.

[64] Shogo Isayama, Shunjiro Shinohara, and Tohru Hada. Review of Helicon High-Density Plasma: Production Mechanism and Plasma/Wave Characteristics. *Plasma and Fusion Research*, 13:1101014–1101014, 2018.

[65] Hirotyuki Arakawa, Shigeru Inagaki, Yusuke Kosuga, Makoto Sasaki, Fumiyoshi Kin, Kazunobu Hasamada, Kotaro Yamasaki, Tatsuya Kobayashi, Takuma Yamada, Yoshihiko Nagashima, Akihide Fujisawa, Naohiro Kasuya, Kimitaka Itoh, and Sanae-I. Itoh. Ion temperature measurement by laser-induced fluorescence spectroscopy in panta. *IEEJ Transactions on Electrical and Electronic Engineering*, 14(10):1450–1454, 2019.

[66] S. Tokuda, Y. Kawachi, M. Sasaki, H. Arakawa, K. Yamasaki, K. Terasaka, and S. Inagaki. Bayesian inference of ion velocity distribution function from laser-induced fluorescence spectra. *Scientific Reports*, 11(1):20810, October 2021.

[67] J. E. Allen, R. L. F. Boyd, and P. Reynolds. The Collection of Positive Ions by a Probe Immersed in a Plasma. *Proceedings of the Physical Society. B*, 70(3):297–304, March 1957.

[68] Francis F. Chen. Langmuir probe analysis for high density plasmas. *Physics of Plasmas*, 8(6):3029–3041, June 2001.

[69] K. Riemann. The Bohm criterion and sheath formation. *Journal of Physics D: Applied Physics*, 1991.

[70] E. O. Johnson and L. Malter. A Floating Double Probe Method for Measurements in Gas Discharges. *Physical Review*, 80(1):58–68, October 1950.

[71] A. Qayyum, N. Ahmad, S. Ahmad, Farah Deeba, Rafaqat Ali, and S. Hussain. Time-resolved measurement of plasma parameters by means of

triple probe. *Review of Scientific Instruments*, 84(12):123502, December 2013.

[72] J. P. Sheehan and N. Hershkowitz. Emissive probes. *Plasma Sources Science and Technology*, 20(6):063001, November 2011.

[73] T. Klinger and A. Piel. Investigations of attractors arising from the interaction of drift waves and potential relaxation instabilities. *Physics of Fluids B: Plasma Physics*, 4(12):3990–3995, December 1992.

[74] Christiane Schröder, Thomas Klinger, Dietmar Block, Alexander Piel, Gérard Bonhomme, and Volker Naulin. Mode Selective Control of Drift Wave Turbulence. *Physical Review Letters*, 86(25):5711–5714, June 2001.

[75] U. Stroth, F. Greiner, C. Lechte, N. Mahdizadeh, K. Rahbarnia, and M. Ramisch. Study of edge turbulence in dimensionally similar laboratory plasmas. *Physics of Plasmas*, 11(5):2558–2564, May 2004.

[76] T. Yamada, Y. Nagashima, S. Inagaki, Y. Kawai, M. Yagi, S.-I. Itoh, T. Maruta, S. Shinohara, K. Terasaka, M. Kawaguchi, M. Fukao, A. Fujisawa, and K. Itoh. Fine positioning of a poloidal probe array. *Review of Scientific Instruments*, 78(12):123501, December 2007.

[77] P. Welch. The use of fast Fourier transform for the estimation of power spectra: A method based on time averaging over short, modified periodograms. *IEEE Transactions on Audio and Electroacoustics*, 15(2):70–73, June 1967.

[78] R. B. Blackman and J. W. Tukey. The measurement of power spectra from the point of view of communications engineering — Part I. *The Bell System Technical Journal*, 37(1):185–282, January 1958.

[79] Tad J. Ulrych and Thomas N. Bishop. Maximum entropy spectral analysis and autoregressive decomposition. *Reviews of Geophysics*, 13(1):183–200, 1975.

[80] N. R. Lomb. Least-squares frequency analysis of unequally spaced data. *Astrophysics and Space Science*, 39(2):447–462, February 1976.

[81] J. D. Scargle. Studies in astronomical time series analysis. II. Statistical aspects of spectral analysis of unevenly spaced data. *The Astrophysical Journal*, 263:835–853, December 1982.

[82] M. Zechmeister and M. Kürster. The generalised Lomb-Scargle periodogram - A new formalism for the floating-mean and Keplerian periodograms. *Astronomy & Astrophysics*, 496(2):577–584, March 2009.

[83] Jacob T. VanderPlas. Understanding the Lomb–Scargle Periodogram. *Astrophysical Journal Supplement*, 236(1):16, May 2018.

[84] H. Gupta and R. Mehra. Power Spectrum Estimation using Welch Method for various Window Techniques. *Computer Science*, 2013.

[85] K. M. M. Prabhu. *Window Functions and Their Applications in Signal Processing*. Taylor & Francis, 2014.

[86] Ch. P. Ritz, E. J. Powers, R. W. Miksad, and R. S. Solis. Nonlinear spectral dynamics of a transitioning flow. *The Physics of Fluids*, 31(12):3577–3588, December 1988.

[87] P. H. Diamond, M. N. Rosenbluth, E. Sanchez, C. Hidalgo, B. Van Milligen, T. Estrada, B. Brañas, M. Hirsch, H. J. Hartfuss, and B. A. Carreras. In Search of the Elusive Zonal Flow Using Cross-Bicoherence Analysis. *Physical Review Letters*, 84(21):4842–4845, May 2000.

[88] Sanae-I. Itoh, Kimitaka Itoh, Yoshihiko Nagashima, and Yusuke Kosuga. On the Application of Cross Bispectrum and Cross Bicoherence. *Plasma and Fusion Research*, 12:1101003–1101003, 2017.

[89] Norden E. Huang, Zheng Shen, Steven R. Long, Manli C. Wu, Hsing H. Shih, Quanan Zheng, Nai-Chyuan Yen, Chi Chao Tung, and Henry H. Liu. The empirical mode decomposition and the Hilbert spectrum for nonlinear and non-stationary time series analysis. *Proceedings of the Royal Society of London. Series A: Mathematical, Physical and Engineering Sciences*, 454(1971):903–995, March 1998.

[90] Dragan B. Ilić. Measurement of Ion-Acoustic Plasma Turbulence by Cross-Power Spectra. *Physical Review Letters*, 34(8):464–466, February 1975.

[91] J. M. Beall, Y. C. Kim, and E. J. Powers. Estimation of wavenumber and frequency spectra using fixed probe pairs. *Journal of Applied Physics*, 53(6):3933–3940, June 1982.

[92] E. Wigner. On the Quantum Correction For Thermodynamic Equilibrium. *Physical Review*, 40(5):749–759, June 1932.

[93] H. Inuzuka, T. Ishiguro, and S. Mizuno. Elimination of cross-components in the Wigner distribution of the exponentially swept data by varying the sampling rate. In *Conference Proceedings. 10th Anniversary. IMTC/94. Advanced Technologies in I M. 1994 IEEE Instrumentation and Measurement Technolgy Conference (Cat. No.94CH3424-9)*, pages 717–720 vol.2, May 1994.

[94] K. Narahari Rao, R. Narasimha, and M. A. Badri Narayanan. The 'bursting' phenomenon in a turbulent boundary layer. *Journal of Fluid Mechanics*, 48(2):339–352, July 1971.

[95] R. F. Blackwelder and R. E. Kaplan. On the wall structure of the turbulent boundary layer. *Journal of Fluid Mechanics*, 76(1):89–112, July 1976.

[96] Garry L. Brown and Andrew S. W. Thomas. Large structure in a turbulent boundary layer. *The Physics of Fluids*, 20(10):S243–S252, October 1977.

[97] J. H. Shin, B. H. Choi, Y. G. Lim, D. U. Jeong, and K. S. Park. Automatic ballistocardiogram (BCG) beat detection using a template matching approach. In *2008 30th Annual International Conference of the IEEE Engineering in Medicine and Biology Society*, pages 1144–1146, August 2008.

[98] Angela O. Leung, Ian Paterson, and Richard B. Thompson. Free-breathing cine MRI. *Magnetic Resonance in Medicine*, 60(3):709–717, 2008.

[99] Shigeru Inagaki, Yudai Miwa, Tatsuya Kobayashi, Takuma Yamada, Yoshihiko Nagashima, Tomohiro Mitsuzono, Hiromitsu Fujino,

Makoto Sasaki, Naohiro Kasuya, Maxime Lesur, Yusuke Kosuga, Akihide Fujisawa, Sanae I. Itoh, and Kimitaka Itoh. Identification of quasi-periodic nonlinear waveforms in turbulent plasmas. *Plasma and Fusion Research*, 9:1201016, 2014.

[100] Fumiyoshi Kin, Kimitaka Itoh, Tim Happel, Gregor Birkenmeier, Akihide Fujisawa, Sigeru Inagaki, Sanae-I. Itoh, Ulrich Stroth, and ASDEX Upgrade Team. Comparison of Conditional Average Using Threshold and Template Methods for Quasi-Periodic Phenomena in Plasmas. *Plasma and Fusion Research*, 14(0):1402114–1402114, June 2019.

[101] Yuichi Kawachi, Sigeru Inagaki, Kentaro Tomita, Kotaro Yamasaki, Fumiyoshi Kin, Yusuke Kosuga, Makoto Sasaki, Yoshihiko Nagashima, Naohiro Kasuya, Kazunobu Hasamada, Boyu Zhang, and Akihide Fujisawa. Determination of Spatiotemporal Structure of Fluctuations by Statistical Averaging Method. *Plasma and Fusion Research*, 13:3401105–3401105, 2018.

[102] Feng-Jen Chang and Eiichirou Kawamori. Control of solitary-drift-wave formation by radial density gradient in laboratory magnetized cylindrical plasma. *Physics of Plasmas*, 26(7):072304, July 2019.

[103] F. Kin, K. Itoh, A. Fujisawa, Y. Kosuga, M. Sasaki, T. Yamada, S. Inagaki, S.-I. Itoh, T. Kobayashi, Y. Nagashima, N. Kasuya, H. Arakawa, K. Yamasaki, and K. Hasamada. Extraction of nonlinear waveform in turbulent plasma. *Physics of Plasmas*, 25(6):062304, June 2018.

[104] A. I. Smolyakov, P. H. Diamond, and M. Malkov. Coherent Structure Phenomena in Drift Wave–Zonal Flow Turbulence. *Physical Review Letters*, 84(3):491–494, January 2000.

[105] G. Chiodini, C. Riccardi, and M. Fontanesi. A 400 kHz, fast-sweep Langmuir probe for measuring plasma fluctuations. *Review of Scientific Instruments*, 70(6):2681–2688, June 1999.

[106] Mark A. Meier, Roger D. Bengtson, Gary A. Hallock, and Alan J. Wootton. Adiabatic Electron Thermal Pressure Fluctuations in Tokamak Plasmas. *Physical Review Letters*, 87(8):085003, August 2001.

[107] V. Skoutnev, P. Dourbal, E. Rodríguez, and Y. Raitses. Fast sweeping probe system for characterization of spokes in E × B discharges. *Review of Scientific Instruments*, 89(12):123501, December 2018.

[108] B. N. Rogers and Paolo Ricci. Low-frequency turbulence in a linear magnetized plasma. *Physical Review Letters*, 104(22):225002, 2010.

[109] P. Popovich, M. V. Umansky, T. A. Carter, and B. Friedman. Analysis of plasma instabilities and verification of the BOUT code for the Large Plasma Device. *Physics of Plasmas*, 17(10):102107, 2010.

[110] R. Kaur, A. K. Singh, R. Singh, A. Sarada Sree, and S. K. Mattoo. Territorial characteristics of low frequency electrostatic fluctuations in a simple magnetized torus. *Physics of Plasmas*, 18(1):012109, January 2011.

[111] D. Biskamp and A. Zeiler. Nonlinear Instability Mechanism in 3D Collisional Drift-Wave Turbulence. *Physical Review Letters*, 74(5):706–709, January 1995.

[112] J. Weiland, Heiji Sanuki, and C. S. Liu. Convective cell formation and anomalous diffusion due to electromagnetic drift wave turbulence. *The Physics of Fluids*, 24(1):93–101, January 1981.

[113] J. S. Kim, R. D. Durst, R. J. Fonck, E. Fernandez, A. Ware, and P. W. Terry. Technique for the experimental estimation of nonlinear energy transfer in fully developed turbulence. *Physics of Plasmas*, 3(11):3998–4009, 1996.

[114] T. Dudok de Wit, V. V. Krasnosel'skikh, M. Dunlop, and H. Lühr. Identifying nonlinear wave interactions in plasmas using two-point measurements: A case study of Short Large Amplitude Magnetic Structures (SLAMS). *Journal of Geophysical Research: Space Physics*, 104(A8):17079–17090, 1999.

[115] P. Manz, M. Xu, S. C. Thakur, and G. R. Tynan. Nonlinear energy transfer during the transition to drift-interchange turbulence. *Plasma Physics and Controlled Fusion*, 53(9), 2011.

[116] Song Chai, Yuhong Xu, Zhe Gao, Wenhao Wang, Yangqing Liu, and Yi Tan. Experimental measurements of energy transfer and nonlinear interaction in turbulence at the sino-united spherical tokamak. *Physics of Plasmas*, 24(3):32503, 2017.

[117] F. M. Poli, M. Podestà, and A. Fasoli. Development of electrostatic turbulence from drift-interchange instabilities in a toroidal plasma. *Physics of Plasmas*, 14(5):052311, May 2007.

[118] Y. Lang, Z. B. Guo, X. G. Wang, and B. Li. Avalanches triggered by Kelvin-Helmholtz instability in a cylindrical plasma device. *Physical Review E,* 100(3):1–10, 2019.

[119] M. Sasaki, T. Kobayashi, R. O. Dendy, Y. Kawachi, H. Arakawa, and S. Inagaki. Evaluation of abrupt energy transfer among turbulent plasma structures using singular value decomposition. *Plasma Physics and Controlled Fusion*, 63(2):025004, December 2020.

[120] Makoto Sasaki, Naohiro Kasuya, Shinichiro Toda, Takuma Yamada, Yusuke Kosuga, Hiroyuki Arakawa, Tatsuya Kobayashi, Shigeru Inagaki, Akihide Fujisawa, Yoshihiko Nagashima, Kimitaka Itoh, and Sanae-I. Itoh. Multiple-Instabilities in Magnetized Plasmas with Density Gradient and Velocity Shears. *Plasma and Fusion Research*, 12:1401042–1401042, 2017.

[121] K. J. Zhao, Y. Nagashima, P. H. Diamond, J. Q. Dong, K. Itoh, S.-I. Itoh, L. W. Yan, J. Cheng, A. Fujisawa, S. Inagaki, Y. Kosuga, M. Sasaki, Z. X. Wang, L. Wei, Z. H. Huang, D. L. Yu, W. Y. Hong, Q. Li, X. Q. Ji, X. M. Song, Y. Huang, Yi. Liu, Q. W. Yang, X. T. Ding, and X. R. Duan. Synchronization of Geodesic Acoustic Modes and Magnetic Fluctuations in Toroidal Plasmas. *Physical Review Letters*, 117(14):145002, September 2016.

[122] J Adamek, J Horacek, J Seidl, HW Müller, R Schrittwieser, F Mehlmann, P Vondracek, S Ptak, COMPASS Team, ASDEX Upgrade Team, et al. Direct plasma potential measurements by ball-pen probe and self-emitting langmuir probe on COMPASS and ASDEX upgrade. *Contributions to Plasma Physics*, 54(3):279–284, 2014.